Electronic and optical properties of semiconductor nanowires with prismatic geometry

by

Miguel Urbaneja Torres

Dissertation submitted to the Department of Applied Engineering
at Reykjavík University in partial fulfillment
of the requirements for the degree of
Doctor of Philosophy

February 2020

Thesis Committee:

Andrei Manolescu, Supervisor
Professor, Reykjavík University, Iceland

Viðar Guðmundsson, Committee Member
Professor, University of Iceland, Iceland

Sigurður I. Erlingsson, Committee Member
Professor, Reykjavík University, Iceland

Guido Goldoni, Examiner
Associate Professor, University of Modena and Reggio Emilia, Italy

The undersigned hereby certify that they recommend to the Department of Applied Engineering at Reykjavík University for acceptance this Dissertation entitled **Electronic and optical properties of semiconductor nanowires with prismatic geometry** submitted by **Miguel Urbaneja Torres** in partial fulfillment of the requirements for the degree of **Doctor of Philosophy (Ph.D.) in Applied Physics**

25 February 2020
date

A Manolescu
Andrei Manolescu, Supervisor
Professor, Reykjavík University, Iceland

Viðar Guðmundsson, Committee Member
Professor, University of Iceland, Iceland

Sigurður I. Erlingsson, Committee Member
Professor, Reykjavík University, , Iceland

Guido Goldoni, Examiner
Associate Professor, University of Modena and Reggio Emilia, Italy

The undersigned hereby grants permission to the Reykjavík University Library to reproduce single copies of this Dissertation entitled **Electronic and optical properties of semiconductor nanowires with prismatic geometry** and to lend or sell such copies for private, scholarly or scientific research purposes only.
The author reserves all other publication and other rights in association with the copyright in the Dissertation, and except as herein before provided, neither the Dissertation nor any substantial portion thereof may be printed or otherwise reproduced in any material form whatsoever without the author's prior written permission.

25/02/2020
.....
date

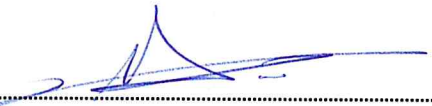

.....
Miguel Urbaneja Torres
Doctor of Philosophy

Electronic and optical properties of semiconductor nanowires with prismatic geometry

Miguel Urbaneja Torres

February 2020

Abstract

In this work, fundamental electronic and optical properties of semiconductor prismatic nanowires, which are a direct consequence of their geometry, are numerically studied. The quantum states of electrons confined in polygonal shells, which describe the cross-section of nanowires where a conducting shell surrounds an insulating core, are obtained using a finite-elements method based on a polar grid, which allows to model a wide range of different shapes. Directly related with the quantum states of the nanowires, the charge and current distributions, conductance and excitonic states are obtained using several computational models. The light scattering by prismatic nanowires is also studied by solving Maxwell's equations with the finite-elements method built in the software COMSOL Multiphysics. The results presented here demonstrate that the specific geometry of such nanowires is a source of rich and interesting phenomenology.

Titll verkefnis

Miguel Urbaneja Torres

febrúar 2020

Útdráttur

Í þessu verki eru raf- og ljósfræðilegir eiginleikar hálfleiðandi nanóvíra út frá rúmfræði þeirra, rannsakaðir með tölulegum reikningum. Skammtafræðileg ástönd rafeinda í strendingslaga hvelum, sem lýsa þverskurði nanóvírana með leiðandi skel umhverfis einangrandi kjarna, eru reiknuð með bútaaðferð á neti í pólhnitum. Hleðslu- og straumþéttleiki ásamt leiðni og örveinda ástöndum, sem eru beintengd skammtaástöndum nanóvíra, eru fengin með fleiri en einu tölvulíkani. Ljósdreifing strendingslaga nanóvíra er að auki skoðuð með lausnum Maxwells jafna með bútaaðferð hugbúnaðisins COMSOL Multiphysics. Niðurstöður sýna að rúmfræðilega lögun nanóvíra er rík uppspretta áhugaverðar eðlisfræði.

Le phénomène passe. Je cherche les lois.
- Lautréamont

Acknowledgements

I would like to express my sincere and deep gratitude to my supervisor Andrei Manolescu for the continuous support and patience. I am also greatly thankful to my colleague Ania Sitek for her insightful comments and encouragement.

I would also like to express special gratitude to my family and friends. This dissertation would not have been possible without their warm love, continued patience, and endless support, even from the distance.

This work was financed by the Icelandic Research Fund, project 163438-051.

Publications

This PhD thesis is based on the following publications:

Journal articles

1. Anna Sitek, Miguel Urbaneja Torres, Kristinn Torfason, Vidar Gudmundsson, Andrea Bertoni and Andrei Manolescu. *Excitons in Core–Shell Nanowires with Polygonal Cross Sections.* Nano Letters **18**, 2581–2589 (2018).

2. Miguel Urbaneja Torres, Anna Sitek, Sigurdur I. Erlingsson, Gunnar Thorgilsson, Vidar Gudmundsson and Andrei Manolescu. *Conductance features of core-shell nanowires determined by their internal geometry.* Phys. Rev. B **98**, 085419 (2018).

3. Miguel Urbaneja Torres, Anna Sitek and Andrei Manolescu. *Anisotropic light scattering by prismatic semiconductor nanowires.* Optics Express **27**, 25502-25514 (2019).

4. Anna Sitek, Miguel Urbaneja Torres and Andrei Manolescu. *Corner and side localization of electrons in irregular hexagonal semiconductor shells.* Nanotechnology **30**, 454001 (2019).

5. Miguel Urbaneja Torres, Kristján Óttar Klausen, Anna Sitek, Sigurdur I. Erlingsson, Vidar Gudmundsson and Andrei Manolescu. *Anisotropic electromagnetic field emitted by core-shell semiconductor nanowires driven by an alternating current* Submitted (2019), arXiv:1912.10284.

Conference proceedings

1. Anna Sitek, Miguel Urbaneja Torres, Kristinn Torfason, Vidar Gudmundsson, and Andrei Manolescu. *Controlled Coulomb effects in core-shell quantum rings.* IEEE Conference Proceedings 19th International Conference on Transparent Optical Networks (ICTON) (2017).

2. Miguel Urbaneja Torres, Anna Sitek, Vidar Gudmundsson, Andrei Manolescu. *Radiated fields by polygonal core-shell nanowires.* IEEE Conference Proceedings 20th International Conference on Transparent Optical Networks (ICTON) (2018).

3. Miguel Urbaneja Torres, Anna Sitek and Andrei Manolescu. *Transverse polarization light scattering in tubular semiconductor nanowires.* IEEE Conference Proceedings 21th International Conference on Transparent Optical Networks (ICTON) (2019).

Posters and oral presentations

1. Miguel Urbaneja Torres[1], Anna Sitek, Vidar Gudmundsson and Andrei Manolescu. *Effects of coulomb interaction in polygonal core-shell nanowires.* NANOWIRE Week, Lund (2017) - Poster presentation.

2. Miguel Urbaneja Torres, Anna Sitek, Vidar Gudmundsson, Andrei Manolescu. *Conductance steps in polygonal core-shell nanowires.* NORDITA Winter School in Condensed matter physics (2018) - Poster presentation.

3. Miguel Urbaneja Torres, Anna Sitek and Andrei Manolescu. *Conductance features of core-shell nanowires determined by their internal geometry.* NANOWIRE Week, Hamilton (2018) - Poster presentation.

4. Miguel Urbaneja Torres, Anna Sitek, Vidar Gudmundsson and Andrei Manolescu. *Radiated filed by polygonal core-shell nanowires.* 20th International Conference on Transparent Optical Networks (ICTON) (2018) - Invited talk.

5. Miguel Urbaneja Torres, Anna Sitek, and Andrei Manolescu. *Light scattering by subwavelength silicon nanowires.* COMSOL Conference, Lausanne (2018) - Poster presentation.

6. Miguel Urbaneja Torres, Anna Sitek and Andrei Manolescu. *Transverse polarization light scattering in tubular semiconductor nanowires.* 21th International Conference on Transparent Optical Networks (ICTON) (2019) - Invited talk.

[1]Underlined name in all these references is the presenter.

Contents

Chapter 1

Introduction

1.1 Background

1.1.1 Core-shell nanowires

The fabrication and study of nanostructures have been a focus of intense research over the last few decades due to their unparalleled properties, meant to shape the technology of the future [1]. As a result of the chase for means to control the properties of such structures, the development and refinement of growth techniques have lead to a rapid progress in the art of nanostructure synthesis, allowing for a high degree of design freedom with high accuracy, both in terms of composition and shape [2]. An example of such nanostructures are nanowires, structures with a length ranging from the order of hundreds of nanometers to a few microns and a diameter usually between a few tens and a few hundreds of nanometers [3].

Semiconductor nanowires are fundamental components of nanoelectronic devices with huge potential and versatility [4–7]. In particular III-V semiconductor materials [8, 9], e.g. InAs [10] or InN [11, 12], have recently drawn a high interest for nanowires growth, since the Fermi level pinning at the surface and the resulting electron accumulation layer lead to a high-electron conductance even at small radii [13].

Recently, semiconductor nanowires comprising heterostructures have been realized [14, 15]. Here, two kinds of heterostructures, axial and longitudinal (and combinations of both), are possible. In longitudinal heterostructures, two or more layers of different materials along the length of the structure compose the nanowires. In axial heterostructures, the composition is varied along the nanowires axis instead. This last type, so-called core/shell nanowires (CSNs), are radial heterojunctions of, at least, two different materials and have attracted huge attention in recent years as a result of their promising properties [16, 17]. As the name indicates, a central component (core) is surrounded by an outer layer (shell). In most cases, there is a mismatch between the lattice constant of the materials used which leads to substantial differences of energy bands with respect to the bulk of each material [18, 19]. Subsequently, the geometric details of the structure play an important role in the properties of the nanowire and, in particular, enable the possibility of achieving type II band alignment at the heterojunction through variations of the thickness of the layers [20, 21].

Due to the preferred growth orientation, following the crystallographic structure, of the more common materials used, the cross section of a CSN is usually hexagonal [22–24], although other shapes, like circular [11], square [25, 26], triangular [27–30] or even dodecagonal [31] are also possible (examples in Fig. 1.1). The field is recent

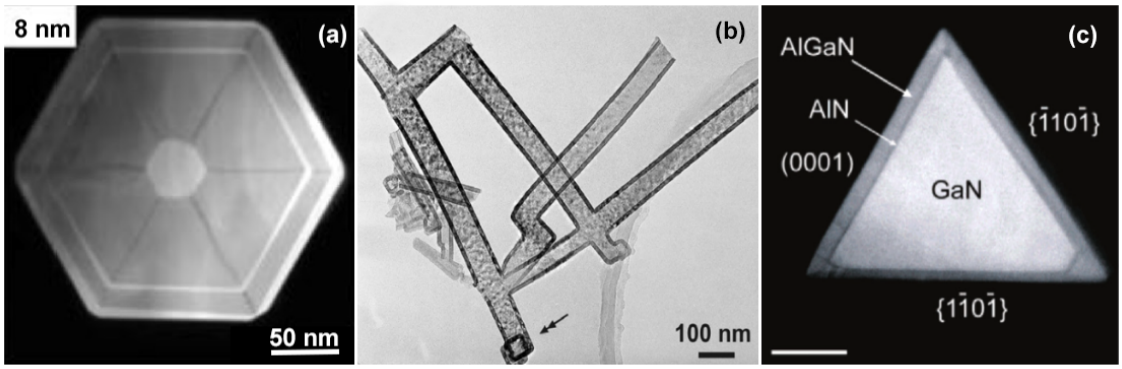

Figure 1.1: Core-shell nanowires with (a) hexagonal [38], (b) square [25] and (c) triangular [30] cross sections.

and evolves very fast, with new original and interesting geometries, exhibiting unique phenomenology, reported every year, e.g., a triangular shell surrounding a hexagonal core [32–34] or the other way around [35]. Another interesting possibility is etching the core, which leaves a hollow tubular nanowire behind [36, 37].

Unlike their cylindrical counterparts, where the electrons are uniformly distributed along the circumference, in prismatic nanowires the electron localization mechanism is more complex. As it has been known for a long time, thin bent wires, such as the polygonal contour, may localize states [39]. Hence, interesting effects may occur due to the possible localization of the carriers (electrons or holes) at the corners or on the sides of a CSN. Because of the narrow diameter and thickness, quantum interference effects are still present. Properly adjusting the thickness and the composition, the shell may become a tubular conductor, with each sharp edge of the polygonal cross-section acting as a quasi-one-dimensional (1D) channel [38, 40–44]. The band gaps of the core or of the shell may be different from the known values in the bulk materials, g-factors and spin-orbit coupling as well [45]. In practice these important parameters are sample dependent. The prismatic geometry is a source of unique physics and very rich quantum phenomena associated to it have been experimentally observed in CSNs, e.g., Aharonov-Bohm type magnetoconductance oscillations in GaAs/InAs CSNs [46, 47]. Many theoretical investigations have also been recently carried out. For instance, CSNs have been predicted to be able to host several interacting Majorana states [48, 49]. Additionally, other recent studies have predicted that, under a transversal magnetic field, tubular nanowires may exhibit a sign reversal of the thermal electric current caused by a thermal gradient along the nanowire [50–52]

Thus, nanowires, and especially CSNs, are not simply quasi-1D systems, but may have a complex internal structure which can be a very rich resource of unique physical properties.

1.1.2 Quantum transport

Due to their quantum nature, charge and spin transport properties in nanowires have attracted a great attention in recent years. The advance in fabrication and measuring methods has led to the possibility of probing some of the fundamental properties of these structures. Charge transport in nanowires usually takes place in subbands, as confined electrons can only occupy a set of discretized energy levels.

This phenomenon manifests itself in transport measurements by the quantization of the conductance, where each subband contributes with conductance of $G_0 = e^2/h$ [53].

The quantization of the conductance has recently been experimentally observed in InSb nanowires [54, 55]. Also, in recent DC magnetotransport experiments carried out by in the group of Thomas Schäpers in Jülich, where the nanowires are exposed to an axial magnetic field, i.e., parallel to its length, complex oscillations of the conductivity along the nanowire were observed [22, 56] with a h/e flux periodic component related to the Aharonov-Bohm effect, but also additional beating patterns and broad variations of mean values. Motivated by these results, recent theoretical work was carried out considering nanowires consisting on a cylindrical surface [57] where the h/e oscillations plus a superimposed modulation comparable to the experimental data due to spin effects were obtained.

On the other hand, electrons situated on a cylindrical surface in the presence of a magnetic field perpendicular to the axis of the cylinder, tend to localize on the lateral sides of the surface, where so-called snaking states are created. These are states captured along the lines where the radial component of the magnetic field vanishes and flips orientation such that the Lorentz force always bends the electron trajectory towards these lines [58, 59]. In a strong magnetic field, the snaking states become the states with the lowest energy and the conduction along the CSN is expected to occur on two separated lateral stripes formed by the snaking states and produce specific peaks of the DC conductance that can be split by an electric field transverse to the CSN [60].

Additionally, very recent experimental work has also been carried out demonstrating interesting phenomenology related to the charge transport in prismatic CSNs, like Coulomb blockade effect formed over the full length of InP/InAs nanowires with hexagonal cross section and triangular core [34] or magnetoconductance measurements in hexagonal GaAs/InSb nanowires [61].

1.1.3 Nanoantennas

The advances in the synthesis of nanostructures and in the knowledge of their properties have driven a rapid progress in the development of applications in the last two decades. Thanks to these advances, a revolution in the field of optics has been taking place. While the technology for the control of propagating electromagnetic radiation by means of subwavelength antennas is widespread for radio and microwaves, the control of light has historically been inaccessible due to the small (nanoscale) dimensions required for the equivalent antennas. Within this context, the dimensions and the flexible control of various properties of nanowires make them perfect candidates for a wide range of optical applications [62–64]. On the other hand, such reduction of the device size makes amplitude and phase measurements challenging and opens many questions concerning quantum effects occurring in the nanoscale systems. Even if of a very low power, a nanoantenna can transfer electromagnetic signals over short distances between optoelectronic elements, without contacts, possibly by near-field enhancement, at plasmonic frequencies [65]. Recent studies show that nanowires (which are not necessarily CSNs) can work not only as antennas for the detection of THz [66] and near-infrared radiation with polarization and wavelength selectivity functions [67], but also as emitter antennas of polarized light [68] or of single photons [69, 70]. Nanoantennas show huge possibilities for the design and application of quantum nanodevices since they may act as building blocks which enable light absorption and emission manipulation.

Present manufacturing technologies allow to grow core-multishell radial p-i-n junctions in which the scattering cross section exceeds the physical one. This enables occurrence of an optical antenna effect [71] that may be substantially enhanced when the system is covered by a dielectric shell [72]. The antenna effect in quantum wires depends on the structure geometry and allows to model absorption and corresponding photocurrents through adjusting the wire diameter. Interestingly, CSNs have been demonstrated to be able to increase absorption in solar cells while reducing the amount of active material used [73–76]. A great amount of experimental work has been carried out, reporting additional promising results. Just to mention a few more, nanoantennas may be used to control light-matter coupling and create radiation sources [77], nanoantennas made of Au, implemented on CSNs, may allow to control exciton generation [78] and nanorod systems may facilitate sub- and super-radiant emission [79].

1.1.4 Optical resonances in nanostructures

In the quest for the control of light in nanoscale dimensions, the study of light-matter interaction in dielectric nanostructures with high refractive index has become one of the most attractive research topics in photonics [80, 81]. This interest is driven by the phenomenology associated with the scattering of light in the optical range, i.e., of wavelength comparable to the size of the scatterers, with negligible losses, contrarily to their plasmonic metallic counterparts of similar size [82–84]. The materials used, usually Si and other semiconductors like InAs, GaAs and GaP, and the geometry of the nanoparticles allow for tunability of electric or magnetic resonances, which often coexist, making them interesting components of optical devices, allowing to manipulate visible light at nanoscale [68, 74, 85–88].

The classic textbook example of light scattering on spherical nanoparticles can be analyzed with the Mie theory [89, 90]. Still, the experimental evidence of specific resonances is an ongoing research subject [91–93]. A wide range of non-spherical nanostructures have been considered for light scattering, such as nanowires [94–96], nanoblocks or nanopyramids [97–99], or metasurfaces [100–103]. This variety of structures exhibits rich phenomenology, including directional scattering through the interference of different resonant modes [104–108], tunable directionality [109, 110], optical cloaking [111], second and third-harmonic generation [112] or surface enhanced Raman scattering [84]. Additionally, Fano resonances, attracted considerable attention in recent research on photonic nanodevices or nanostructures, both dielectric and metallic, due to their promising applicability in optical switching and sensing [113]. They are generated by resonant modes occurring on the background of a continuous spectrum, and observed as narrow S-shaped features of the scattering cross section, being thus sensitive to various adjustable parameters. Such resonances are more pronounced in the dielectric structures, where the absorption is low [114–116]. Strong Fano resonances can be hosted by dielectric nanowires as a result of the superposition of sharp longitudinal modes and a broad Mie background or leaky mode [109, 117, 118].

1.2 Objectives and motivation

The main goal of the work presented in this thesis is to understand the impact of the tubular and polygonal geometry on several properties of CSNs. The thesis is divided in two distinct parts. The first part contains the studies directly related to the quantum

states of CSNs, and focuses on understanding the charge and current distributions along the nanowires and the properties of optically active excitonic states confined in the shell. The objective of the second part is to understand the consequences of this geometry in the light scattering properties of dielectric nanowires. In general, the specific geometry of CSNs has not been studied much experimentally. It is either seen as a natural outcome, when the nanowires are hexagonal, or as a curiosity, when they are of different types. To the best of our knowledge, experimental results with features related to the internal geometry of the nanowire are very rare. The motivation behind this work is to stimulate experimental groups to do such investigations and to achieve the corresponding quality of the samples with a clear manifestation of the role played by the geometry.

This thesis is a review of the most important results presented in the published papers where the candidate was the first or the second author, listed at page IX. Several fragments of the published text have been reused to explain the methodology and the results, in a logical order and unified manner. Unpublished calculations, together with other results currently considered for publication, are also included and integrated with the published parts.

1.2.1 Charge and current distributions

The main part of the thesis begins with the derivation of the spectra of quantum states of electrons confined in a CSN, i.e., the energies and wave functions. Prismatic tubes will be considered as models of core-shell nanowires with an insulating core and a conductive shell. A computational method based on a discrete polar grid and finite differences is used in order to model any arbitrary polygonal sample. The model is also applicable to uniform nanowires (i.e. not core-shell) which have conductive surface states due to the Fermi level pinning. However, nanowires built of topological materials are not addressed. In the calculations a Schrödinger Hamiltonian is used. In this model the cross section of the prismatic shell is a narrow polygonal ring (hexagonal, square, or triangular), i.e., with lateral thickness much smaller than the overall diameter of the nanowire.

In this geometry the electrons with the lowest energies are localized in the corners of the polygon and the electrons in the next layer of energy states are localized on the sides [119, 120]. The corner and side states are energetically separated by an interval that depends on the geometry and on the aspect ratio of the polygon, it increases with decreasing the shell thickness or the number of corners, and it can become comparable or larger than the energy corresponding to the room temperature [121–123]. Hence, such structures can contain a well-separated subspace of corner states, potentially robust to many types of perturbations. On the contrary, if the shell thickness is not sufficiently thin (with respect to the diameter of the wire), the localization patterns are more complex, the corner and side states are mixed up, and the polygonal structure has little effect on the electron density distribution [124].

It has been shown, using inelastic light scattering, the coexistence of one- and two-dimensional electron channels, along the edges and facets, respectively, of GaAs core-shell nanowires [125]. In transport experiments one can mention here the detection of flux periodic oscillations of the conductance in the presence of a magnetic field longitudinal to the nanowire [56], which indicates the radial localization of the electrons in the shell. Or, flux periodic oscillations with the magnetic field perpendicular to the nanowire, due to the formation of snaking states on the sides of the tubular conductor

[13, 126]. Still, results indicating the presence of corner or side localized states, or the energy gap between them, or other details implied by the prismatic geometry of the shell, have not been reported yet.

The intention of the work done in this part is to predict specific features of the conductance of core-shell nanowires determined by the prismatic geometry of the nanowire when the electronic transport occurs within the shell. Such features, which could be experimentally tested, can reveal to what extent the electronic states are influenced by the polygonal geometry, and if not, to what extent the quality of the nanowire needs to be improved in order to achieve a robust corner localization.

1.2.2 Excitonic states

In a recent theoretical work [121], the optical absorption spectra of low-energy electrons confined in polygonal rings was obtained by considering independent electrons and evaluating the implications of the polygonal geometry on the transitions between corner and/or side states. It has also been shown that, for electrons with mutual Coulomb repulsion and for appropriate material parameters, it is possible to obtain multielectron states within the gap separating corner and side states [122]. The work presented in this part is a natural continuation of these previous studies, and focuses on the study of excitonic states confined in the shell of prismatic CSNs.

Excitons are bound states consisting of pairs of electrons and holes attracted to each other via Coulomb interaction. The possibility of controlling the band alignment during the fabrication process allows for the confinement of such pairs in the shell of a CSN. In order to obtain the energy spectra and the exciton configuration in the shell of a quantum ring, a multielectron method [127] where both valence and conduction bands are included is used. The Coulomb interaction is included in a nonperturbative manner and only electronic states with zero wavevector k are considered. The model includes only electrons within a configuration-interaction scheme and the Coulomb interaction treated by numerical diagonalization.

The main objective in this part is to study the implication of the corner and side electron localization in the formation of optically active in-gap excitonic states.

1.2.3 Antenna characteristics

Once a reasonable description of the current distribution is obtained, the radiated electromagnetic field is calculated using the classical Biot-Savart method, i.e., by solving the Maxwell's equations to derive the propagating electric and magnetic field with the help of the vector potential in the Coulomb gauge.

By numerically obtaining the quantum states for selected geometries, the current along an infinite polygonal shell driven by a time-dependent harmonic voltage bias is calculated. The implications of the corner localized states are discussed, and in particular the anisotropy of the radiated field and features that can capture the localization itself. Furthermore, the manipulation of the radiated field is explored by applying an external magnetic field to break the spatial symmetry of the charge and current distributions.

The main objective is to qualitatively analyze the signature of the polygonal geometry in the structure of the radiated fields, related to the corner or side localization, and to the applied external fields. The anisotropy of the radiated field is limited to

the near field zone, but depending on the geometry of the nanowire and on other parameters, that zone can be considerably large compared to the nanowire radius.

1.2.4 Light scattering

In the last part of this thesis the scattering of light by dielectric CSN is studied. The Maxwell equations are solved using a finite differences method for hollow cylindrical nanowires, i.e., nanocylinders or nanotubes and for prismatic bulk-like nanowires. The Maxwell equations are solved for the scattered field using a finite elements method included in the wave optics module of COMSOL Multiphysics [128]. The scattering cross section is evaluated under transversal plane wave illumination, i.e., either transversal electric (TE) or magnetic (TM) field. The calculations are carried out for both short and long nanowires. Short nanowires offer a simpler scattering spectra which facilitates an insight into the role played by the geometry of the nanowires but long nanowires exhibit a much richer and complex phenomenology, such as high directivity [109] or sharp Fano resonances [118].

There are two main objectives in this part. The first one is to understand how the presence of a hole inside the wire disturbs the modes in a tubular nanowire. The resonant modes are the result of the field distribution inside the sample, the opening of an internal radius affects different modes in different ways, allowing for the possibility of tuning their spectral position. An exploration of this tunability through variations of the geometrical parameters (internal and external radii) for both tubular and bulk-like nanowires is carried out.

The second part focuses on nanowires with polygonal cross sections. The objective here is to explore the effects of the prismatic geometry on the light scattering when the direction of incidence is varied, between being perpendicular to the sides or edges of the prism. The geometrical cross section that the incident light faces changes when the angle of incidence is rotated, so a change in the scattering behaviour may follow. The possibility of tuning the directivity or the spectral position of resonant modes through an anisotropic scattering could have interesting applications in switching or sensing. Previous studies have demonstrated tunable directivity in rectangular nanowires by changing the polarization of the incident light and by changing the illumination direction gradually from transverse to longitudinal incidence [109], but the possibility of controlling light scattering by a transversal rotation of the geometry has only been recently considered in pyramidal silicon nanostructures [110].

Chapter 2

Computational methods

In this chapter the computational methods used in the thesis are introduced. For the study of the quantum and electrical properties of the nanowires a finite elements methods based on a polar grid was developed using Fortran. The study of optical scattering, instead, was carried out with the software COMSOL Multiphysics, also based on finite elements methods.

2.1 Quantum states

To begin with, a system of non-interacting electrons confined in a prismatic shell with a polygonal cross section is analyzed. The Hamiltonian of the problem is of Schrödinger type and can be decomposed as

$$H = H_t + H_l + H_s \ , \tag{2.1}$$

where the terms H_t, H_l, and H_s correspond to the transverse, longitudinal, and spin degrees of freedom, respectively.

The transverse Hamiltonian is

$$H_t = \frac{(-i\hbar\partial_x + eA_x)^2 + (-i\hbar\partial_y + eA_y)^2}{2m_{\text{eff}}} - e\mathbf{E}\cdot\boldsymbol{r} \ , \tag{2.2}$$

where m_{eff} is the effective electron mass in the shell material, $A = (A_x, A_y, A_z) = (-yB_z/2, xB_z/2, yB_x - x_B y)$ is the vector potential, e is the electron charge and $\mathbf{E} = (E_x, E_y, 0)$ is an external electric field perpendicular to the wire. The transverse Hamiltonian depends only on the longitudinal magnetic field B_z. Technically, the Hamiltonian 2.2 is restricted to a lattice of points that covers the cross section of the shell. The eigenstates and eigenvectors/eigenfunctions of the transverse Hamiltonian are obtained with a discretization method based on polar grid. To construct the model of a polygonal ring we first define a circular disk [129] on which we superimpose polygonal constraints and further reduce the grid to sites situated between the boundaries, Fig. 2.1. The number of points of the shell is taken to be $N_p = N_r N_\phi$, where $N_r = 60$ is the number of points in the radial direction and $N_p hi = N_c orners \cdot N_r$ is the number of points in the angular direction, always a multiple of the number of corners of the chosen polygon. The Hilbert space associated with the polar grid is spanned by vectors $|nj\rangle$, where the two integer numbers label/represent the discretized radial (r_n,) and angular (ϕ_j,) coordinates, respectively.

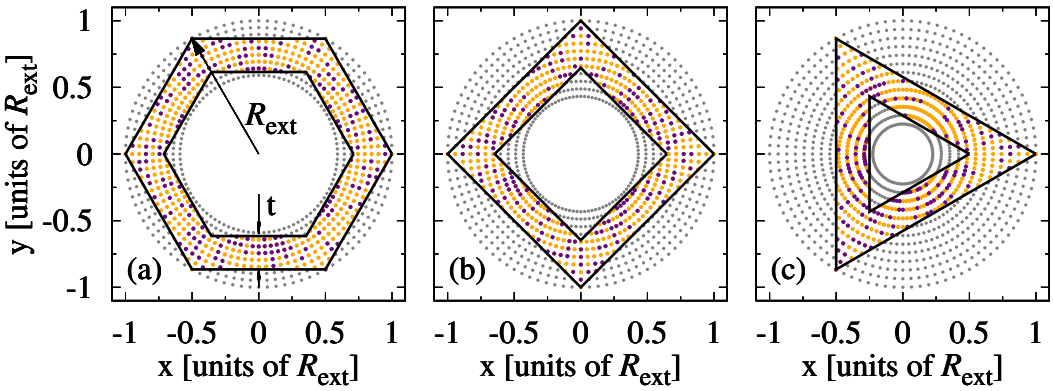

Figure 2.1: The cross sections of the prismatic shells are defined by applying boundaries on a circular ring discretized in polar coordinates. Only the lattice points inside the polygonal shell (shown in yellow) are used in the transverse Hamiltonian 2.2, where a chosen percentage of random-strength impurities (purple points) can be included. R_{ext} and t indicate the nanowire radius and shell thickness, respectively. For clarity the figures show only a subset of lattice points, whereas the numerical calculations are performed with 6000-10000 points, depending on the polygon: (a) hexagon, (b) square, (c) triangle.

This method allows to describe both symmetric and non-symmetric polygonal shells without the need of adapting the background grid geometry to the specific polygon or redefining Hamiltonian matrix elements [121, 122]. As a second method, the Kwant software [130] is used to verify the results, giving the same numerical results for the matrix elements, this time using a triangular grid.

The transverse Hamiltonian can be split into three terms:

$$H_t = H^{\text{K}} + H^{\text{B}} + H^{\text{E}}$$

The first element, the kinetic Hamiltonian in the absence of magnetic field, in the basis $|n, j\rangle$ is given by

$$\begin{aligned}\langle nj|H^{\text{K}}|n'j''\rangle \;=\; & T\left[t_r\left(\delta_{n,n'} - \delta_{n,n'+1}\right)\delta_{j,j'} + \right.\\ & \left. t_\phi \delta_{n,n'}\left(\delta_{j,j'} - \delta_{j,j'+1}\right) + \text{H.c.}\right],\end{aligned}$$

where $T = \hbar^2/(2m^* R_{\text{ext}}^2)$ is a reference energy, respectively. R_{ext} is the external radius of the polar grid and also of the polygonal ring [Fig. 2.1(a)]. $t_r = (R_{\text{ext}}/\delta r)^2$, $t_\phi = [R_{\text{ext}}/(r_n \delta\phi)]^2$, δr is the distance between neighboring sites with the same angle and $\delta\phi$ is the angle between adjacent/consecutive sites with the same radius.

The second element is the correction to the kinetic energy due to the magnetic field

$$\langle nj|H^{\text{B}}|n'j'\rangle = T\delta_{n,n'}\left[\frac{1}{2}t_{\text{B}}^2\left(\frac{r_n}{4R_{\text{ext}}}\right)^2\delta_{j,j'} - t_{\text{B}}\frac{i}{4\delta\phi}\delta_{j,j'+1} + \text{H.c.}\right],$$

where $t_{\text{B}} = \hbar e B/m^* T$ is the cyclotron energy in the units of T. And the third element is the contribution of the electric field to the kinetick energy

$$\langle nj|H^{\text{E}}|n'j'\rangle = e\mathbf{E}\cdot\mathbf{r}_n\delta_{n,n'}\delta_{j,j'}.$$

The longitudinal Hamiltonian is

$$H_l = \frac{(-i\hbar\partial_z + eA_z)^2}{2m_{\text{eff}}} \ , \tag{2.3}$$

in this case A_z is the vector potential associated with a magnetic field transverse to the nanowire $\mathbf{B}_\perp = (B_x, B_y, 0)$, which can be chosen at different angles relatively to the corners or sides of the shell.

Finally, the spin Hamiltonian is

$$H_s = -g_{\text{eff}}\ \mu_{\text{B}}\ \boldsymbol{\sigma}\cdot\mathbf{B}\ , \tag{2.4}$$

where g_{eff} is the effective g factor, μ_{B} is Bohr's magneton, $\boldsymbol{\sigma} = (\sigma_x, \sigma_y, \sigma_z)$ denote the Pauli matrices, and $\mathbf{B}$ is the total magnetic field.

The Schrödinger equation

$$H_t\,|a\rangle = \epsilon_a\,|a\rangle\,(a = 1, 2, 3, ...) \tag{2.5}$$

is solved numerically. The diagonalization of H_t provides the coefficients $\psi_a(q)$ which are further used to construct the eigenstates

$$|a\rangle = \sum_q \psi_a(q)\,|q\rangle\,, \tag{2.6}$$

where $|\psi_a(q)|^2$ is the localization probability on the lattice site $q = (x_q, y_q)$ and $|q\rangle = |n_q j_q\rangle$. Next, retaining only a set of low-energy transverse modes, and together with the plane waves in the z direction $|k\rangle = \exp(ikz)/\sqrt{L}$, with k being the wave vector and L the (infinite) length of the nanowire, and with the spin states $s = \pm 1$, the basis in the Hilbert space of the total Hamiltonian, $|aks\rangle$ is formed. In the absence of the magnetic field transverse to the wire ($\mathbf{B}_\perp = 0$), the kets $|aks\rangle$ are eigenvectors of the total Hamiltonian, with eigenvalues $E_{aks} = \epsilon_a + \hbar^2k^2/2m_{\text{eff}} - g_{\text{eff}}\mu_{\text{B}}sB_z$. If $\mathbf{B}_\perp \neq 0$ the transverse motion becomes dependent on k, and then the total Hamiltonian for a discretized series of k values is diagonalized, to obtain its eigenvalues E_{mks} ($m = 1, 2, 3, ...$), and its eigenvectors $|mks\rangle$ expanded in the basis $|aks\rangle$.

2.2 Charge distribution and electron-electron interaction

Having obtained the states with the lowest energies, localized along the edges or in facets of the prismatic shells, the charge density can be computed inside the shell as

$$\rho(\boldsymbol{r}) = e\,(n(\boldsymbol{r}) - n_d) = e\sum_{mks}\mathcal{F}\left(\frac{E_{mks}-\mu}{k_BT}\right)\left[|\langle\boldsymbol{r}|mks\rangle|^2 - n_d\right], \tag{2.7}$$

where $n(\boldsymbol{r})$ is the particle density distribution, $\mathcal{F}(u) = 1/[\exp(u)+1]$ is the Fermi function with $u = (E_{mks}-\mu)/k_BT$, μ stands for the chemical potential, T the temperature, and k_B Boltzmann's constant. The second term of the charge density represents a homogeneus background of ionized donors of density n_d.

Once the charge density distribution is obtained, the electron-electron interaction can be estimated by using the Hartree-Fock approximation (HFA). The Hartree-Fock

self-energy takes the form: $\Sigma_{HF}(\boldsymbol{r_1}, \boldsymbol{r_2}) = \Sigma_H(\boldsymbol{r_1}, \boldsymbol{r_2}) + \Sigma_F(\boldsymbol{r_1}, \boldsymbol{r_2})$, where Σ_H and Σ_F account for the Coulomb and exhange interactions, respectively.

The Hartree (or Columb) term is expressed as

$$\Sigma_H(\boldsymbol{r_1}, \boldsymbol{r_2}) = \delta(\boldsymbol{r_1} - \boldsymbol{r_2}) \int u(\boldsymbol{r_1} - \boldsymbol{r_2})\rho(\boldsymbol{r_2})d\boldsymbol{r_2} = \delta(\boldsymbol{r_1} - \boldsymbol{r_2})V_H(\boldsymbol{r_1}), \tag{2.8}$$

where the integration is performed over the cross section of the shell and $u(\boldsymbol{r} - \boldsymbol{r'}) = e/(4\pi\epsilon_0\varepsilon_r|\boldsymbol{r} - \boldsymbol{r'}|)$ with ϵ_0 and ε_r being the electrical permittivity of the vacuum and the relative permittivity of the material, respectively.

The potential energy then simply takes the form

$$V_H(\boldsymbol{r}) = \int u(\boldsymbol{r} - \boldsymbol{r'})\rho(\boldsymbol{r'})d\boldsymbol{r}, \tag{2.9}$$

and is expressed in the basis of the Hilbert space of the full Hamiltonian as:

$$\langle a_1 k_1 s_1|V_H(\boldsymbol{r})|a_2 k_2 s_2\rangle = \sum_q \psi_{a_1}(q)^* \psi_{a_2}(q)\delta\sigma_{s_1,s_2} V_H(\boldsymbol{r_q}). \tag{2.10}$$

On the other hand, the Fock (or exchange) term is expressed as

$$\Sigma_F(\boldsymbol{r_1}, \boldsymbol{r_2}) = -u(\boldsymbol{r_1} - \boldsymbol{r_2}) \sum_{mks} \mathcal{F}\left(\frac{E_{mks} - \mu}{k_B T}\right) \langle \boldsymbol{r_1}|mks\rangle \langle mks|\boldsymbol{r_2}\rangle . \tag{2.11}$$

The matrix elements $\langle a_1 k_1 s_1|\Sigma_F|a_2 k_2 s_2\rangle$ are shown in the Appendix Section A.1.

The full Hamiltonian is now $H = H_t + H_l + H_s + H_{Int}$, where $H_{Int} = V_H(\boldsymbol{r_1}) + \int \Sigma_F(\boldsymbol{r_1}, \boldsymbol{r_2})d\boldsymbol{r_2}$. The eigenstates are obtained self-consistently by iterating the solutions, i.e., the charge distribution of the non-interacting system is first calculated and then used as a starting point for the interacting system. Then, in each iteration, the charge distribution is recalculated until a convergent solution is reached.

2.3 Charge response under an external time-harmonic perturbation

In order to study the time-dependent response of the charge distribution under a harmonic perturbation we now consider nanowires with finite length. Thus, the longitudinal elements of the basis for the Hilbert space associated with the full Hamiltonian, instead of $|k\rangle$, are now $|n\rangle$, and the complete basis is then

$$|ans\rangle = \sum_q \psi_a(q) f_n(z) \, |qns\rangle , \tag{2.12}$$

where $f_n(z) = \sqrt{\frac{2}{L_z}} \sin\left(\frac{n\pi(z + L_z/2)}{L_z}\right)$, L_z being the length of the nanowire. The eigenstates of the Hamiltonian expressed in this basis are then $|m\rangle = \sum_{ans} \psi_m(a, n, s) \, |ans\rangle$.

The external perturbation can be expressed as follows

$$\delta V_{ext}(\boldsymbol{r}, t) = \mathrm{Re}[\delta V_{ext}(\boldsymbol{r}, \omega) e^{-i(\omega + i\eta)t}], \tag{2.13}$$

where ω is the angular frequency of the external perturbation and $\eta \to 0^+$ is an adiabatic parameter.

The effects of the perturbation in the charge distribution can be obtained using the Liouville equation

$$i\hbar\dot{\rho}(t) = [H + \delta V_{ext}(\boldsymbol{r}, t), \rho(t)], \tag{2.14}$$

where $\rho(t)$ is the time-dependent phase space distribution defined as:

$$\rho(t) = \sum_m p_m(t) \left|m\right\rangle \left\langle m\right|, \tag{2.15}$$

where p_m is the statistical operator that corresponds to the Fermi function in equilibrium. If the perturbation and the charge response are weak, i.e., $\rho(t) = \rho_0 + \delta\rho(t)$ with small $\rho(t)$, the matrix elements $\delta\rho_{mm'}$ of the charge response take the form

$$\langle m|\delta\rho|m'\rangle = f_{mm'}(\delta V_{ext})_{mm'}, \tag{2.16}$$

where $f_{mm'} = \frac{\mathcal{F}_{m'} - \mathcal{F}_m}{\hbar\omega + E_{m'} - E_m + i\hbar\eta}$ and $(\delta V_{ext})_{mm'} = \langle m|\delta V_{ext}|m'\rangle$. If the perturbation is considered to be a uniform electric field along the z-direction, i.e., along the length of the nanowire as $\delta V_{ext} = V_{ext} \cdot z$, the matrix elements are then

$$\langle m|\delta V_{ext}|m'\rangle = V_{ext} \sum_{ans} \sum_{a'n's'} \psi_m(ans){\psi^*}_{m'}(a'n's')\delta_{aa'}\delta_{ss'} \left\langle n|z|n'\right\rangle. \tag{2.17}$$

The matrix elements for a tilted perturbation, i.e., $V_{ext} = V_x x + V_y y + V_z z$, are shown in the Appendix Section A.2.

In equilibrium, the particle density distribution is simply $n(\boldsymbol{r}) = \langle \boldsymbol{r}|\rho|\boldsymbol{r}\rangle$ which using Eq. 2.15, takes the form:

$$n(\boldsymbol{r}) = \sum_{\substack{ans \\ a'n's'}} \psi_a^*(q)\psi_{a'}(q)f_n(z)f_{n'}(z)\delta_{ss'} \sum_m \mathcal{F}_m\psi_m(ans)\psi_m^*(a'n's'). \tag{2.18}$$

On the other hand, the dynamic density response to the external harmonic perturbation is $\delta n(\boldsymbol{r}, \omega) = \langle \boldsymbol{r}|\delta\rho_{mm'}|\boldsymbol{r}\rangle$

$$\delta n(\boldsymbol{r}, \omega) = \sum_{\substack{ans \\ a'n's'}} \psi_a^*(q)\psi_{a'}(q)f_n(z)f_{n'}(z)\delta_{ss'} \sum_{mm'} \psi_m(ans)\psi_{m'}^*(a'n's')f_{mm'}(\delta V_{ext})_{mm'}. \tag{2.19}$$

2.4 Current distributions

The next step of the calculations is to evaluate the electric current along the nanowire in the presence of a voltage bias. The operator describing the contribution of an electron which is localized at the spatial point $\boldsymbol{r}_0$, to the total charge-current density observed in a point $\boldsymbol{r}$, is defined as

$$\boldsymbol{j}(\boldsymbol{r}, \boldsymbol{r}_0) = \frac{e}{2}[\delta(\boldsymbol{r} - \boldsymbol{r}_0)\boldsymbol{v} + \boldsymbol{v}\delta(\boldsymbol{r} - \boldsymbol{r}_0)], \tag{2.20}$$

where $\delta(\boldsymbol{r}-\boldsymbol{r}_0)$ is the particle-density operator and $\boldsymbol{v}(\boldsymbol{r}_0)=\frac{i}{\hbar}[H,\boldsymbol{r}_0]$ is the velocity operator. The expected value of the total charge current flowing in the positive or negative direction along the nanowire (i.e., in the z direction) can be defined as:

$$I_{\pm}=\pm\int_S\left[\sum_{mks}\mathcal{F}\left(\frac{E_{mks}-\mu_{\pm}}{k_BT}\right)\langle mks|\boldsymbol{j}(\boldsymbol{r},\boldsymbol{r}_0)|mks\rangle\right]\mathrm{d}\boldsymbol{r}. \tag{2.21}$$

The integration is performed over the cross section of the shell, practically as a summation over all lattice sites $\boldsymbol{r}_q=(x_q,y_q)$, whereas the scalar product included in the square brackets is an integration over the electron positions $\boldsymbol{r}_0$. Here $\mu_{\pm}$ are the chemical potentials associated with electrons having positive or negative velocity along the nanowire. Obviously, in equilibrium ($\mu_+=\mu_-$) the corresponding currents compensate each other and the total current $I=I_+-I_-$ is zero.

In order to generate a current along the nanowire one has to create an imbalance between the states with positive ($\partial E_{mks}/\partial k>0$) and negative velocity ($\partial E_{mks}/\partial k<0$) by considering in Eq. (2.21) different chemical potentials, μ_+ and μ_-, respectively. The current is thus driven along the nanowire by the potential bias $eV=\mu_+-\mu_-$. This procedure, well established in ballistic transport theory [131], allows to calculate the $I-V$ characteristic and the conductance $G=I/V$ in the small bias limit.

The effects of the disorder in the nanowire are included in two ways. A nanowire of finite length and a random distribution of impurities is considered, assuming that the electron-impurity collisions are elastic (non-dissipative). In this case the impurities can be represented by an extra random term in the total Hamilonian (2.1). The current and the conductance can be calculated using the well known concept of transmission function. Here the transmission function is obtained by using the Fisher-Lee formula [132] and the recursive Green's function method [133]. A summary of the method for cylindrical geometry can be found in the Supplementary Material of Ref. [50]. The (nonequilibrium) Green's function includes a self energy corresponding to the coupling of the nanowires with external contacts.

The second way to estimate the effect of disorder or impurities is by considering a broadening of the energy levels described by a normalized spectral function $A(E)=\frac{1}{\pi}\mathrm{Im}\,\mathcal{G}(E)$, where now the (equilibrium) Green's function $\mathcal{G}(E)$ includes also the effect of electron-impurity scattering in the self-energy. In this study the spectral function for each energy level E_{nks} is modelled as a Gaussian

$$A_{mks}(E)=\frac{1}{\sqrt{2\pi}\Gamma}e^{-\frac{(E-E_{mks})^2}{2\Gamma^2}}, \tag{2.22}$$

whose width parameter Γ represents the disorder energy. This approach corresponds to assuming a statistical collection of impurities in the nanowire and an averaging of the energy spectra resulting from each particular configuration, which was in fact the traditional method to calculate the conductivity of a material before the ballistic transport era [134]. In the present case this method is applicable if the mean free path of the electrons in the nanowire is much smaller than its length. With the ansatz represented by Eq. (2.22), but still assuming a relatively small disorder, the formula for the currents introduced in Eq. (2.21) can be modified by the inclusion of an energy integration of the Fermi function, i.e., by the transformation

$$\mathcal{F}\left(\frac{E_{mks}-\mu}{k_BT}\right)\rightarrow\int A_{mks}(E)\mathcal{F}\left(\frac{E-\mu}{k_BT}\right)dE\ . \tag{2.23}$$

Obviously, for vanishing disorder $\Gamma \to 0$ and $A_{nms}(E) \to \delta(E - E_{nms})$, such that one returns to the ballistic case, Eq. (2.21).

A more rigorous approach in the case with averaged impurity configurations is the traditional Kubo method [134], which allows to calculate the conductivity of the nanowire in the presence of a small potential bias in the z direction (in the linear response regime) by using the matrix elements of the velocity operator and the spectral functions

$$\sigma_{zz} = \frac{he^2}{V}\int dE \left[-\frac{\partial \mathcal{F}}{\partial E}\right] \times \sum_{\substack{m_1 k_1 s_1 \\ m_2 k_2 s_2}} |\langle m_1 k_1 s_1 | v_z | m_2 k_2 s_2 \rangle|^2 A_{m_1 k_1 s_1}(E)\ A_{m_2 k_2 s_2}(E)\ , \tag{2.24}$$

where V denotes the volume of the conductor. The Kubo formula describes the conductivity in the non-ballistic and, in principle, dissipative case, which should be realistic for long nanowires.

2.5 Radiated electromagnetic fields

With the method described above the current density $\boldsymbol{J}$ inside the shell is

$$\boldsymbol{J}(\boldsymbol{r}) = \sum_{mks} \mathcal{F}\left(\frac{E_{mks} - \mu}{k_B T}\right) \langle mks | \boldsymbol{j}(\boldsymbol{r} - \boldsymbol{r}_0) | mks \rangle. \tag{2.25}$$

Two different values, harmonically time-dependent, are considered for the chemical potential μ_+ and μ_- of carriers with opposite velocities, with $\mu_\pm = \mu_s \pm V \sin(\omega t)$, where ω is the frequency, V the bias amplitude and μ_s is the static chemical potential, which is determined by the carrier density at equilibrium.

Once obtained the current density distribution, the time dependent vector potential is calculated outside the nanowire as

$$\boldsymbol{A}(\boldsymbol{r}, t) = \frac{\mu_0}{4\pi} \int \frac{\boldsymbol{J}(\boldsymbol{r'}, t)}{|\boldsymbol{r} - \boldsymbol{r'}|} \mathrm{d}\boldsymbol{r'}\ , \tag{2.26}$$

here μ_0 is the vacuum permeability and the integration is performed inside the shell. We assume $r \ll L$ to properly obtain the vector potential. Having obtained the vector potential it is straightforward to obtain the electromagnetic radiated field using the relations

$$\boldsymbol{E} = -\frac{\partial \boldsymbol{A}}{\partial t} \text{ and } \boldsymbol{B} = \nabla \times \boldsymbol{A}. \tag{2.27}$$

The next step is to estimate the frequency domain which is to consider with this method. Typical nanowires made of semiconductor materials such as InAs, InP or GaAs have electron mobilities μ_e in the range of 400-6000 cm^2/(Vs), with scattering times in the range of tens of femtoseconds [135, 136]. Thus, for frequencies in the RF domain, from kHz to GHz, achievable within an electric circuit connected to the nanowire, the electron damping and losses in the semiconductor nanowire to the static the resistivity are negligible, and it is possible to ignore the dynamic corrections.

We are mostly interested in the angular distribution of the radiated field around the nanowire, and for this purpose the frequency plays no quantitative role. Hoewever,

it affects the power density, which - in principle - is proportional to the frequency squared. The power density of the radiated field is thus evaluated with the time-averaged Poynting vector

$$\overline{\boldsymbol{S}}(\boldsymbol{r}) = \frac{1}{T}\int_0^T \frac{1}{\mu_0}(\boldsymbol{E}(\boldsymbol{r},t)\times\boldsymbol{B}(\boldsymbol{r},t))\,dt\ . \tag{2.28}$$

2.6 Excitons

We now consider the transverse states of electrons confined in the shell of a CSN. These are the states of a polygonal ring with a lateral thickness in the (x,y) plane given by the width of the shell and with a short height in the growth direction, z, such that all electrons are in the lowest vertical (or longitudinal) mode. These are also the relevant states for the excitons created in an infinitely long nanowire at wavevector $k=0$ in a material with direct band gap. Using the same discretization method as described in Section 2.1, the single-particle Hamiltonian is now taken to be

$$H = H_v + H_c, \tag{2.29}$$

and describes the electrons in the valence (H_v) and the conduction band (H_c), respectively. Assuming that the zero energy level corresponds to the top of bulk valence band, each component takes the form

$$H_i = \frac{(-i\hbar\nabla + e\boldsymbol{A})^2}{2m_i^*} + \delta_{c,i}E_b - g_i^*\mu_B\sigma_z B - e\boldsymbol{E}\cdot\boldsymbol{r}, \tag{2.30}$$

where the subscript $i = v,c$ refers to one of the two bands; $m_{v,c}$ and $g_{v,c}$ are the effective masses of the electrons and the g-factors in the valence and the conduction band, respectively; E_b is the (bulk) semiconductor band gap; μ_B the Bohr magneton; e the electron charge; and σ_z stands for the Pauli matrix, $\boldsymbol{A} = B[-y,x,0]/2$ is the vector potential of an external uniform magnetic field (B) in the longitudinal z direction. A uniform electric field in the plane (x,y), making an angle ϕ with the x axis, $\boldsymbol{E} = E[\cos(\phi),\sin(\phi),0]$, is also considered in order to break the geometric symmetry of the polygons and show the electron arrangements within samples.

The single-particle eigenstates are now $|\Psi_{i,a}\rangle = \sum_q \psi_i(q,a)\,|q\rangle$ where $\psi_i(q,a)$ are the amplitudes of the eigenvectors in the polar basis $|q\rangle$.

In the second quantization approach the multielectron Hamiltonian of interacting electrons is

$$\hat{H} = \sum_a E_a a_a^\dagger a_a + \frac{1}{2}\sum_{abcd} V_{abcd} a_a^\dagger a_b^\dagger a_d a_c, \tag{2.31}$$

where $E_a \equiv E_{ia}$ are the single-particle eigenvalues, $a_a^\dagger$ and a_a are the electronic creation and annihilation operators acting on particles in the single-particle eigenstate $|\Psi_a\rangle \equiv |\Psi_{i,a}\rangle$, and V_{abcd} are the Coulomb integrals

$$V_{abcd} = \langle\Psi_{i,a}\Psi_{j,b}|\,\frac{e^2}{4\pi\varepsilon_r\varepsilon_0|\boldsymbol{r}-\boldsymbol{r'}|}\,|\Psi_{i,c}\Psi_{j,d}\rangle\,, \tag{2.32}$$

here ε_r is the material dielectric constant, ε_0 the vacuum permittivity and $|\boldsymbol{r}-\boldsymbol{r'}|$ the spatial separation of two electrons. We exclude the cases for which the positions $r = r'$ in the grid in order to avoid singularities.

The multi-electron eigenvalues $\mathcal{E}_\alpha(\alpha = 1, 2, 3, ...)$ and eigenstates $|\Phi_\alpha\rangle$ are obtained by numerical diagonalization of $\hat{H}$ in a truncated Fock space constructed of N_v valence and N_c conduction band single-particle eigenstates. If there are N electrons confined in the system, then the basis consists of $(N_v + N_c)!/[N!(N_v + N_c - N)!]$ eigenstates of the non-interacting system (Slater determinants in 'built string' representation) of the form:

$$|\mu\rangle = |v_1^\mu v_2^\mu \cdots v_{N_v}^\mu c_1^\mu c_2^\mu \cdots c_{N_c}^\mu\rangle\,, \tag{2.33}$$

where $v_a^\mu = [0, 1]$ and $c_a^\mu = [0, 1]$ are the occupation numbers of the single-particle states in the valence ($|\Psi_{v,a}\rangle$) and the conduction ($|\Psi_{c,a}\rangle$) bands, respectively. Since the analysis is restricted to single excitons, the basis $|\mu\rangle$ is reduced to states for which $\sum_i v_i^\mu \geq N_v - 1$. The multi-electron eigenstates are linear combinations of these states

$$|\Phi_\alpha\rangle = \sum_\mu \phi(\mu, \alpha)\,|\mu\rangle\,, \tag{2.34}$$

with $\phi(\mu, \alpha)$ being the amplitude of the multi-electron eigenstates in the basis μ. It is then assumed that most of the valence levels are occupied and the electrons may be excited to the conduction band from few (N_v) top valence states.

2.7 Light scattering

The scattering of electromagnetic waves by particles has been a topic which has drawn the interest of physicists over the last two centuries. Any scattering of electromagnetic waves occurs as the result of an excitation (of a heterogeneity at molecular or molecular aggregations scale) followed by reradiation. The same physics underlies any scattering phenomena regardless of the type of heterogeneity: when light illuminates an obstacle (electrons, atoms, etc.), the electromagnetic field sets the electric charges into oscillatory motion and thus, they re-radiate electromagnetic waves in all directions. This secondary radiation is called the scattered field.

In particular, the scattering of light by spherical particles was first rigorously described by Gustav Mie in 1908. He provided the solution to Maxwell's equations for the scattering of plane waves restricted to the boundary conditions of a homogeneous sphere. The solution takes the form of an infinite series of multipole expansion (of electric and magnetic nature) in terms of Legendre polynomials and Bessel functions.

In any scattering problem, the total electromagnetic wave can be decomposed into the incident and the scattered contributions:

$$\boldsymbol{E} = \boldsymbol{E}_{inc} + \boldsymbol{E}_{sca}, \qquad \boldsymbol{H} = \boldsymbol{H}_{inc} + \boldsymbol{H}_{sca}. \tag{2.35}$$

The Maxwell's wave equation can then be solved for the scattered field only

$$\nabla \times \left(\frac{1}{\mu_r}\nabla \times \boldsymbol{E}_{sca}\right) - k_0^2\left(\varepsilon_r - j\frac{\sigma}{\omega\varepsilon_0}\right)\boldsymbol{E}_{sca} = 0, \tag{2.36}$$

where ε_0 is the permittivity of the vacuum and ε_r and μ_r are the relative permittivity and permeability of the scattering medium, respectively. The magnetic field can be obtained using Faraday's law

$$\boldsymbol{H}_{sca} = -\frac{1}{j\omega\mu}\nabla \times \boldsymbol{E}_{sca}, \tag{2.37}$$

and the energy flux is given by the time-average Poynting vector for harmonic fields:

$$\boldsymbol{\mathcal{P}} = \frac{1}{2}\mathrm{Re}\left[\boldsymbol{E} \times \boldsymbol{H}^{*}\right]. \tag{2.38}$$

Taking into account that the electric and magnetic fields are related

$$\boldsymbol{H}_{inc} = \frac{1}{\eta}\left|\boldsymbol{E}_{inc}\right|^{2}\hat{\boldsymbol{k}}, \tag{2.39}$$

where $\hat{\boldsymbol{k}}$ is the versor pointing in the direction of the incident wave propagation and $\eta = \sqrt{\mu/\varepsilon}$ is the impedance. The energy flux of the incident plane wave can be calculated accordint to

$$\boldsymbol{\mathcal{P}}_{inc} = \frac{1}{2}c\varepsilon\left|\boldsymbol{E}_{inc}\right|^{2}\hat{\boldsymbol{k}}, \tag{2.40}$$

where $c = \sqrt{1/\mu\varepsilon}$ is the speed of light.

We define the scattering cross section as the rate at which the electromagnetic energy passes the surface of an imaginary surface enclosing the scatterer divided by the incident energy flux

$$\sigma_{sca}\,[\mathrm{m}^2] = \frac{W_{sca}\,[\mathrm{W}]}{\boldsymbol{\mathcal{P}}_{inc}\,[\mathrm{W/m}^2]}. \tag{2.41}$$

The scattered energy can be derived by performing an integration of the Poynting vector over the surface enclosing the scatterer

$$W_{sca} = \oiint_{S} \boldsymbol{\mathcal{P}}_{sca} \cdot \boldsymbol{n}\mathrm{dS}. \tag{2.42}$$

Finally, by dividing σ_{sca} by the geometrical cross section, i.e., the area of the scatterer perpendicular to the direction of the incoming light, we obtain the normalized scattering cross section

$$\sigma_{n} = \frac{\sigma_{sca}\,[\mathrm{m}^2]}{\sigma_{geom}\,[\mathrm{m}^2]}. \tag{2.43}$$

In this work the normalized scattering cross section of nanowires, illuminated transversally with plane electromagnetic waves having TE and TM polarizations, is calculated numerically using the finite elements method implemented in the Wave Optics Module of the software Comsol Multiphysics (version 5.4) [128].

The results are arranged into two subsets. In the first one, cylindrical nanowires with an internal gap (tubular nanowires or nanotubes) are studied and, in the second one, prismatic nanowires with polygonal (triangular, square and hexagonal) cross section are addressed.

In the first part, the simulation domain consists of a quadrant of a sphere with 1200 nm radius in which a quarter of the nanowire, cut by two symmetry axes, is embedded in the center. The sphere consists of an outer perfectly-matched layer (PML) of 400 nm thickness and the inner space where the nanowire is located. Boundary conditions are imposed (perfect electric conductor [PEC] and perfect magnetic conductor [PMC]) on the facets of the quadrant for the background electromagnetic field according to the chosen polarization of the incident light (Fig. 2.2). First, short cylinders are considered, with the length of $L = 150$ nm, and external radius $R_{\mathrm{ext}} = 100$ nm.

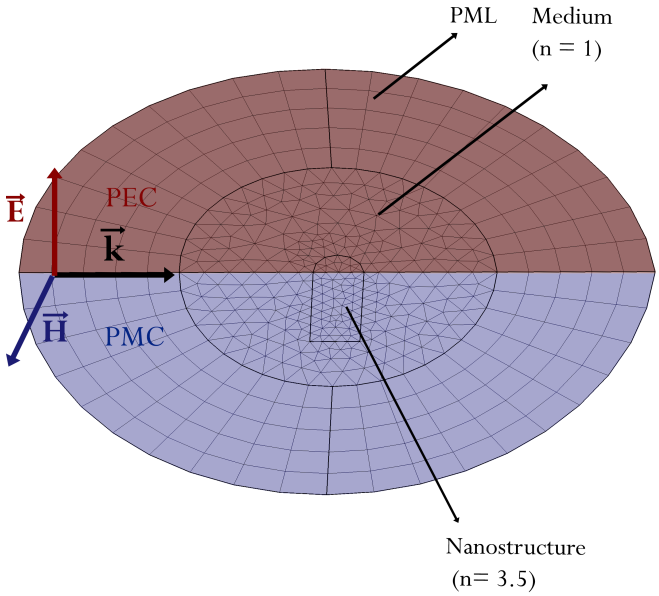

Figure 2.2: Sketch of the problem in COMSOL

The cylinders have a tubular shape, with a constant external radius (R_{ext}) and the internal one (R_{int}) varying between zero and R_{ext}. The spectral dependence of the normalized scattering cross section is studied in the wavelength range of $\lambda = 400 - 800$ nm. Further, longer nanowires, i.e., of length $L = 600$ nm are considered, and the calculations are repeated for the scattering cross section for incident light wavelengths up to $\lambda = 1000$ nm. Finally, the spectra for the constant value of the aspect ratio $R_{\text{int}}/R_{\text{ext}} = 1/2$, and variable external diameter ($2R_{ext}$) are obtained. The results are compared with the spectra obtained for the bulk nanowire.

In the second part, the simulation domain consists now of a full sphere with 800 nm radius which has an outer perfectly-matched layer of 400 nm thickness, with the nanowire located at the center of the sphere. Prismatic nanowires of hexagonal square, and triangular cross section, are considered with radii between 100-250 nm, in the optical/near-infrared range, where the wavelength is several times larger than these values. The length of the nanowires varies between values comparable with the radius up to several times larger. The symmetry of the nanowires could still be taken advantage of in order to optimize the computational time of the scattering cross sections, but in this case the full sphere is needed as effects of changing the angle of incidence in the directivity are studied.

Additionally, the asymmetry parameter g, which is defined as the mean direction of the scattered light (Eq. 2.44), is calculated in each case in order to be able to compare the average directivity of each structure as a function of the wavelength

$$g = \langle \cos(\theta) \rangle = \frac{\oiint_S \cos(\theta)(\boldsymbol{\mathcal{P}}_{sca} \cdot \boldsymbol{n}) \mathrm{dS}}{\oiint_S (\boldsymbol{\mathcal{P}}_{sca} \cdot \boldsymbol{n}) \mathrm{dS}}, \tag{2.44}$$

where $\cos(\theta) = \boldsymbol{n} \cdot \hat{\boldsymbol{k}}$, $\boldsymbol{n}$ being the vector normal to the surface S and $\hat{\boldsymbol{k}}$ the direction of the incident light. The asymmetry parameter is equal to zero when the particle either scatters isotropically or symmetrically with respect to an angle $\theta = \pi/2$. The

asymmetry parameter is positive if the nanostructure scatters more light in the forward direction ($\theta = 0$) and negative if it scatters more in the backward direction ($\theta = \pi$).

For all examples of nanowires, the same refractive index is used $n = 3.5$, corresponding to GaP at $\lambda = 530$ nm [137]. The surrounding medium is air, i.e., refractive index $n = 1$. The meshing maximum size is chosen to be a sixth of the wavelength in each material $\lambda/6n$ and the Maxwell equations are solved for the scattered field in the far-field approximation. Since our interest lies in the effects of the geometry, the absorption is neglected in all cases.

For prismatic nanowires the spectra are expected to differ from the ones obtained for a cylinder of the same dimensions (radius and length), due to the change of geometry and the decrease of the effective scattering volume. For ease of comparision, a rescaling of the dimensions is then carried out in order to obtain the main resonant scattering modes in each case for the same wavelengths.

Chapter 3

Results

3.1 Transverse quantum states of polygonal core-shell nanowires

The first step in order to study the charge and current distribution in the nanowires is to obtain the quantum states of the systems, i.e., the wave functions and the energy levels. Since the nanowires have infinite length in the model, the quantum states are to be calculated only in the transversal cross-section. In this section, the energy levels and the probability distributions of the transverse states are presented, both for symmetric and asymmetric shapes.

3.1.1 Symmetric geometry

In the examples shown in this subsection the external radius of the polygonal shell, which is the distance from the center to one corner, as indicated in Fig. 2.1(a), is $R_{\text{ext}} = 30$ nm, whereas the side thickness $t = 6$ nm. The numerical calculations were performed for InAs bulk parameters, which are $m_{\text{eff}} = 0.023m_{\text{e}}$ (m_{e} being the electron mass of a free electron), and $g_{\text{eff}} = -14.9$.

Because of the polygonal cross section of the shell the lowest transverse modes are localized in the corners of the polygons while the probability distributions corresponding to higher modes have maxima on the sides [121]. For each polygon there are $2N$ corner states, where $N = 6, 4, 3$ is the number of corners (or sides) and the factor 2 accounts for the spin, as it is shown in Fig. 3.1. The energy dispersion of corner states decreases with the number of corners. For a 6 nm thick shell these states fit into the intervals 15.3 meV for the hexagon, 3.1 meV for the square, and 0.2 meV for the triangle (measured from the ground state). For each geometry, above the group of corner states, there is another group of $2N$ states, localized on the sides of the polygons (the lower part of Fig. 3.2). For the radius and thickness used, the energy dispersion within each group of corner and side states is exceeded by the energy interval (or gap) between these groups, which are $\Delta_{\text{h}} = 21.2$ meV for hexagonal, $\Delta_{\text{s}} = 34.4$ meV for square and $\Delta_{\text{t}} = 87.1$ meV for triangular cross sections. The probability distribution associated with corner and side states is illustrated in Fig. 3.2.

These energy gaps distinguish polygonal from cylindrical shells. In the latter case, if $t \ll R_{\text{ext}}$, one expects the transverse energies $\varepsilon_m = \hbar^2 m^2 / 2m_{\text{eff}} R_{\text{ext}}^2$, with $m = 0, \pm 1, \pm 2, ...$ the quantum number of the angular momentum, i.e., with energy intervals uniformly increasing as m^2. In addition, in the cylindrical case (not shown in Fig. 3.2),

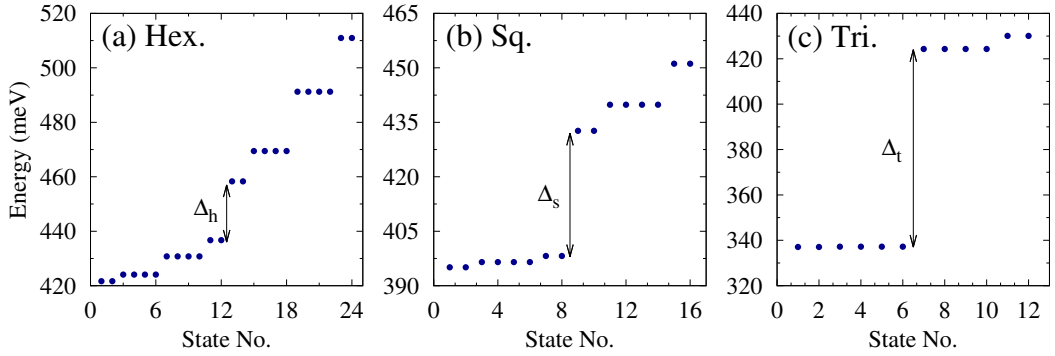

Figure 3.1: Single-particle energies associated with corner and side states of (a) hexagonal, (b) square, and (c) triangular shells. The arrows indicate the energy separation between the groups of corner and side states.

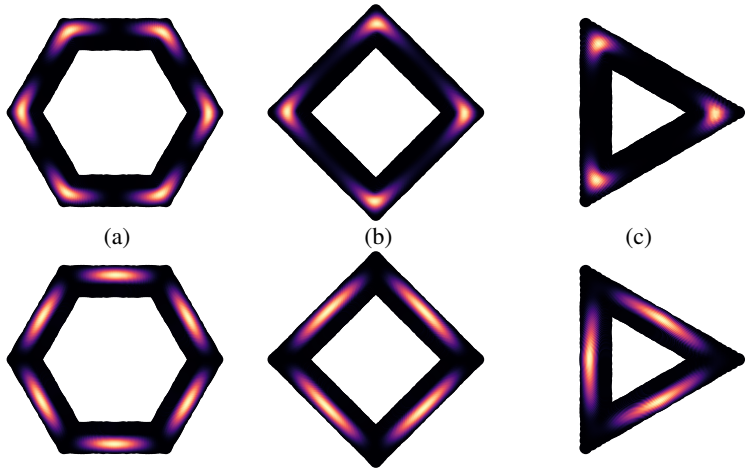

Figure 3.2: Single-particle probability distributions associated with the low-energy transverse modes of (a) hexagonal, (b) square, and (c) triangular shells. The top figures illustrate the corner states, which include the ground state, and the bottom figures illustrate the next, higher-energy group of modes, localized on sides. The energy separation between corner and side modes is indicated in Fig. 3.1.

at zero magnetic field, the transverse modes are four fold degenerated, both spin and orbital, except the ground state which is only two fold, spin degenerate. For symmetric polygons, because of the reduced, discrete symmetry, the orbital degeneracy is lifted between consecutive groups of $2N$ transverse states. In particular, for symmetric shells, the sequence of degeneracy orders (2-fold or 4-fold) of the corner/side states, with increasing the energy, is 2442/2442 for the hexagon, 242/242 for the square, and 24/42 for the triangle.

3.1.2 Asymmetric geometry

Even if it is possible to achieve a high degree of precision with the current state-of-the-art fabrication technologies, perfectly symmetric wires are still impossible to obtain. CSNs are usually grown in sets of close-by vertical cores, later covered with layers of different materials. Due to the screening of neighboring wires, the shell thickness varies along the cross section circumference making it very difficult to obtain

shells of constant thickness [138, 139]. In general, the corner localization is very sensitive to the ring symmetry and to the size of the corner area [122].

In the examples of this subsection two cases of hexagonal shells are considered, one in which one of the sides is thinner than the others, and another in which angular deformations are studied. The dimensions in the examples that follow are $R_{\text{ext}} = 60$ nm and $t = 10$ nm, and the effective mass considered here corresponds to the bulk InSb, ie.,$m_{\text{eff}} = 0.014m_{\text{e}}$. This subsection is a part of the results published in Ref. [123].

3.1.2.1 Different side thickness

Symmetric hexagonal shells where one of the sides is thicker than the others have been previously studied [140]. Here, the opposite case, i.e., the situation when one of the sides is thinner than the other ones, is considered. In this case, electrons are depleted from the thinner side and the structure acts as a system with five facets, now with eight corner states separated from the group of side states, Fig. 3.3(a). The low-energy states are distributed between the four larger corner areas [Figs. 3.3(b-c)], while the electrons excited to the higher levels are delocalized over the five sides, Fig. 3.3(d). As expected, the probability distributions corresponding to both types of states do not reproduce the symmetry of the sample, but only the mirror symmetry with respect to the thinnest side.

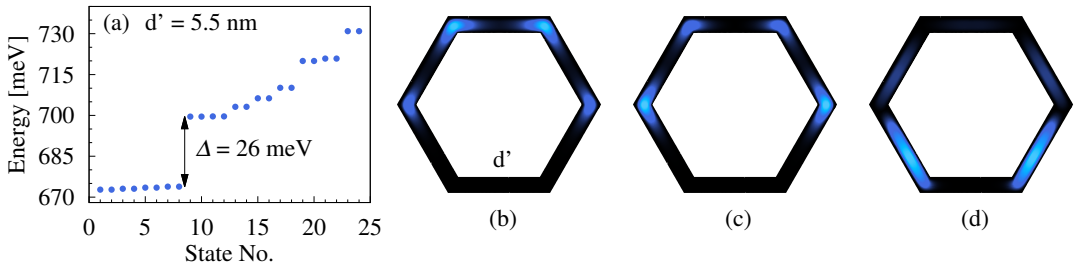

Figure 3.3: Single-particle energies for a hexagonal cross section with one thinner side [side d' in Fig. (b)] (a), and the examples of the corresponding probability distributions: ground state (b), first excited state (c) and first side state (d)].

3.1.2.2 Angular deformations

Hexagonal cross sections with angular deformations, which include star-shaped polygons which have been recently obtained [141], are considered. In order to reproduce these deformations, three alternating external radii (R_1) are left unchanged while the other radii (R_2) are reduced (Fig. 3.4). As a result, the system is now threefold rotationally symmetric. The corner domain is now split into two groups of corner states, separated by a gap (δ) comparable to the corners-sides separation (Δ) for small differences between the two radii [Fig. 3.4(a)]. The probability distributions corresponding to the lowest states are localized around the sharpest corners [Fig. 3.4(b)] while those associated with the second group of corner states form three maxima residing in the larger corner areas [Fig. 3.4(c)]. These relatively small differences of the corner areas do not affect the side localization, which remains symmetric, [Fig. 3.4(d)].

A smaller ratio R_2/R_1 results in the sharpening of three corner areas and softening of the alternating ones. This considerably increases the separation between the corner

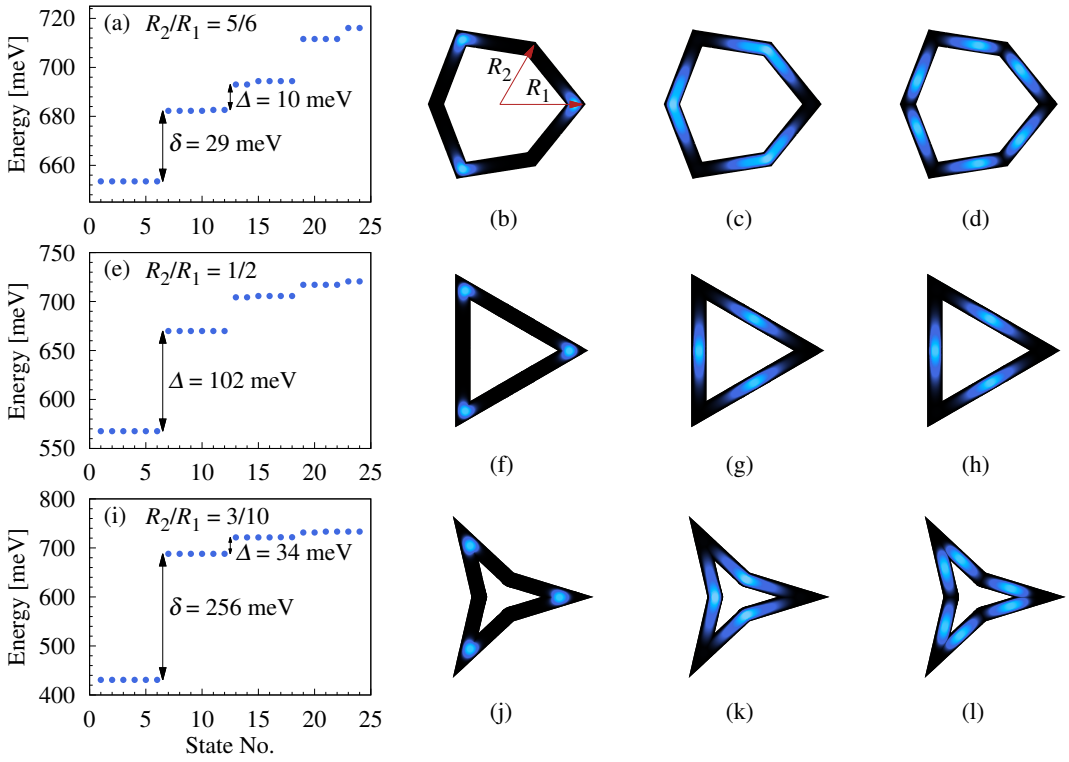

Figure 3.4: Single-particle energies for InSb rings with different ratios of the neighboring external radii R_2/R_1 (first column), and the probability distributions corresponding to the ground state (second column), the second corner level (third column), and the lowest side level (fourth column).

states (δ) such that it becomes the dominant gap of the spectrum, while the separation of the corner from side states slightly decreases. For $R_2 = R_1/2$ the triangular shape is recovered, where the lowest states are strongly localized in the corners [Fig. 3.4(f)], while the probability distributions associated with the two lower side states form maxima centered on the sides [Fig. 3.4(g,h)].

Further decreasing the ratio, such that $R_2 < R_1/2$, results in star-like structures where the gap separating the corner from side states (Δ) slightly increases while the lower gap (δ) now exceeds it by nearly one order of magnitude [Fig. 3.4(i)]. The formation of six quasi-degenerate corner-states is now observed, well-separated from the higher, formally of corner-type, states but spatially elongated similarly to the side states of triangular rings [Fig. 3.4(k)]. The second group of side states splits again into the six sides of the structure [Fig. 3.4(l)].

3.2 Conductance features determined by the geometry

In this section the effects of an external magnetic field in the conductance of the nanowires are presented. Once the quantum states of the system are obtained, the charge and current distributions, through which we obtain the conductance, can be calculated using the methods described in Chaper 2. Several features of the conductance steps for polygonal CSN which are consequences of the internal geometry of the

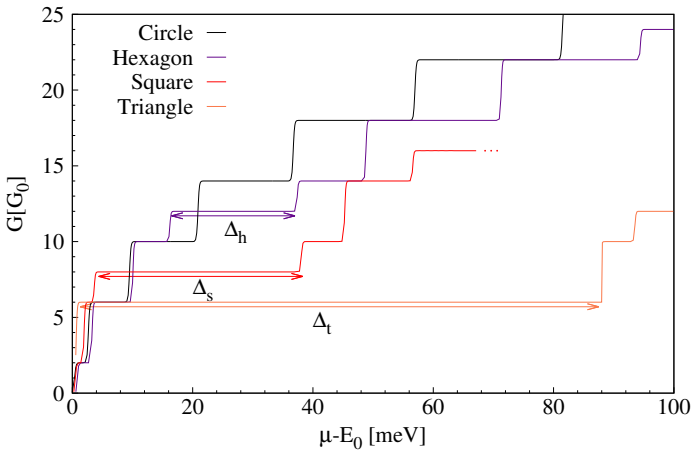

Figure 3.5: Conductance steps expected for tubular nanowires of circular and polygonal cross sections, versus the chemical potential μ adjusted by subtracting the ground state energy E_0. $\Delta_{h,t,s}$ indicate the energy separation between the corner and side modes for hexagon, square, and triangle, respectively. The conductance is represented in units of $G_0 = e^2/h$. Here $t = 6$ nm

nanowires are presented. The results presented in this section are an excerpt from Ref. [142].

In the examples that follow the external radius of the polygonal shell is $R_{\text{ext}} = 30$ nm, whereas the side thickness t varies between 2-8 nm. The numerical calculations were performed for InAs bulk parameters, which are $m_{\text{eff}} = 0.023 m_{\text{e}}$ and $g_{\text{eff}} = -14.9$.

In Fig. 3.5 the conductance steps expected in the cylindrical and in the three prismatic geometries are compared, when the chemical potential μ is varied. Here quasi-ballistic transport and symmetric shells are assumed. The steps obtained for circular and hexagonal structures are visibly different, with an extra plateau at $12G_0$ for the hexagon, ($G_0 = e^2/h$) corresponding to the gap between corner and side states. These plateaus increase dramatically for the square and triangular geometries, at $8G_0$ and at $6G_0$, respectively. For the hexagonal shell the corner states induce steps at $2G_0$, $6G_0$, and $10G_0$, similar to the circular case. For the square, instead, only some shoulders indicating the corner states are seen at $4G_0$ and for the triangular case they are not resolved. The energy gaps between corner and side states are (as in Section 3.1.1) $\Delta_{\text{h}} = 21.2$ meV for hexagon, $\Delta_{\text{s}} = 34.4$ meV for square and $\Delta_{\text{t}} = 87.1$ meV for triangle.

In order to obtain the conductance of a nanowire of finite length with impurities, scattering centers are considered at random locations within the tubular nanowire with random characteristic energy between 0.0 and 0.5 meV. The conductance is calculated this time with the recursive Green's function approach on the example of the triangular geometry, at zero temperature. The results are shown in Fig. 3.6, for a nanowire of 54.2 nm length, with different impurity concentrations corresponding to a mean distance between the nearest neighbors of 2.7 nm, 1.6 nm, and 1.2 nm. The impurity configurations are fixed in these cases, such that this situation corresponds to a specific mesoscopic sample with individual randomness. The impurity concentration is increased until the largest plateau, corresponding to the gap between the corner and side states, nearly disappears. This impurity concentration can offer a hint on how dirty a nanowire can be such that the conductance steps cannot be detected

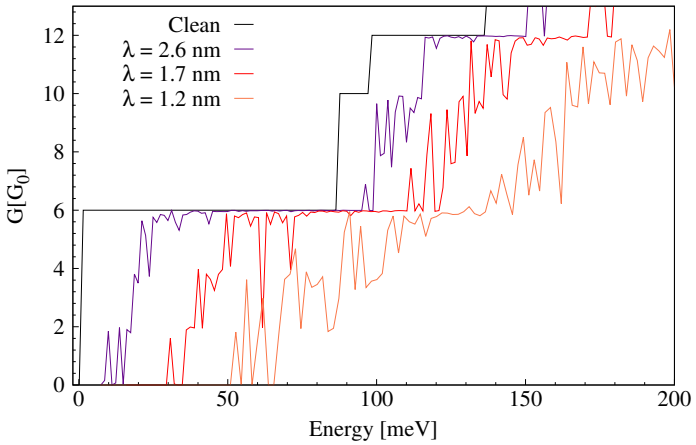

Figure 3.6: Conductance steps expected for the triangular nanowire for different impurity concentrations characterized by the mean distance between the nearest neighbors. The potentials associated with the impurities are repulsive and of a random strength between 0 and 0.5 meV.

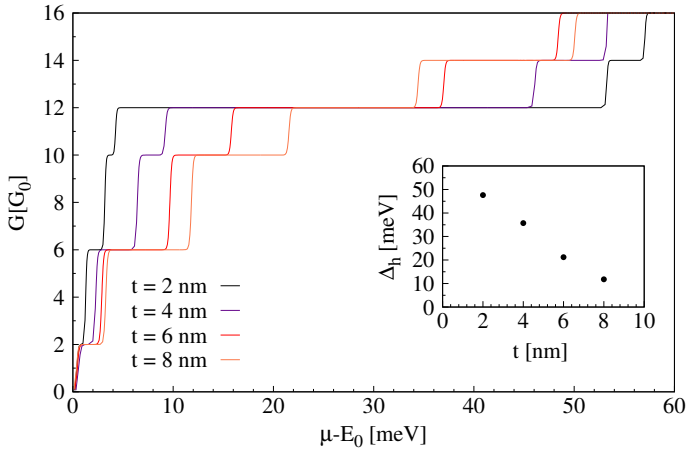

Figure 3.7: Dependence of the conductance plateaus on the side thickness t for the hexagonal shells. Decreasing the side thickness leads to a significant increase of the plateau between the corner and side states, at $12G_0$, and to a decrease of all the other plateaus.

in the experiments. It is instructive to mention that, by generating several impurity configurations, for the same geometry, and averaging the results for the conductances, similar results to those based on the Gaussian spectral function could be obtained (not shown).

We now return to the clean nanowire, to discuss the effect of the side thickness on the hexagonal geometry. With the parameters used in Fig. 3.5 the plateaus corresponding to side modes, i.e. above $12G_0$, are comparable or larger than Δ_h. However, the relative magnitude of the energy intervals, i.e., of Δ_h relatively to the dispersion of the corner and side states, increases with reducing the aspect ratio of the polygon, i.e., t/R_{ext} [122]. As a result, with reducing the thickness parameter t, while $R_{\rm ext}$ is kept constant, the plateau at the transition between corner and side states (at $12G_0$) becomes much more prominent. At the same time the ratio between Δ_h and the other energy intervals rapidly increases such that the plateaus in the corner domain become negligible relatively to the main one of width Δ_h, as shown in Fig. 3.7.

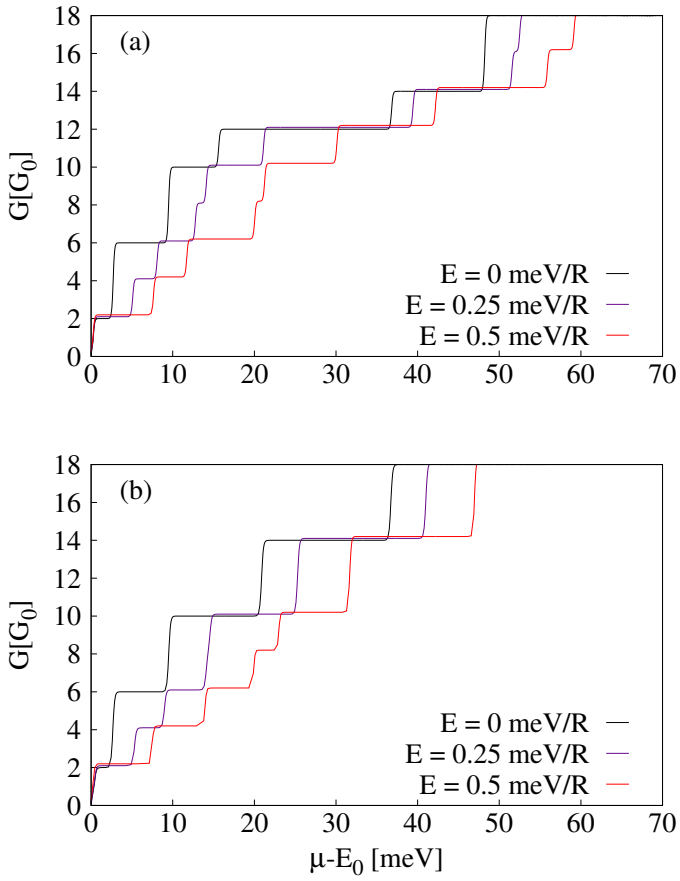

Figure 3.8: Conductance steps in the presence of an asymmetry induced by an electric field parallel to the x-axis for the hexagonal case (a) and the cylindrical one for comparison (b). The orbital gaps are split and the gap between corner and side states for the hexagonal geometry is reduced, yielding to shorter plateaus at $12G_0$. Here $t = 6$ nm

In these examples the geometric symmetry of the nanowires is assumed. Nevertheless, shells with perfect polygonal symmetry cannot be fabricated, such that the symmetric case should be seen only as a reference case. Geometric imperfections, random impurities, or external electric fields remove the orbital degeneracies. In order to account for asymmetry an electric field transversal to the wire is considered. In practice, this is a way to model also the effect of a lateral gate attached to the nanowire, or of the substrate where the nanowire is situated, typically used to control the carrier concentration with a voltage [121]. Assuming this voltage is not very large, such that the electrons are still distributed over the entire shell (and not simply crowded near the gate), new plateaus can be obtained between the split orbital states, as shown in Fig. 3.8.

The electric field changes the electron distribution by favoring some corner or sides over the others, depending on its orientation. This allows for the controllability of the electron localization within the shell. Although the first plateaus are similar for both the cylindrical and the hexagonal case, the main difference arises from the orbital degeneracy pattern of the hexagonal nanowire, which is split at $12G_0$, separating corner from side states (2442/2442). It is also interesting to observe that, in the cylindrical nanowire, the electric field applied needs to be progressively stronger in order to split

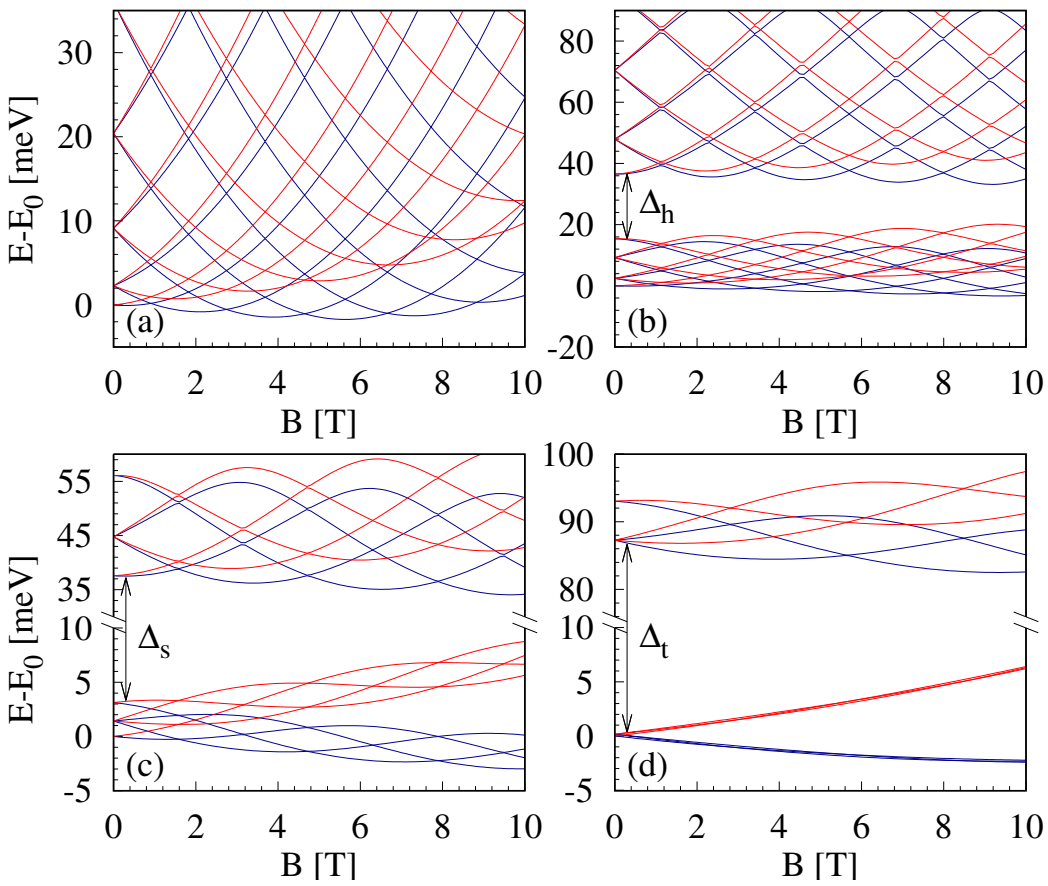

Figure 3.9: Evolution of the transverse energy modes with magnetic field for the circular shape (a) and for the three polygonal shapes: (b) hexagonal, (c) square and (d) triangular. The red color stands for the spin down levels and the blue for the spin up ones. Here $t = 0.2R_{ext}$. Note that, in order to include both corner and side states in the graphs, the vertical axes in panels (c) and (d) are broken.

the orbital degeneracy of higher energy levels, as shown in 3.8(b). Additionally, for the hexagonal wire, rotating the direction of the electric field leads to a change in the secondary plateaus but leaves the main one (at $12G_0$) unaffected (not shown).

3.2.1 Effects of a longitudinal magnetic field

An external longitudinal magnetic field is now considered and its impact on the transverse modes is studied. For a circular nanowire with $t \ll R_{\text{ext}}$ a periodic energy spectrum vs. the magnetic field is expected, with period of one flux quantum in the cross sectional area. Such flux-periodic oscillations, related to the Aharonov-Bohm interference, have been observed experimentally for InAs/GaAs hexagonal core-shell nanowires with $t = 25$ nm and $R_{\text{ext}} \approx 75$ nm [56]. The oscillations had additional modulations that were attributed to impurities, or subsequently to the spin splitting, by using a circular nanowire model of zero thickness [57].

Indeed, the presence of the spin disturbs or breaks the flux periodicity of the transverse modes when the magnetic field increases, as seen in Fig. 3.9(a) for a circular shell. In addition the flux periodicity is also disturbed by the shell thickness. Flux periodic energy spectra for thin polygonal shells, without spin effects, have already been obtained by other authors [40, 143, 144].

In Fig. 3.9(b) the energies of the transverse modes for the hexagonal shell are shown. Remarkably, the gap between the corner and side states survives at high magnetic fields [144], in this case even above 10 T. The reason is that the orbital energy of the states localized in corners is significantly reduced compared to states of higher energies, an effect that becomes more pronounced in the square geometry, Fig. 3.9(c). In fact, the differences reveal the symmetry reduction from circular to hexagonal or square shapes. In these examples the orbital degree of freedom of the corner states is provided by their mutual coupling via tunneling across the polygon sides. Instead, in the triangular case, where the corner localization is the strongest, the tunneling is suppressed, and the orbital motion of the corner states is completely frozen, such that only the spin Zeeman energy is observable for the corner states in. Fig. 3.9(d).

The conductance steps expected in the presence of a longitudinal magnetic field (shown in Fig. 3.10) develop according to the evolution of the transverse modes when increasing the field, by lifting both spin and orbital degeneracies. It is worth noting that, up to 10 T, the gap separating corner and side states prevails for the three polygonal shells, with the geometric parameters used, and that a new gap separating the corner states with different spin is created as a consequence of the Zeeman splitting for the triangular and square nanowires, where the orbital degree of freedom is most restricted.

3.2.2 Effects of a magnetic field perpendicular to the nanowire

3.2.2.1 Charge and current distributions

A magnetic field orthogonal to the nanowire axis creates a second localization mechanism, in addition to the localization imposed by the polygonal geometry. This type of magnetic localization has been studied in recent years for the cylindrical shell geometry by several authors [59, 60, 145–147]. If the electrons are confined on a cylindrical surface, their orbital motion is governed by the radial component of the magnetic field. Assuming a magnetic field uniform in space, its radial component vanishes and changes sign along the two parallel lines on the cylinder situated at $\pm 90^\circ$ angles relatively to the direction of the field, and if the field is strong enough the electrons have snaking trajectories along these lines. At the same time, at angles 0° and 180° the electrons perform closed cyclotron loops. This localization mechanism leads to an accumulation of electrons on the sides of the cylinder, where the snaking states are formed, and to the depletion of the regions hosting the cyclotron orbits [59].

In a thin prismatic shell the geometric and magnetic localization of the electrons coexist. Therefore, the distribution of electrons is expected to depend on the orientation of the magnetic field relatively to the prism edges or facets, as in the examples shown in Fig. 3.11. Here a carrier concentration of 1.3×10^{11} cm^{-3} is considered, as reported in the recent literature [13]. In each case the color scale represents the difference between the carrier concentration at $B = 2$ T and at $B = 0$ for the three geometries. With the present parameters these differences are somewhere up to 10%. Furthermore, for each geometry, the local changes of the density when the angle of the magnetic field is varied, are up to 1% only. Still, as we shall see, this variation should be sufficient to have implications on the transport data.

Next, in Fig. 3.12 the current distributions in the equilibrium states, i.e. in the absence of a biased chemical potential ($\mu_+ = \mu_-$) are shown. In the absence of the

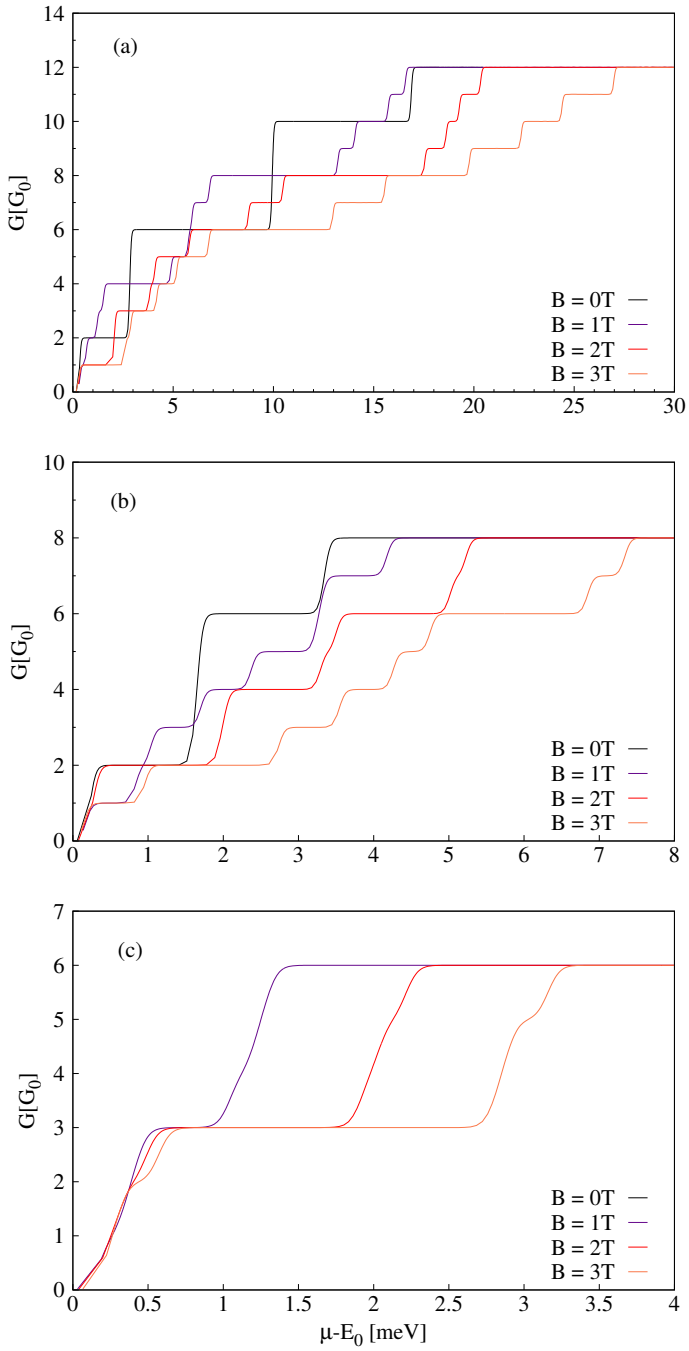

Figure 3.10: Conductance steps for different magnetic field values for the $2N$ corner states of the three prismatic shapes: (a) hexagonal, $N = 6$, (b) square, $N = 4$, (c) and triangular, $N = 3$. As the magnetic field increases, both orbital and spin plateaus develop according to the single particle states evolution in Fig. 3.9.

magnetic field the current distribution is zero everywhere in the shell, i.e. the positive currents and negative currents compensate in each point. In the presence of the magnetic field, as expected, the Lorentz force may create local currents, as shown in the figure, which no longer compensate locally, but indeed the integrated current is zero. The local currents are in fact loops along the z axis of the nanowire, closing up at infinity. Still, it is interesting to observe the compensation of these loops. In the cases where the magnetic field points along the direction of one of the symmetry axes of the cross section the loops are compensated, with the same current flowing

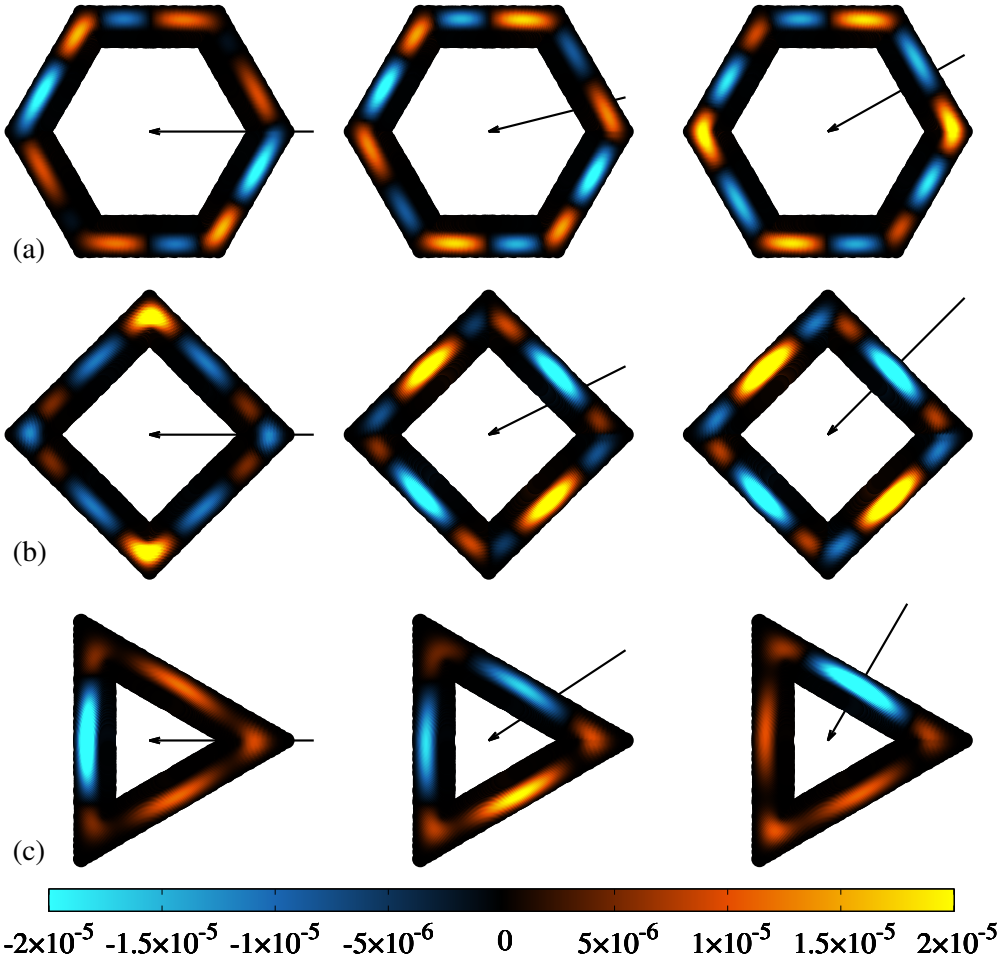

Figure 3.11: The color scale shows the change of the electron density, in units of nm^{-3}, to the orientation of the magnetic field, of magnitude $B = 2$ T, indicated by the arrows, relatively to the three polygonal shells: (a) hexagonal, (b) square, (c) triangular. The magnetic field points to the corners in the left column, it is perpendicular to the sides in the right column, and half way in between these two orientations in the middle column. In each case the electron density for $B = 0$ is subtracted. The average electron density is fixed to 1.3×10^{-4} $\mathrm{n}m^{-3}$. The geometry parameters are $R_{ext} = 50$ nm and $t = 10$ nm.

in both directions, and the channels are paired with the ones on the opposite side of the geometric symmetry axis relative to the magnetic field direction. The pairing can happen within the same corner or side or on opposite ones. In the cases where the magnetic field does not point along one of the symmetry axes the loops are no longer compensated and the current traveling in both directions is not the same. Instead, the compensation occurs when adding the loop on the opposite side of the shell.

3.2.2.2 Energy spectra and conductivity

The energy dispersion with respect to the wave vector k, corresponding to the situations shown in Figs. 3.11 and 3.12, can be seen in Fig. 3.13. The dashed horizontal

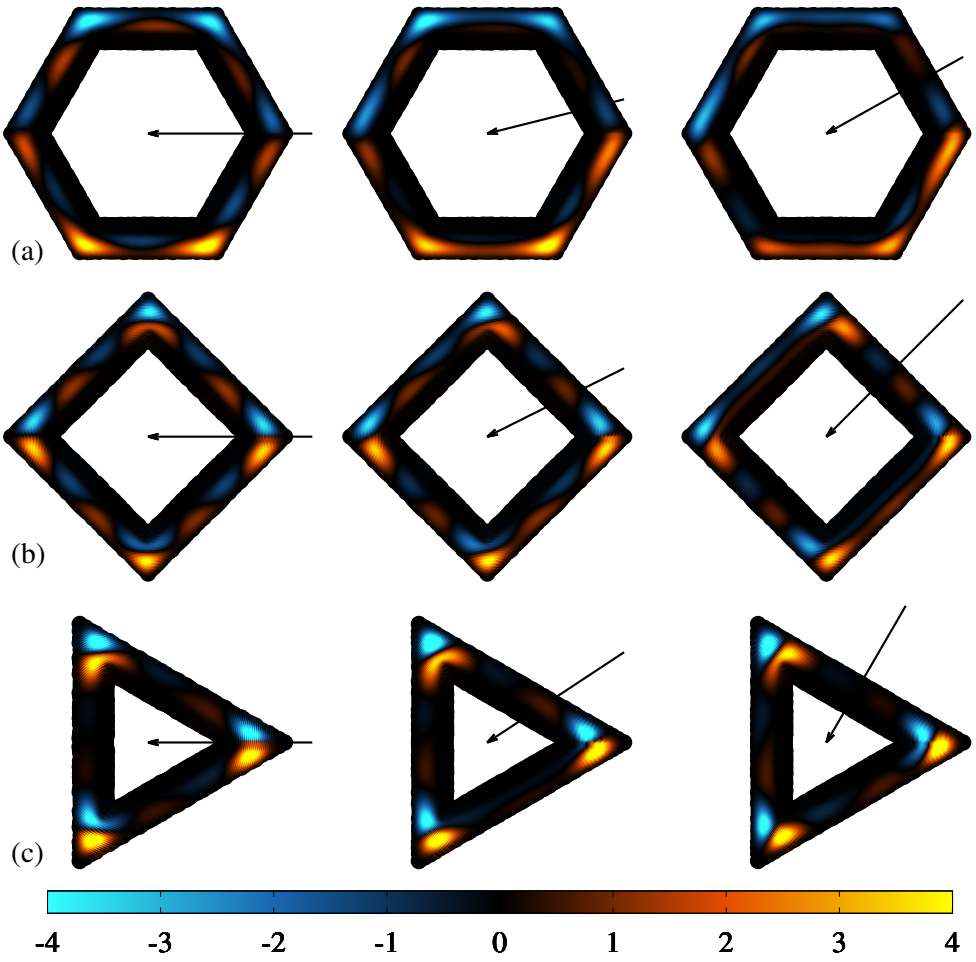

Figure 3.12: The current density in equilibrium (no potential bias) for the same cases as in Fig. 3.11. The color scale is in units of nA/nm^2

.

lines indicate the chemical potential corresponding to the selected carrier concentration. In all cases, in the absence of the magnetic field the position of the chemical potential is somewhere at the level of the side states. The presence of the magnetic field mixes the corner and the side states and leads to quite complex changes in the spectra and in the charge or current distributions. Moreover, as it can be seen, the energy dispersions are also sensitive to the orientation of the field relatively to the prismatic shell.

Note that in the triangular case, the spectra may not be symmetric (even) functions of the wave vector k if the magnetic field is not aligned with a symmetry axis of the shell, like in the second example of Fig. 3.13 (c), corresponding to the second example of Fig. 3.11 (c). In this case the magnetic field is parallel to the side of the triangle. The sign reversal of the magnetic field leads to the sign reversal of the wave vector, i.e., to the same energy spectrum. The reason for the asymmetric spectra is that the triangular geometry is somehow special, compared to the hexagonal or square, because of the absence of an inversion center. Still, in principle, in all cases, the symmetric polygonal shells are only idealized models, since realistic core-shell nanowires are never

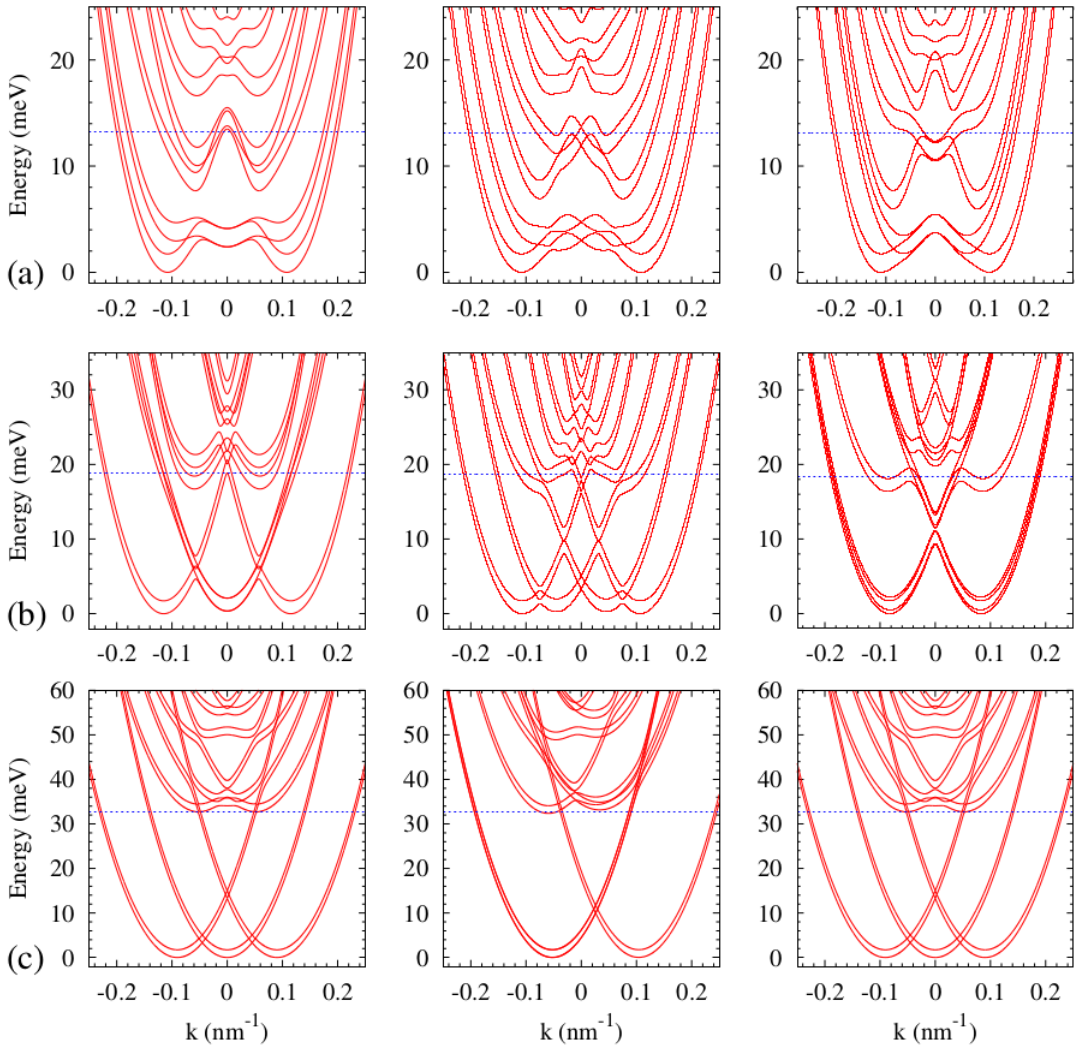

Figure 3.13: Energy spectra obtained by varying the angle of the perpendicular magnetic field, as in Fig. 3.11: (a) hexagon, (b) square, (c) triangle. In each case the energy of the ground state is considered zero. The temperature is 1 K.

perfectly symmetric, first because of imperfections in the fabrication process, and second due to the attached contacts or gates.

According to these results it can be predicted that due to the internal geometry of the nanowire the conductance should depend on the orientation of the magnetic field in a manner that indicates the polygonal symmetry of the shell cross section. This is demonstrated in Fig. 3.14 where the results obtained with the Kubo formula (2.24) are shown. In these calculations infinitely long nanowires are assumed and a disorder broadening of the energy spectra is included, described by the parameter $\Gamma = 1$ meV in Eq. (2.22), i.e., far from the ballistic regime. In addition temperatures up to 50 K are considered, to emphasize that the conductance anisotropy should be also robust to thermal perturbations.

For each geometry the zero angle is considered when the field is oriented towards a prism edge, as shown in the first column of Fig. 3.11. The angular period of the conductivity, when the magnetic field rotates, is obtained when the magnetic field points to the next corner for the hexagon and square, i.e., 60° and 90°, respectively,

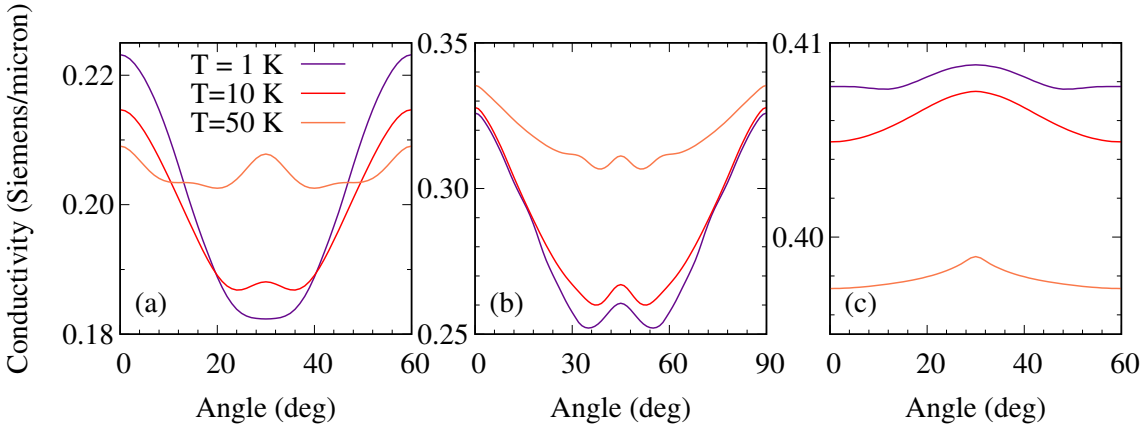

Figure 3.14: Conductivity as a function of the angle of the magnetic field, for temperatures 1 K, 10 K, and 50 K, within one full period for each geometry (a) hexagonal, (b) square, and (c) triangular shells. As before, the magnetic field is $B = 2$ T and the carrier concentration 1.3×10^{-4} nm^{-3}. The results are obtained with Kubo formula including a disorder broadening of 1 meV.

whereas for the triangle it corresponds to a half of it, i.e., 60°. Obviously, all figures can be continued by periodicity, up to a complete rotation of the magnetic field.

The conductivity described by the Kubo formula is, in this case, an example of band conductivity, i.e., it is directly related to the velocity of carriers along the transport direction, like in the ballistic case, and decreases when the disorder parameter Γ increases [148]. The dependence on the temperature is more complicated. In this calculations the dependence on the temperature of the collisional broadening parameter Γ is completely ignored, which is a separate problem. In this model the main effect of increasing the temperature is the population/depopulation of the states above/below the chemical potential, respectively, and to a lesser extent the variation of the chemical potential itself. Because the energy curves are nonlinear functions of the wave vector, the velocity distribution of the carriers changes in a nonuniform manner, such that the conductivity may either increase or decrease with increasing the temperature. The relative variation of the conductivity with the angle is also not simple, meaning that it can increase or decrease, depending on what is going on around the chemical potential when the magnetic field is changing orientation. In these examples we can see that the variation is the weakest for the triangular case, which is because the corner localization is stronger and their mixing with the side states is relatively weak.

The conductance anisotropy in hexagonal core-shell nanowires was already predicted for the case with electrons localized in the core [42], but only in the ballistic regime, much higher magnetic fields, and much less pronounced. In this case the results obtained in the ballistic regime are qualitatively similar to those shown in Fig. 3.14, except at low temperatures, when the conductance depends critically on the number of intersections of the Fermi energy with the energy bands, which may vary discontinuously. But, since it is difficult to obtain the ballistic regime in realistic experimental samples, these results show that the anisotropy of the shell could be easier resolved, in well attainable experimental conditions, and possibly not only at low temperatures.

3.2.2.3 Nonlinear I-V characteristics

Another indication of the internal geometry of the prismatic shell can be the $I-V$ characteristic, as shown in Fig. 3.15. The $I-V$ characteristics are obtained following the same method used for the conductance, i.e., an imbalance is created between states with positive and negative velocity but in this case the potential bias is increased far from the linear range, starting with a chemical potential close to the lowest band bottom.

We can first notice the bias threshold where the linear regime breaks. That is the lowest for the hexagonal geometry, below 5 meV, whereas for the square and triangular cases it increases to 15 meV and 35 meV, respectively. The change of the slope of the curves, more clearly seen for square and triangular cases, indicate the transition from corner states to side states, as more channels are crossed, and could offer a possibility to observe experimentally the existence of the gap separating these groups of states. In some cases the magnetic field yields a reduction in energy and a shift in k-space of two mixed-spin bands, leading to an avoided crossing at $k = 0$. In these cases an inflection point is observed, more clearly for the hexagonal and square cases, as a consequence of the reduction in the number of levels crossed by the potential bias.

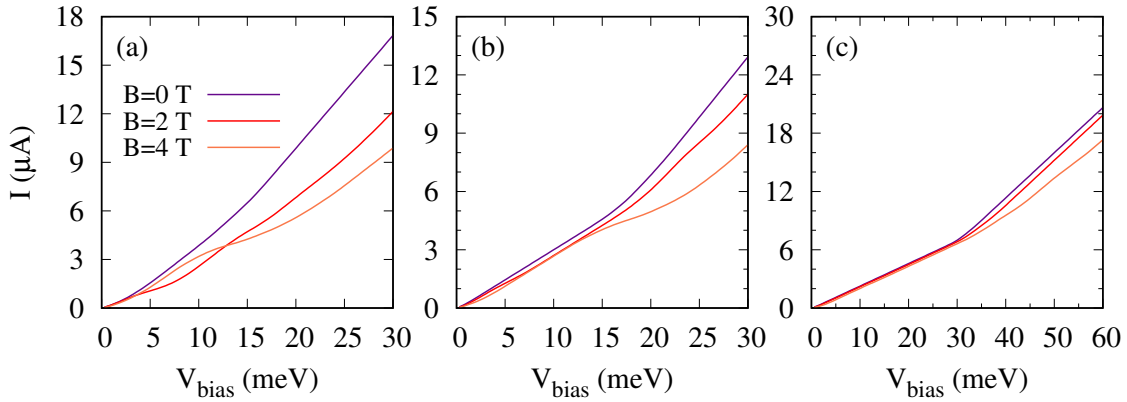

Figure 3.15: $I-V$ characteristic for different values of a magnetic field perpendicular to an edge for the hexagonal (a), square (b), and triangular (c) nanowires. A disorder broadening of the energy spectra $\Gamma = 1$ meV is included.

In the results shown in Fig. 3.15 a temperature of 25 K was used in order to increase the population of the states above the chemical potential. The I-V curves were obtained assuming an infinite wire without impurities. To a first approximation their averaged effect can be incorporated in Eq. 2.21 by the substitution

$$\mathcal{F}\left(\frac{E_{mks}-\mu}{k_BT}\right) \rightarrow \int A_{mks}(E)\mathcal{F}\left(\frac{E-\mu_{\pm}}{k_BT}\right) dE \tag{3.1}$$

In this way results similar to those shown in Fig. 12 can be obtained, with a lower temperature, T = 1 K, but with a disorder energy $\Gamma = 1$ meV.

3.3 Density response under a time-harmonic perturbation

In this section, results corresponding to the density response of finite nanowires are presented. The work presented in this section is still in progress.

As previously stated, in order to study the density response to a time-harmonic perturbation it is necessary to consider nanowires with finite length. The dimensions of the nanowires in the examples that follow are $R_{ext} = 50$ nm, $t = 9$ nm and $L_z = 200$ nm. The number of states in this case is $N_w = 2N_tN_l$, where the factor 2 takes into account the two-fold spin degeneracy and N_t and N_l are the number of states corresponding to the transversal and longitudinal Hamiltonians. Here, $N_t = 3, 4, 6$ for the triangular, square and hexagonal nanowires, respectively, and $N_l = 200$ in all cases. The states, arranged according to increasing energy, are shown in Fig. 3.16. The intervals separating the group of corner from the group of side states are $\Delta_h = 2.2$ meV, $\Delta_s = 20.4$ meV and $\Delta_t = 57.1$ meV.

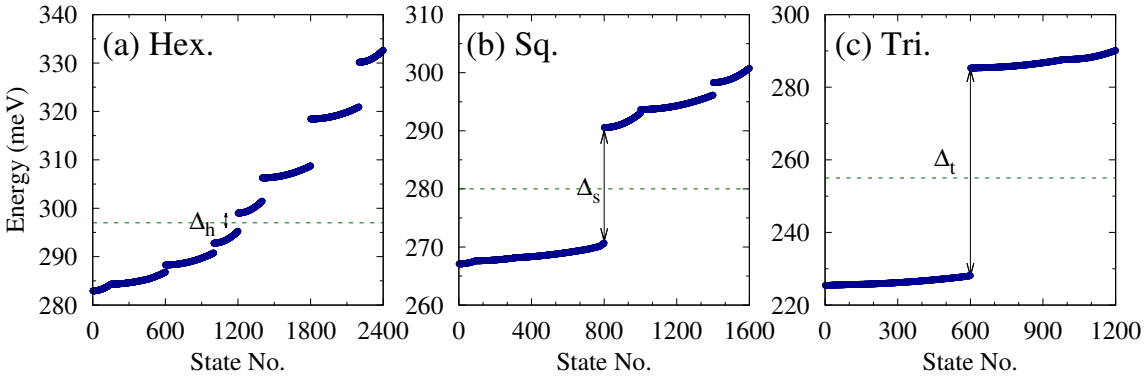

Figure 3.16: First two sets of energy levels (groups of corner and side states) of the nanowires for the three different geometries. The green dashed-lines represent the chemical potentials.

The nanowires are exposed to a longitudinal voltage bias of $V_0 = 0.2$ meV, which breaks the orbital degeneracy of the states, and are perturbed by a time-harmonic tilted voltage $\delta V_{ext}(\boldsymbol{r}) = 0.1x + 0.1y + z$ meV. The density response is studied by sweeping the frequency of the perturbation over a range that includes the energy gaps separating side from corner states.

In accordance to Eq. 2.14, for a given chemical potential, and as long as $\mathcal{F}'_m - \mathcal{F}_m \neq 0$, the density response $\delta\rho$ has a series of resonance peaks corresponding to the frequencies for which the difference $[(\hbar\omega + E_{m'}) - E_m] = 0$. The adiabatic parameter, $\eta^+ = 0.2$ meV, is included so that the singularities are avoided.

In Fig. 3.17, the dependence of the density response on the frequency is shown. The response is calculated in the middle of the nanowire ($z = L/2$) in two points of the cross section, which lie in the center of the corners (blue curves) and in the center of the sides (red curves) for which the response is maximal. As it can be seen, in each case there is a series of resonance peaks which arise due to the aforementioned conditions. However, it is important to note that this peaks do not exactly occur for the frequencies that match the gaps, but rather for the ones that match the "mode" energy separation between occupied and unoccupied energy levels; as the sum $\sum_{mm'}$, in Eq. 2.17, runs over all possible pairs of states.

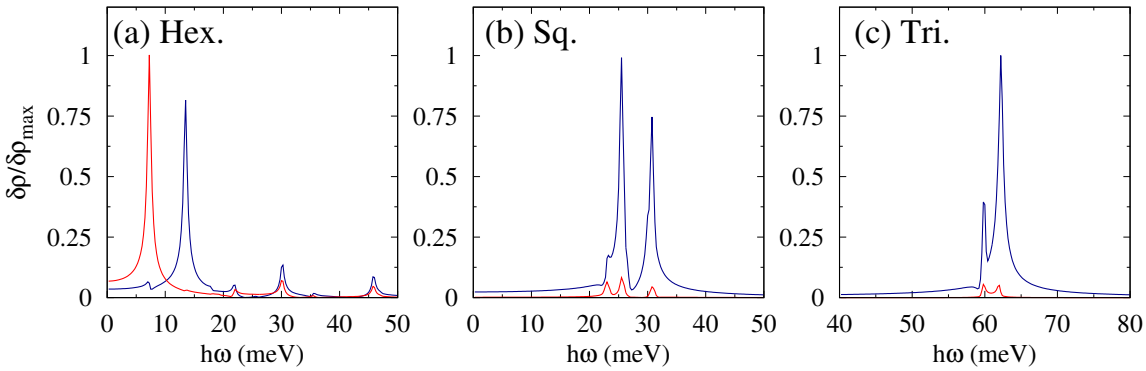

Figure 3.17: Amplitude of the density response in arbitrary units as a function of the perturbation's wavelength calculated in two points; one lying on the center of the corner area (blue curves) and another one lying on the center of the side area (red curves).

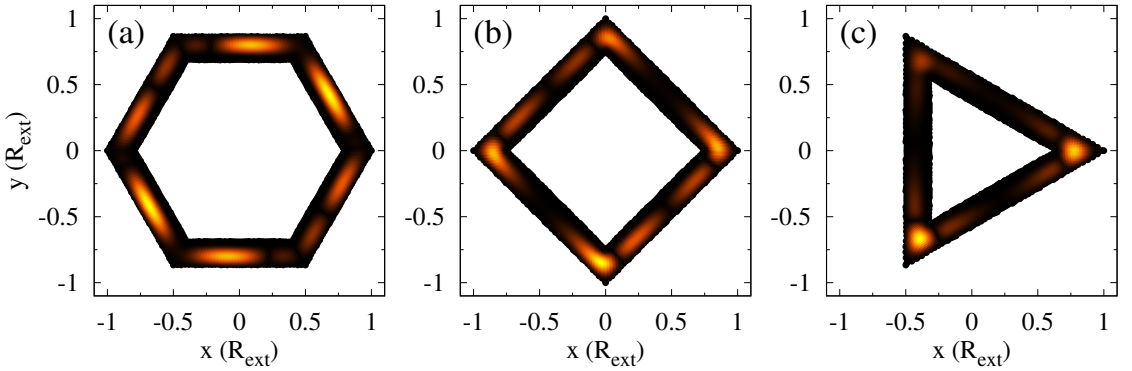

Figure 3.18: Amplitude of the density response in each geometry for a perturbation's frequency corresponding to the highest resonance peak calculated in each case.

In the examples shown here, the chemical potential lies in the gap separating corner from side states. Thus, the main resonance peaks, for the triangular and square nanowires, happen for the frequencies that match the average energy separation of all the possible pairs of corner and side states, and the secondary peaks arise as consequence of the gaps within the corner or the side states domain, together with the fact that the energy levels are not homogeneously distributed. As it is also observed, the peaks corresponding to the side area are much smaller in these two cases, as the occupied states correspond to electrons localized in the corner areas. For the hexagonal nanowire, for which the localization is weakest, however, the situation is more complex, since the localization of different subsets of side states is also different, and because the localized corner states overlap along the sides, making the resonant frequencies to be highly dependent on the point where it is calculated.

In Fig. 3.18 we show the amplitude of the density response, corresponding to the frequency for which the highest resonance peak is achieved. As can be observed, and in accordance to the results shown in Fig. 3.17, the amplitude of the density response on the center of the sides is almost negligible in comparison to the response on the corners for the square and the triangular nanowires, whereas it dominates in the case of the hexagonal nanowire.

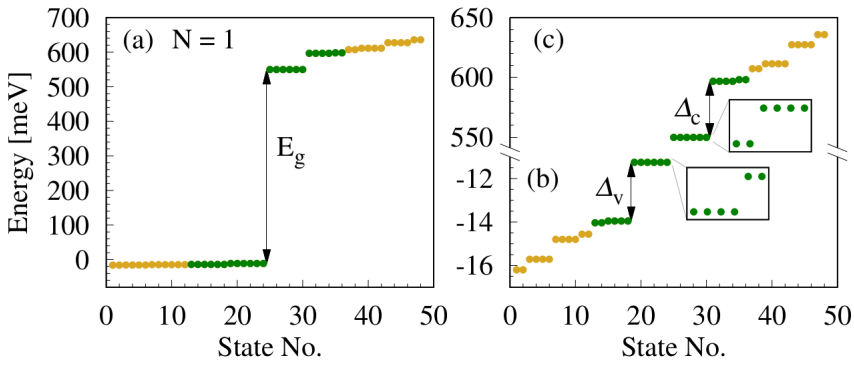

Figure 3.19: (a) Single-particle energy levels close to the band edges for a triangular shell. The separation between the lowest conduction and highest valence levels (E_g = 561 meV) is considerably increased with respect to the bulk value (E_b = 354 meV) due to the confinement. (b) and (c) zoomed valence and conduction levels. The arrows indicate the splittings between corner and side spin-orbital states in the two bands (Δ_v = 2.7 meV and Δ_c = 47 meV). Insets to both figures show the degeneracy of corner spin-orbital states in each band.

3.4 Excitons

In this section, results corresponding to the study of the properties of excitons confined in polygonal shells are presented. The results presented in this section are an excerpt from Ref. [149].

3.4.1 Single-particle states

The results of this part were achieved with the discretization method described in Section 2.1. For the studied triangular cross section, t = 8 nm and R_{ext} = 50 nm. In the case of square and hexagonal samples the results were obtained for the same parameters and for reduced values of t or t and R_{ext}. The numerical calculations were performed for InAs material parameters which are $m_c^* = 0.023m_e$, $m_v^* = -0.4m_e$, $g_c^* = g_v^* = -15$, $\epsilon = 15$, and $E_b = 354$ meV. The values of the g factors are used here as test values. However, the present results are not significantly sensitive to the g factor of electrons or holes, since only a weak magnetic field is considered, in order to lift the spin degeneracy.

To construct the multi-electron interacting Hamiltonian (Eq. 2.31) the single-particle spectrum is truncated to $4N$ valence and $4N$ conduction states, where N is the number of corners, and the eigenvalue problem is solved by diagonalizing the Hamiltonian in the base built of those $8N$ states. In this way, the corner and side states from both bands are included in the model in order to describe corner and side localization of electrons or vacancies.

Both the lowest group of conduction band states and the highest valence band states consist of corner-localized states. The energy gaps between corner and side states, Δ_v and Δ_c, for valence and conduction bands, respectively, are the largest gaps within each band and in both cases exceed the energy dispersion of corner states by few orders of magnitude. Due to the large effective mass, the splittings between adjacent valence levels are much smaller than within the conduction band, and thus Δ_v is over one order of magnitude smaller than Δ_c, Figs. 3.19(b) and 3.19(c).

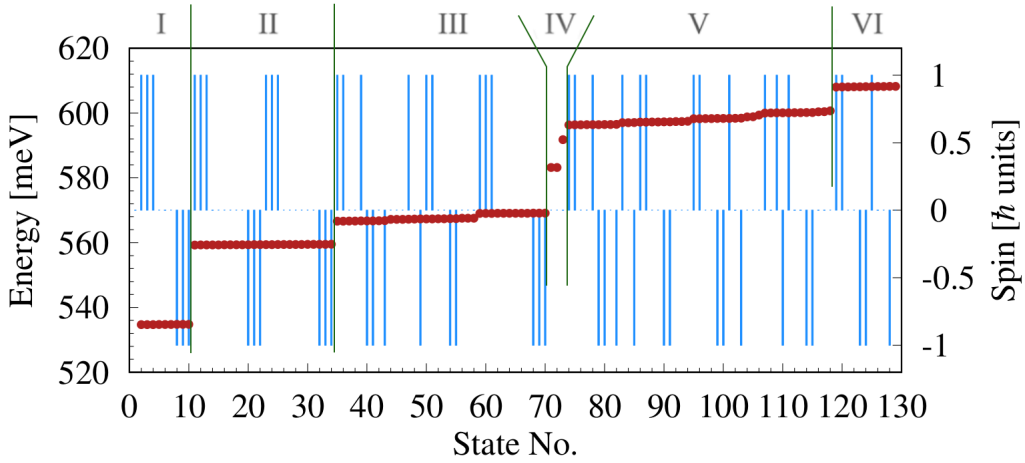

Figure 3.20: Excitonic energy levels and the corresponding zth component of spin (light blue bars).

3.4.2 Excitons in triangular shells

The ground state and the zero energy level correspond to the fully occupied valence band. An exciton is thus created when one of the electrons is excited to the conduction band leaving a vacancy in the valence band. The top of the valence band is described by restricting the system to 12 electrons, i.e., only electrons localized in the corners or the sides may be shifted to the conduction band. The ground state consists then of the 12 highest valence states, i.e., the 6 corner and 6 side states. This restriction is necessary for taking into account the Coulomb interaction in a reasonable configuration-interaction space.

The energy levels obtained with the multi-electron configuration-interaction method are shown in Fig. 3.20. The probability distributions for symmetric polygons always obey the geometric symmetry. Therefore, in order to identify the number of electrons occupying each particular corner or side area, the system symmetry is broken with an electric field of 0.22 mV/R_{ext} and a magnetic field of $B = 50$ mT, both parallel to one of the sides. The external fields rearrange the electron localization and only slightly affects the energy levels, removing the orbital and spin degeneracies [150].

The lowest group of 9 states [zone I in Fig. 3.20, $2 \leq \alpha \leq 10$] is associated with almost-symmetric probability distributions, forming single peaks on corner and side areas [Fig. 3.21(a)]. This, together with a very small energy dispersion, suggests that the conduction electron and the vacancy are localized on the same corner.

The second level consists of 24 states [zone II, $11 \leq \alpha \leq 34$] within an interval of 0.16 meV. The corresponding probability distributions form 3 equal maxima on the sides and 3 peaks of different height in the corners. This indicates that there are 3 electrons accumulated in the corner area where the highest peak appears, 2 particles in the second one and only 1 electron on the third corner [Fig. 3.22(b)]. Since at most 2 valence electrons may stay so close to each other, the third particle in the corner must be the electron excited to the conduction band, while the single valence electron is paired with the vacancy.

The energy dispersion of the third group [zone III, $35 \leq \alpha \leq 70$] increases because of side-localized vacancies. The 3 in-gap states [$\alpha = 71$, 72, and 73, zone IV] consist of a conduction electron and the vacancy in the same corner area and are associated with

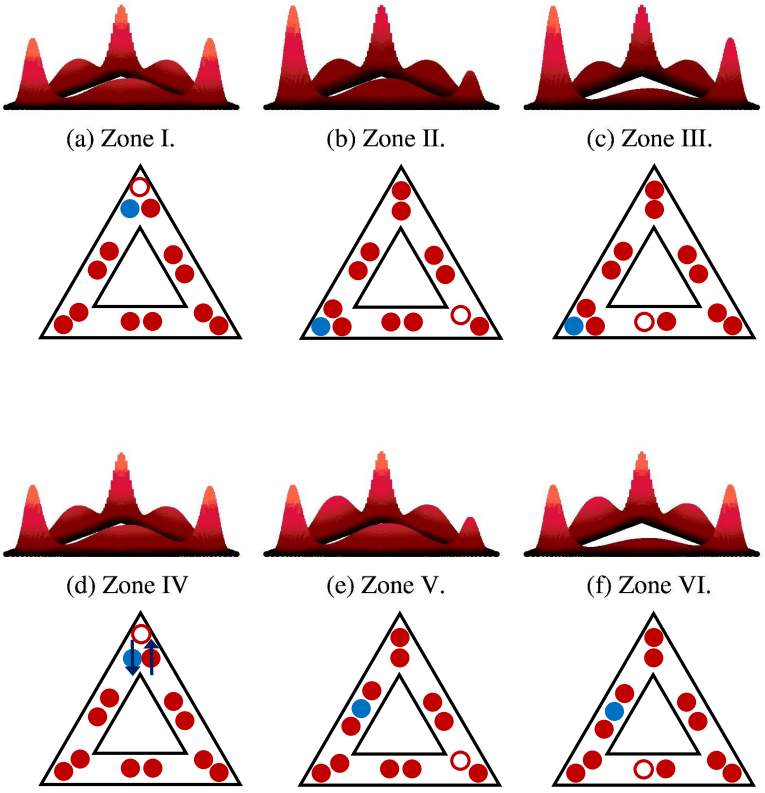

Figure 3.21: Probability distributions associated with the representative excitonic states and the corresponding (pictorial) electron arrangements for each spectral zone indicated in Fig. 3.20. The filled red circles stand for the valence electrons, the red empty circle represents the vacancy in the valence band and the blue circle indicates the position of the conduction electron. Arrows in (d) stand for the spin singlet configuration.

symmetric probability distributions [Fig. 3.21(d)]. Although 12 electrons are taken into consideration, there are only 3 possible values of the zth component of the exciton spin: $-\hbar$, 0, and $\hbar$, which are characteristic for a pair of $\pm\hbar/2$ spin particles. Such system may be in one of the triplet ($|1,1\rangle$, $|1,0\rangle$, $|1,-1\rangle$) configurations or in a singlet ($|0,0\rangle$) state. Due to the system symmetry and equivalent electron distributions, each of the 4 spin configurations is repeated within every group of the same localization type. For example, there are 12 states [$2 \leq \alpha \leq 10$, and $71 \leq \alpha \leq 73$, zones I and IV] associated with the conduction electron and the vacancy both localized on the same corner. As can be seen in Fig. 3.20, two values of the zth spin component ($-\hbar$ and $\hbar$), are repeated 3 times while the third value (0) occurs 6 times within the group, i.e., the whole set of 4 spin configurations is reproduced 3 times. The 9 lower states are in the triplet configurations and form a quasi-degenerate level, while the 3 remaining states are moved to much higher energies. The spin singlet configuration allows the particles to approach so close to each other that the contribution due to the Coulomb interaction of symmetrically distributed electrons exceeds even the one corresponding to 3 electrons accumulated in one corner area [zones II and III, $11 \leq \alpha \leq 70$]. Two of these excitonic in-gap states are almost degenerate (Fig. 3.20), and would be degenerate in the absence of external fields, while the energy of the third state is substantially higher.

Higher states correspond to excitons consisting of conduction electrons occupying sides and vacancies localized in corners, [zone V, Fig. 3.21(e)], or on side areas [zone VI,

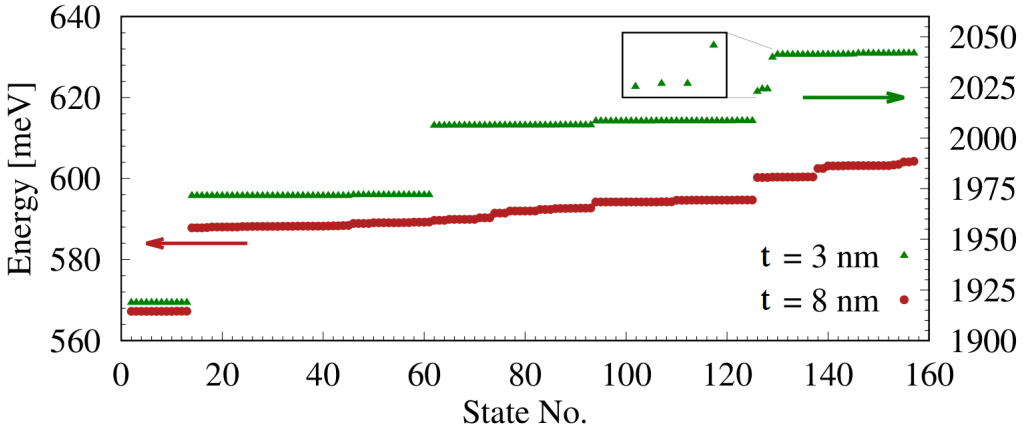

Figure 3.22: Excitonic energy levels for two symmetric square shells of different side thickness (t). The shells are restricted externally by the same external radius ($R_{\text{ext}} =$ 50 nm). The green and red arrows indicate the relevant axes.

Fig. 3.21(f)]. The gap that originates from Δ_c, between zones III and V, is affected by the Coulomb interaction. If the 3 states in the gap are not taken into consideration, the states approaching the gap from lower and higher energies differ by the spatial separation of electrons. In particular, the lower states correspond to arrangements that include 3 electrons accumulated in a small corner area [Fig. 3.21)(c)], while the higher states correspond to conduction electrons sharing side areas together with 2 other (valence) electrons [Fig. 3.21(e)], i.e., the set of 3 electrons is distributed on a much larger area than in the former case. This results in a much smaller contribution due to Coulomb repulsion to these states than to the states below the gap, and thus considerable reduction of the splitting between the two groups [zones III and V] with respect to Δ_c.

3.4.3 Excitons in square and hexagonal shells

For a square shell, the energy gap separating corner from side states in the conduction band is still considerably large and for $t = 8$ nm equals 20.6 meV. However, the splitting between excitonic states containing the conduction electron in the corner or in the side area is considerably reduced due to the Coulomb repulsion and it is not broken by high energy corner states (Figs. 3.22(red circles)). Four corners allow for 16 states corresponding to the conduction electron and the vacancy both localized on the same corner. As seen in Fig. 3.20, only 12 states ($2 \leq \alpha \leq 13$) of this type are separated from the spectrum. Similar to the triangular shell, the 4 remaining states acquired much more energy but, due to the relatively small energy splitting between the lowest states and the states corresponding to conduction electrons occupying side areas, those 4 purely corner excitonic states mix with the latter states.

To considerably separate the two types of excitonic states and to keep the high-energy corner states within the gap, t was reduced to 3 nm (green triangles in Fig. 3.22). The 4 in-gap states reproduce the degeneracy of single-particle corner states with respect to the spin [121], i.e., the lowest and highest states ($\alpha = 126$ and 129) are non-degenerate, while the middle states are twofold degenerate. In this case, the largest energy splitting results from the large increase of the Coulomb interaction due

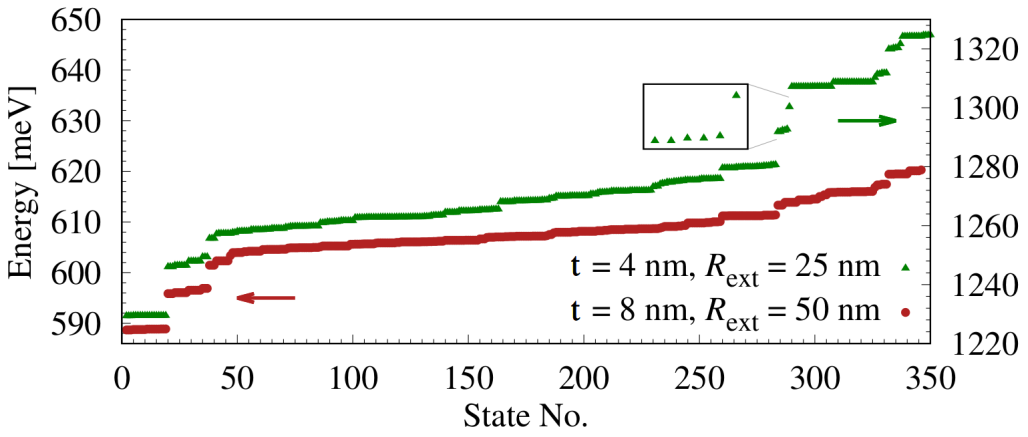

Figure 3.23: Excitonic energy levels for two symmetric hexagonal shells. The shells differ in both t and R_{ext}. The green and red arrows indicate the relevant axes.

to the increased number of electrons in particular corners. As seen in Fig. 3.22, this splitting is much larger for the thinner shell as the corner localized electrons are accumulated on much smaller areas, increasing Coulomb interaction. Since 4 corners allow for more combinations of electron distribution, the energy structure is richer than for the triangular shell. The purely corner states, which are associated with non-symmetric electron arrangements, form two closeby levels corresponding to the conduction electron and the vacancy occupying neighboring ($14 \leq \alpha \leq 45$) and alternating ($46 \leq \alpha \leq 61$) corners. The small difference between these two levels shows that Coulomb interaction between electrons localized in different corners is negligibly small. The following 64 states correspond to vacancies localized on sides and the conduction electron in one of the corners, i.e., there are 3 pairs of electrons in 3 corners while the fourth corner is occupied by 3 particles.

For the hexagonal shells, the lowest 18 states are also separated from the spectrum (Fig. 3.23), with a slightly larger dispersion than in the previous cases. The corner localization softens with increasing the number of corners and, for $t = 8$ nm, the corner peaks penetrate into the sides and overlap. This increases the corner areas and allows for a much larger spatial separation between corner-localized electrons, decreasing the Coulomb interaction of the few particles accumulated in one corner. However, the interaction between electrons occupying neighboring corner and side areas increases considerably and, to a lesser extent, the interaction of electrons in consecutive corners. The overlap of single-particle states strongly depends on the energies and thus, also the contributions due to the Coulomb interaction may differ even within the group of states associated with similar particle arrangements. As a result, some of the states corresponding to unequal electron distributions ($20 \leq \alpha \leq 47$) are pulled towards lower energies. The effect is amplified by the reduction of the distances between the vertices and the possibility of different distributions of the conduction electron and the vacancy within the cross section. If the external radius and side thickness are not changed, then the energy gap separating corner from side conduction states of a hexagonal shell is much smaller than the one of square samples and for the 8 nm thick shell it hardly allows to separate the two types of excitonic states. Here the dominant splittings are purely of Coulomb origin (red circles in Fig. 3.23).

To move the 6 high-energy corner states below the states corresponding to conduction electrons occupying side areas, it was necessary to decrease both the t and R_{ext}

to 4 and 50 nm, respectively. As shown in Fig. 3.23, such a shell provides sufficiently large gap which can host the whole set of 6 states in the spin singlet configuration for which the conduction electron and the vacancy are localized in the same corner area.

3.5 Radiated electromagnetic fields

In this section, results corresponding to the study of the electromagnetic field radiated by the polygonal core-shell nanowires driven by an alternate current are presented. The results are divided into two parts, the first one corresponding to the case in which no external magnetic field is applied to the nanowires and a second one where the effects of the external magnetic field are studied.

3.5.1 Features of the radiation in the absence of external fields

In all the examples shown in this article the external radius of the shell and the thickness of the facets are $R_{\text{ext}} = 30$ and $t = 6$ nm, respectively, and the length is considered infinite in the model. InAs bulk parameters are considered for the nanowire: $m_{eff} = 0.023m_e$ and $g_{eff} = -14.9$. A voltage bias corresponding to $V = 2.5$ meV and a test frequency of 1 MHz are considered. For these dimensions, in Figs. 3.24(a-c) the energy spectra of nanowires with hexagonal, square, and triangular (with hexagonal core) cross sections are shown, assuming free electron scattering and no external fields. The energy interval between corner and side states are $\Delta_h = 21.2$ meV for the hexagon, $\Delta_s = 34.4$ meV for the square and $\Delta_t = 171.1$ meV for the triangle.

When a harmonic voltage is applied to the nanowires, the total current is zero at those instants of times when $\mu_\pm = \mu$, i.e., when $\sin(\omega t) = 0$. However, at these instants the amplitude of the radiated field is maximal, as it depends on the time derivative of the current density through the vector potential. Contrarily, when $\sin(\omega t) = 1$ the voltage amplitude applied is maximal and $\mu_\pm = \mu + V$, at these instants the current reaches its maximum but its time derivative goes to zero, and so does the radiated electromagnetic field. It is important to note that, when $\mu_\pm \neq \mu$ or $\sin(\omega t) \neq 0$, depending on the amplitude of the harmonic voltage applied, electrons may cross different energy levels, which translates in changes of localization, and hence of current distribution and radiated field, along one period of time.

For simplicity, in the examples of this article only the time derivative of the current density in the case of $\mu_\pm = \mu$ is shown, when the radiated field intensity is maximal. In the absence of external fields, the current density distribution follows the localization of the charge distribution, i.e., the voltage bias only creates an imbalance between carriers moving with opposite directions along the length of the nanowire restricted to the localization stemming from the geometric boundaries. In Figs. 3.24(d-f), the time derivative of the current density ($d\boldsymbol{J}/dt$) in the nanowires is plotted, in the absence of external fields and corresponding to a carrier density of $n = 10^{-4}$ nm^{-3}, which lies in the corner-localized group of states. The values of the total current driven along the nanowire for this carrier density ranges from a few nA to a few μA for voltage bias amplitudes of 1-10 meV [142].

The power density of the resulting radiated electromagnetic field is shown in Figs. 3.24(g-i). In order to resolve the structure of the radiated field, the difference of the power density relative to its minimum value in each case is shown, which are

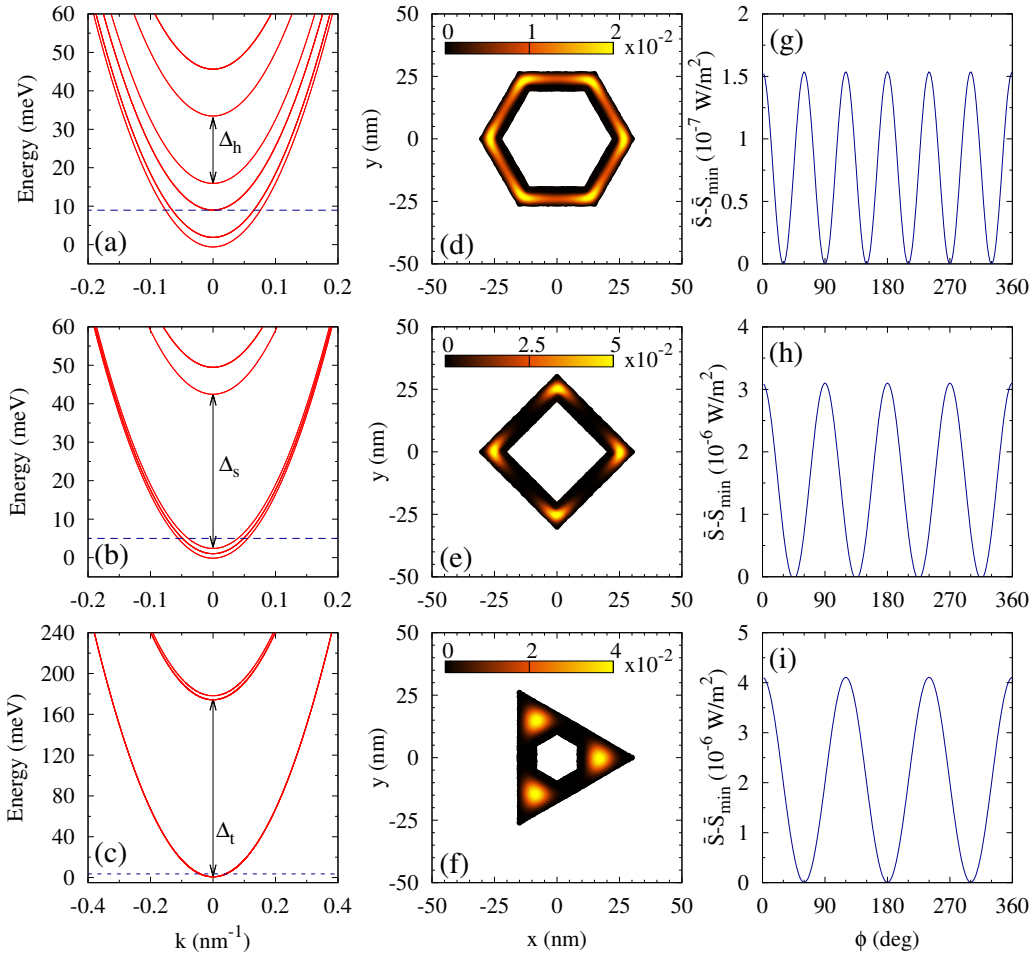

Figure 3.24: (a-c): energy spectra obtained for the three polygonal shapes with $R_{\text{ext}} = 30$ and $t = 6$ nm. The blue-dashed lines mark the chemical potential μ in equilibrium for a carrier density of $n = 10^{-4}$ nm^{-3}, the arrows indicate the energy gap between the groups of corner and side states. (d-f): time derivative of the current density $(d\boldsymbol{J}/dt)$ inside the nanowire when its amplitude is maximal, i.e, at an instant in time when $\mu_{\pm} = \mu$, the color scale units are A/(s · nm^2). (g-i): relative difference of the time-averaged Poynting vector (radiated power density) as a function of the angle at a distance of $2R_{ext}$ from the center of the nanowire. The initial 0° is taken to be at the rightmost corner of the shell in the figures and increases counter-clockwise.

$\overline{S}_{min} = 3.01,\ 3.06,\ 1.76 \cdot 10^{-4}$ W/m^2 for hexagonal, square and triangular nanowires, respectively. As expected from the current density distribution, the resulting field captures the internal geometry of the nanowires and has a number of peaks equal to the number of corners, as the electrons localized in each one form quasi-independent current channels which can be considered as individual nanowires.

In Fig. 3.25 the decay with the distance of the difference between the maximum and the minimum values of the power density curves shown in Fig. 3.24(g-i) is presented, starting with $d = 2R_{\text{ext}}$ up to $d = 10R_{\text{ext}}$. The anisotropy decays faster for the hexagonal nanowire, which is closer to a cylinder. The difference in the square and triangular nanowires have similar starting values, but it decays faster for the square. The difference at $d = 10R_{\text{ext}}$ is around 10^5, 10^3 and 10^2 times smaller for hexagonal, square and triangular nanowires, respectively.

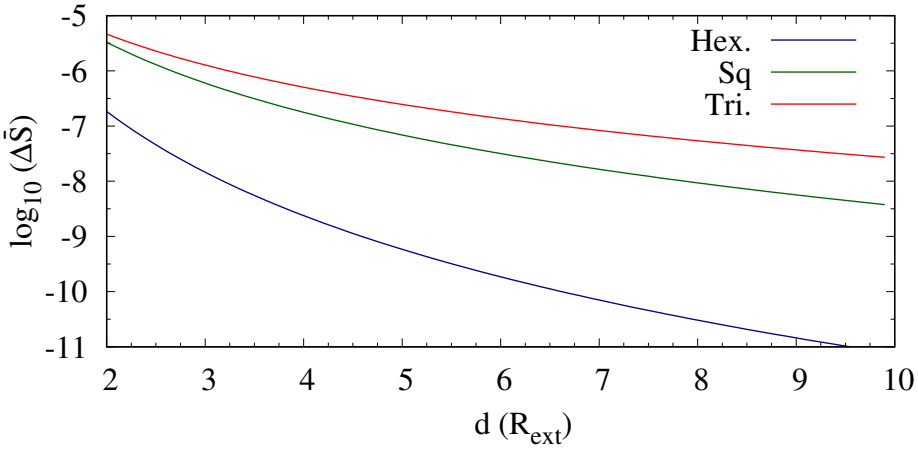

Figure 3.25: Decay of the relative difference, in log-scale, between minimum and maximum values of the radiated power density as a function of the distance from the center of the nanowire.

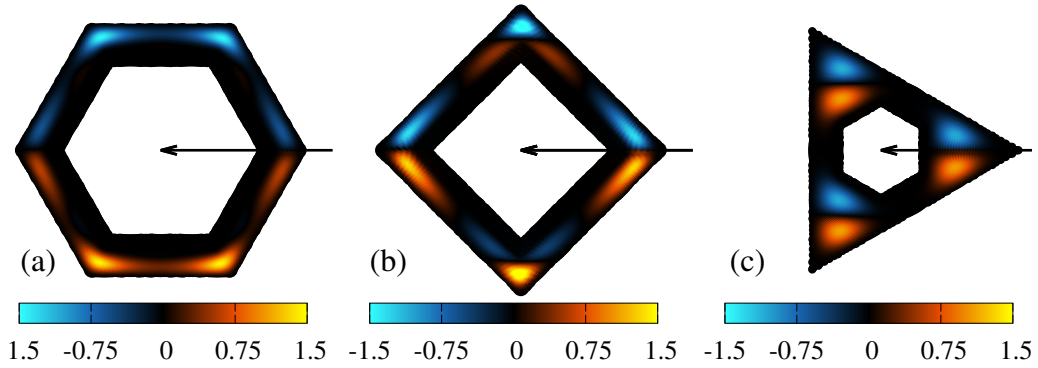

Figure 3.26: Current distribution in equilibrium inside the polygonal shells for $n = 10^{-5}$ nm^{-3} when a magnetic field of $B = 1$ T is applied perpendicular to one of the edges for the hexagonal (a), square (b) and triangular (c) shells. The units of the color scale are nA/nm^{-2}.

3.5.2 Features of the radiation when an external magnetic field is applied

Applying a transverse external magnetic field creates a second localization mechanism which, together with the localization imposed by the polygonal shell, leads to a complex electronic distribution. If the magnetic field is strong enough, it can mix the two groups of corner and side states, leading to complex changes in the energy spectra and in the current distributions, as it has been described in Section 3.2.2.1. The dispersion with respect to the wave vector k when a magnetic field is applied perpendicular to one of the edges is shown in Figs. 3.27(a-c). In all cases, the same carrier density ($n = 10^{-4}$ nm^{-3}) is used so that the position of the chemical potential would be at the level of the corner states if there was no magnetic field applied, as shown in Figs. 3.24(a-c).

As pointed out previously in Section 2.4, when no longitudinal voltage is applied on the nanowire, the total current is zero, i.e., the current corresponding to the electrons moving with positive velocity compensates the current of those moving with negative velocity in the z direction and the current distribution is zero everywhere. In this

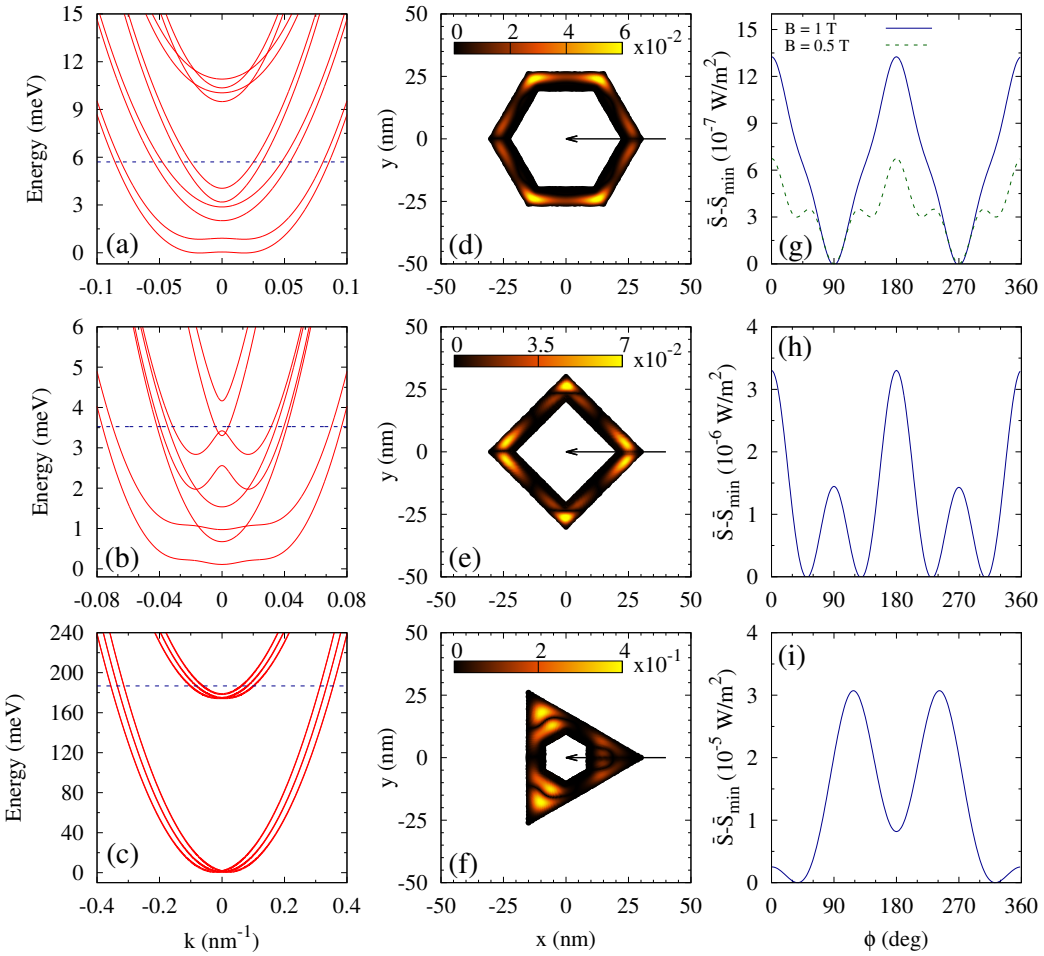

Figure 3.27: As in Fig. 3.24 in the presence of an external magnetic field of $B = 1$ T perpendicular to one of the edges of the nanowire [indicated by the arrows in (d-f)]. The additional dashed green curve in (g) corresponds to the case of $B = 0.5$ T, shown in order to illustrate the evolution of the curve. The chemical potential in (c) corresponds to a carrier density of $n = 10^{-3}$ nm^{-3} for the triangular nanowire. The color scale units are A/(s $\cdot$ nm^2).

case, electrons move in parallel along the prism edges restricted to their corner or side localization. Note however that, as it was also described in Section 3.2.2.1, in the presence of a magnetic field, the Lorentz force creates local currents, in the form of loops along the z axis of the nanowire closing up at infinity, so that, even if the total integrated current is still zero, the currents do not compensate locally. This is shown in Fig. 3.26, where the current density distribution in equilibrium ($\mu_\pm = \mu$) is shown when a magnetic field perpendicular to one of the edges of the prism is applied.

The channels that form each loop are compensated, i.e., the same current flows in both directions and are being accelerated/decelerated at same rate, with each channel paired with the one on the opposite side of the geometric symmetry axis relative to the magnetic field direction. Depending on the localization strength, the pairing can happen within the same corner or side or on opposite ones. Thus, observe that for the hexagon, in Fig. 3.26(a), where the localization is weakest, there is one main loop, carrying most of the current, formed on the two sides parallel to the magnetic field direction, where the snaking states are formed, and two additional weaker ones

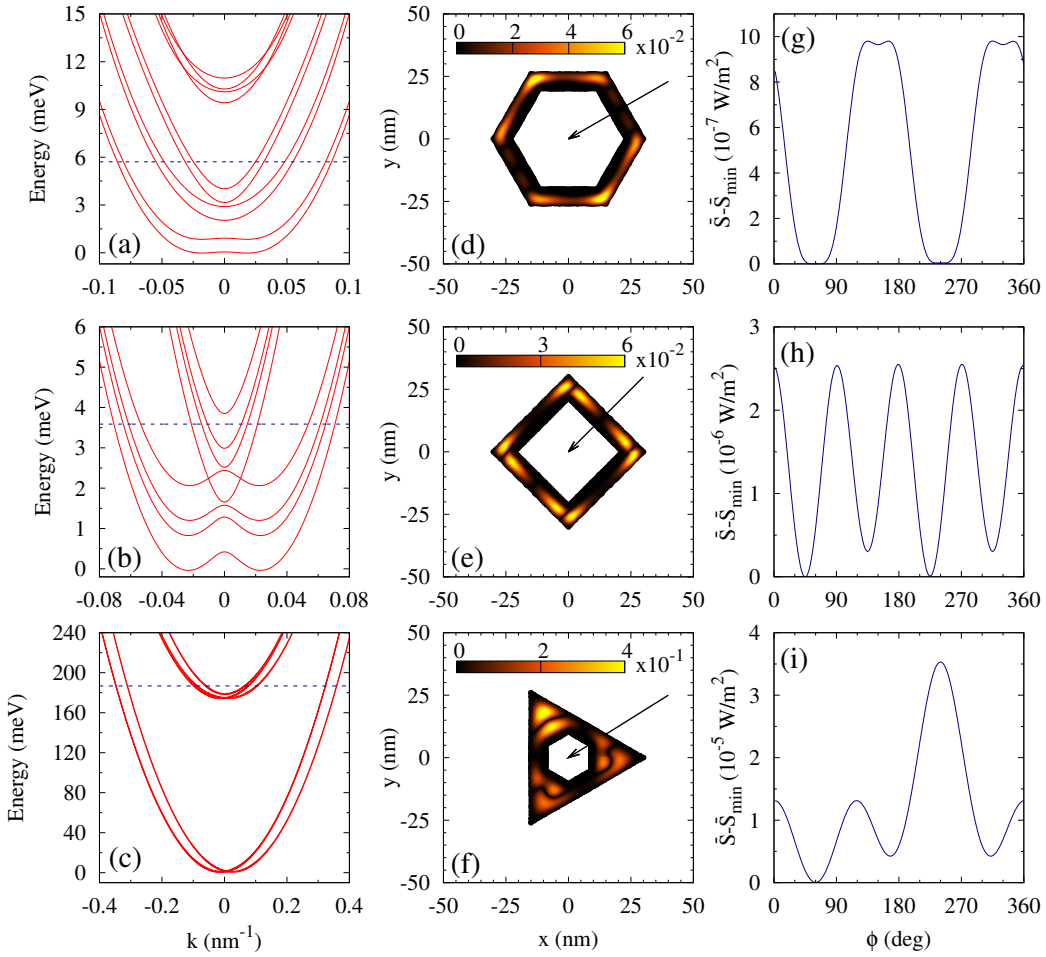

Figure 3.28: As in Fig. 3.27 changing the direction of the external magnetic field to be perpendicular to one of the facets of the hexagonal and square nanowires, and parallel for the triangular [indicated by the arrows in (d-f)]. The color scale units are $\mathrm{A}/(\mathrm{s}\cdot\mathrm{nm}^2)$.

on the perpendicular sides. In the case of the square, Fig. 3.26(b), the situation is similar, a loop that connects opposite corners and two additional ones on the corners perpendicular to the field direction. For the triangular case, Fig. 3.26(b), where the localization is the strongest, there are three loops, with each corner being densely populated. The time derivative of the current density ($d\boldsymbol{J}/dt$), shown in in Figs. 3.27(d-f), however, has the same sign for electrons moving along the length of the nanowire in opposite directions, as they are oppositely being accelerated or slowed down.

In Figs. 3.27(g-i) the magnetic field effects in the relative differences of the power density are shown. The minimum values of the power density are now $\overline{S}_{min} = 1.74$, 2.23, 15.45 $\cdot 10^{-4}$ W/m^2 for hexagonal, square and triangular nanowires, respectively. For the hexagonal nanowire a clear difference with respect to the case without external magnetic field [Fig. 3.24(g)] is observed. Instead of the six corner-related peaks now only two main ones appear with some shoulders. The reason is that now the Lorentz force pushes the current density to the sides where the snaking states are formed, which carry most of the current. Note, however, that the time-average Poynting vector is an integration over a complete period; when the chemical potentials are imbalanced, the nanowire quickly carries net current only in one direction and thus, over half of a period

the contribution of one of the two sides is much smaller. Contrarily, the contribution of the two other regions where the additional loops are formed remains relevant during a complete period. Thus, on average, the two peaks of the maximum radiated power density appear on the angles where the two corners perpendicular to the field are. For clarity, to illustrate this both the current density distribution and its time derivative over a complete period are shown in the Appendix Sections A.3 and A.4. The situation is, to some extent, similar in the case of the square, but the difference in this case lies in the fact that each corner hosts current in both directions. Thus, integrating over a period, there are still four peaks in the power density but with different intensity. For the carrier density consideredm the triangular case, as the localization is stronger and the current distribution is locked in each corner, do not offer big differences with respect to the case without magnetic field for the same carrier density (not shown), and its radiated field is similar to the previously discussed. For this reason, a carrier density of $n = 10^{-3}$ nm^{-3} was used, so that the chemical potential crosses the next group of states, for which the localization is weaker. The Lorentz force then unlocks the formation of current loops on the side opposite to its direction from one corner to the other, which carry most of the current, and it is reflected in the power density curve where now only two clear peaks corresponding to the current carried along the corners of this side are observed.

Taking advantage of the localization mechanism induced by the external magnetic field, it is possible to slightly tune the directivity of the nanowires. In Fig. 3.28 the same carrier density as in the previous case was considered, but now the direction of the magnetic field was changed to be perpendicular to one of the facets of the hexagonal and square nanowires and parallel for the triangular. As illustrated in Fig. **??**, a change in the orientation of the field changes the electron distribution, resulting in a change of the current density distribution and the pairing of channels in the loops. As can be seen in Figs. 3.28(g) and (h), the directivity of the radiated field for the hexagon and the square can be tuned by changing the direction of the magnetic field, which is reflected by a horizontal shift of 30° and 45°, respectively, in the power density peaks. Note that a change in the direction of the magnetic field does not only shifts the power density curves but also creates a different localization which leads to different current density distributions. Thus, this change has also implications on the power density curves, which mainly affects the overlapping of the contributions between the main loop and the weaker ones for the hexagon and the relative difference in their amplitude for the square. In the triangular nanowire the rotation of the field leads to the accumulation of current in the corner opposite to its direction, which translates in the formation of a dominant peak in the power density curve. The minimum values of the power density in this case are $\overline{S}_{min} = 1.74,\ 2.37,\ 15.62 \cdot 10^{-4}$ W/m^2 for hexagonal, square and triangular nanowires, respectively. Additionally, as can be seen in Fig. 3.28(i), because of the absence of a center of inversion in the triangle, the energy spectra is no longer symmetric with respect to k if the magnetic field points parallel to one of the sides.

Finally, for comparison, in Figs. 3.29(a-c) the relative difference of the radiated power density for different orientations of the external magnetic field is shown. As it has been previously described, a change in the magnetic field orientation is translated in a horizontal shift of the power density curve in the case of the hexagonal nanowire, where the geometric localization is weaker. The change of orientation does not only shifts the curve but also changes its shape, as the electrons are being pushed to different areas of the shell and different loops are formed. For the square nanowire, instead, the

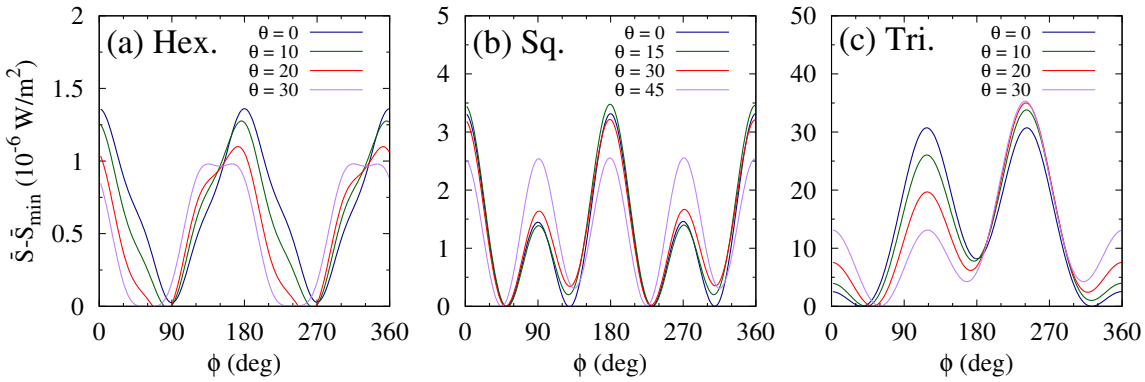

Figure 3.29: Relative difference of the time-averaged Poynting vector as a function of the angle for different orientations for the three different geometries. The angle of the magnetic field is varied in steps of 10° for the hexagonal and triangular nanowires and steps of 15° for the square. As in the previous cases the power density is measured at a distance of $2R_{\text{ext}}$ from the center of the nanowire.

change of orientation of the field does not shift the curves, as the localization which stems from its geometry is stronger than for the hexagonal case, but leads to a change of the contribution from each corner. For the triangular nanowire, for which a higher carrier density ($n = 10^{-3}$ nm^{-3}) was considered, a rotation of the magnetic field leads to a gradual decrease of the power density emitted by the current hosted by the corner perpendicular to its direction, as the Lorentz force pushes the current to the opposite side, where the main loop is formed.

3.6 Light scattering

The results in this section are arranged in two parts. The first one contains the description of the study of the scattering cross section of cylindrical nanowires where an internal gap is included. The effects of a varying internal radius and changes in the dimensions of the cylinders in the scattering properties are explored. In the second one, prismatic nanowires are considered. The consequences of the geometry, reflected in an anisotropic scattering of light depending on the angle of incidence, in the scattering cross section spectra and directivity are presented. The first part is excerpted from the results published in Ref. [151] and the second part from the results published in Ref. [152].

3.6.1 Light scattering in tubular cylindrical nanowires

3.6.1.1 Short nanowires

First, the scattering cross section is studied for short cylindrical particles in which a longitudinal hole of increasing radius is created. Such hollow dielectric particles, whose dimensions are smaller than the light wavelength, are known to support strong magnetic or electric Mie resonances. A normally incident plane wave may excite either vertical TE or TM modes [96].

As expected, with increasing the internal radius of the tubular structure, the resonant scattering modes are blue-shifted, because the thickness of the cylindrical shell is

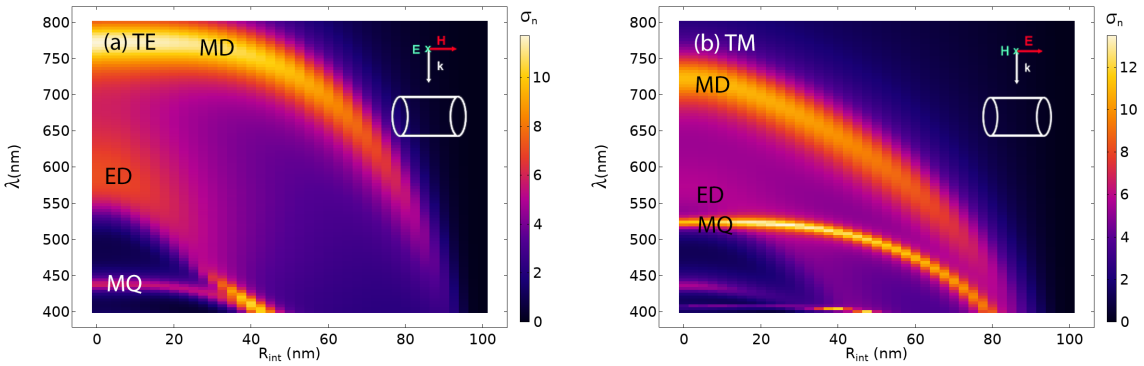

Figure 3.30: Normalized scattering cross section spectral dependence on internal radius R_{int} for a short nanowire under TE polarization (a) and TM polarization (b). In both cases the nanowire length is $L = 150$ nm.

reduced, and thus the effective scattering volume shrinks. However, not all the modes decay with the same rate. As shown in Fig. 3.30 under TE polarization, the electric dipole (ED) shifts remarkably faster than the magnetic dipole (MD) and the magnetic quadrupole (MQ). The MD, oriented along the axis of the cylinder, is almost unaffected for $R_{\text{int}} < 40$ nm, since the displacement currents that create it are stronger on the outer part of the nanowire. Under TM polarization both the ED and the MD are shifted in the same way. It can also be observed that the MD mode predominates when the impinging light is TE polarized whereas under TM polarized light the MQ becomes the dominant mode. A detailed explanation of the behavior of these modes can be found in [96].

3.6.1.2 Long nanowires

As the length of the nanowires increases, the resonant Mie modes evolve until they converge to those of an infinite cylinder. These transverse resonances may coexist with such longitudinal guided modes, as Fabry-Pérot resonances start to develop as a function of the length. This is the result of the transverse modes bouncing back and forth along the length of the nanowire. These overlapping of transverse and longitudinal modes leads to sharp Fano resonances [118].

Here, it is explored how to tailor the Fano resonances by changing the geometry of the nanowires. The presence of the longitudinal hole distorts the Mie transverse modes in the same way as for the short nanowires studied in the previous section. However, the guided modes are affected in a different way.

The guided sharp TE_{01} modes are associated to the reflections of the purely transversal MD and overlap with the broad MD background leading to the sharp Fano resonances. The guided modes for TM polarization are also associated with the MD mode, which has now longitudinal symmetry, and the reflections along the length of the nanowire lead to hybrid Fabry-Perot modes (HE_{11}).

As shown in Fig. 3.31 under TE incidence, the guided modes (TE_{01}) are almost unaffected by the increasing internal radius since they are associated to the MD. This situation allows for the inversion of the symmetry of the Fano resonances because the blue-shift of the broad ED mode is much faster. On the other hand, under TM polarization both the Mie background and the hybrid guided modes (HE_{11}) are blue-shifted at equivalent rates, and thus the crossing of the main resonant peaks is avoided.

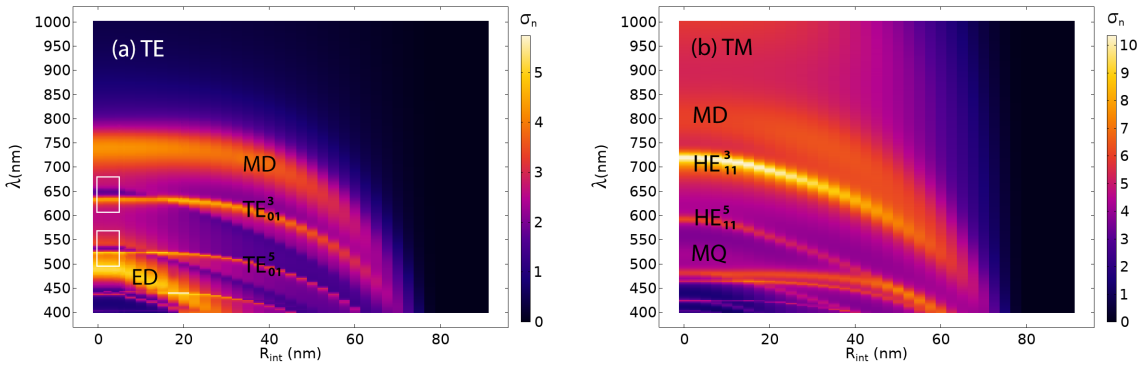

Figure 3.31: As in Fig. 3.30 but for $L = 600$ nm. The rectangles indicate the ranges where the main Fano resonances occur.

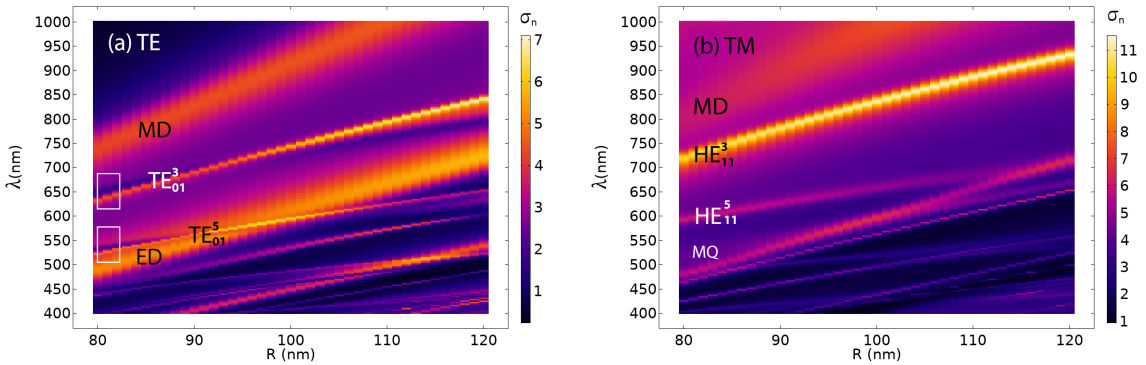

Figure 3.32: Normalized scattering cross section spectral dependence on external radius R_{ext} for a (full) cylindrical nanowire under TE polarization (a) and TM polarization (b). In both cases the length is $L = 600$ nm.

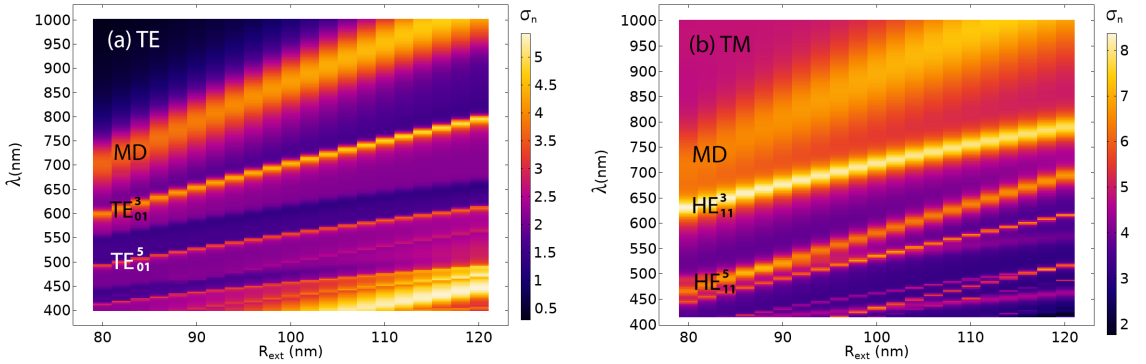

Figure 3.33: Normalized scattering cross section spectral dependence on the external radius R_{ext} for a tubular nanowire with a fixed ratio $R_{\text{int}} = R_{\text{ext}}/2$. In both cases the length $L = 600$ nm.

A detailed description of these modes for cylindrical nanowires, i.e., for which $R_{\text{int}} = 0$, can be found in Ref. [118]. Here the dependence of the scattering spectra on the external radius for cylindrical (Fig. 3.32) and tubular nanowires (Fig. 3.33) with fixed aspect ratio ($R_{\text{int}} = R_{\text{ext}}/2$) are compared. Now the scattering cross section increases with the radius, and thus all the modes are red-shifted and their spectral

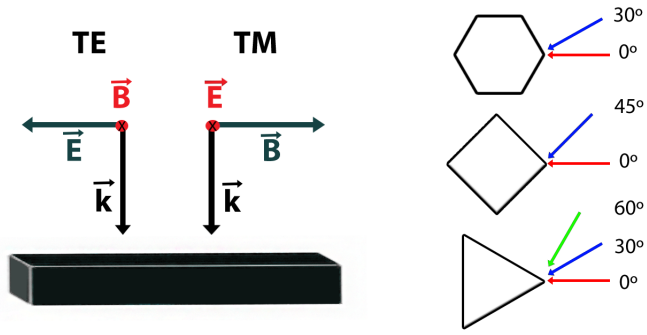

Figure 3.34: Right: sketch of the two polarizations (TE and TM) of the incident light, for example on a nanowire with square cross section. Left: the different angles of incidence studied in each polygonal geometry: hexagonal, square, and triangular.

position depends on the size parameter $x = \pi R_{\text{ext}}^2/\lambda$. Within the studied range of external radii ($R_{\text{ext}} = 80 - 120$ nm) the modes are linearly red shifted with different rates. In the case of a full nanowire exposed to TE polarized light, the increasing radius creates a crossing of modes, which again allows for an inversion of the Fano resonance. However, for the tubular nanowire, the red-shifting rate of the resonant modes does not differ much between the Mie background and the guided modes, again avoiding any crossing in the studied range.

3.6.2 Anisotropic light scattering by prismatic nanowires

In this section the influence of the incidence angle, both in the scattering spectra and in the radiation patterns, is first studied for short ($L = 200$ nm) polygonal nanowires (or nanoparticles) and long nanowires ($L = 600$ nm). The scattering cross section is normalized by dividing, in each case, by the geometrical cross section of a cylindrical nanowire with the same dimensions (radius and length).

The geometrical cross section, i.e., the effective surface of the prismatic nanowire perpendicular to the direction of the incoming light, and the scattering conditions depend on the angle of incidence. Thus, a variation of the scattering spectra is expected to appear as the angle of incidence changes. Because of the symmetries this angle has limited ranges, between $0 - 30°$ for the hexagonal, $0 - 45°$ for the square, and $0 - 60°$ for the triangular case (Fig. 3.34). The geometrical cross section seen by the light varies over these incidence intervals by a factor of $2/\sqrt{3} \approx 1.15$ for the hexagonal and triangular cases, and by $\sqrt{2} \approx 1.41$ for the square, indicating that the square geometry is expected to be more effective. The anisotropy is also expected to increase with the radius of the nanostructures, as the absolute differences in the geometrical cross sections under a change in the incidence angle would also increase, getting closer to the incident light wavelength.

In particular, for triangular nanowires, a rotation of 60° leaves the geometrical cross section unchanged, but due to the lack of an inversion center, it leads to different scattering conditions when the light impinges along a symmetry axis from opposite directions. This effect has already been reported in a recent paper for Si nanopyramids [153]. For the same reason, even if within a specific range, the scattering spectra show almost no difference for different angles of incidence, there may still be a difference

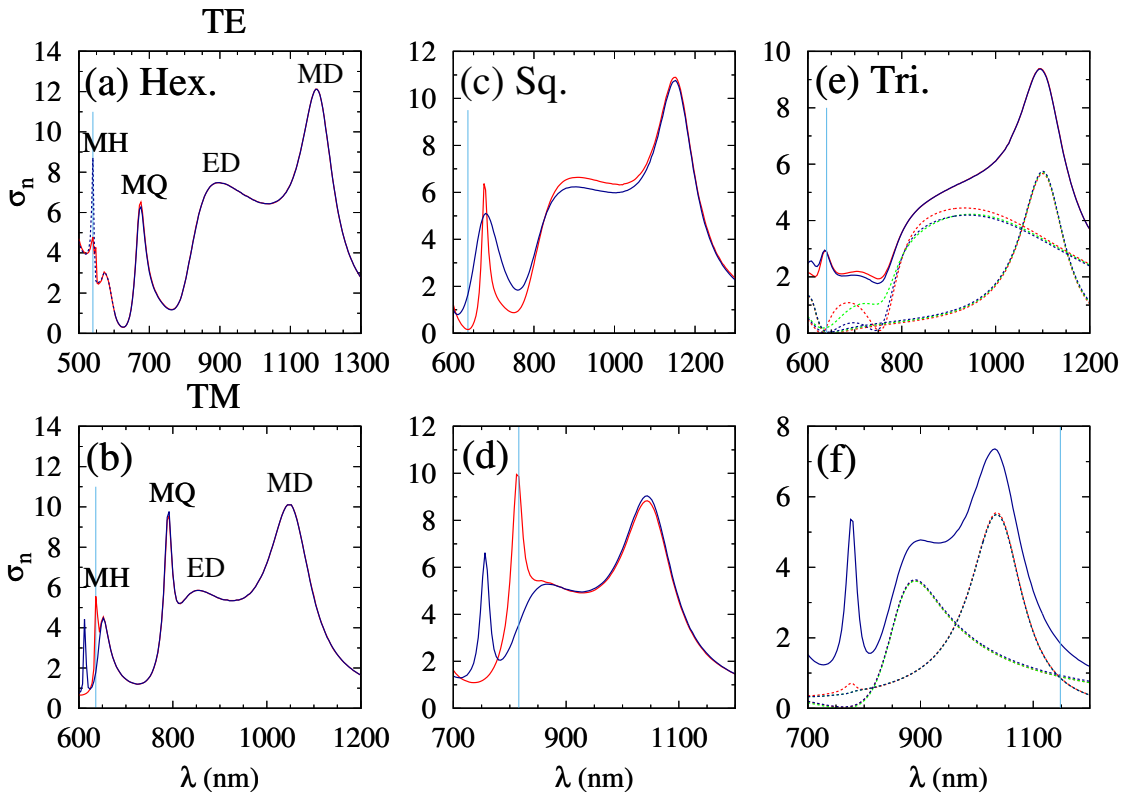

Figure 3.35: The scattering cross section vs. wavelength, for different incidence angles of light, for short nanoprisms with length $L = 200$ nm, of hexagonal (a,b), square (c,d), and triangular (e,f) cross section, with radii $R = 175, 200, 250$ nm, respectively. Figures (a), (c), (e) correspond to TE polarization and (b), (d), (f) to TM polarization. The colors of the curves match the colors of the incidence angles in Fig. 3.34, i.e., the red and blue curves correspond to the scattering cross section obtained with the light incident along the corner-center direction and incident perpendicular to one of the facets of the prism, respectively. In the triangular case the total scattering cross section with the light inciding at 60° is indistinguishable from the case corresponding to 0° and the dashed curves correspond to the individual contributions of the dipole moments (ED and MD). The vertical lines correspond to the wavelength values for which the directivity patterns are shown in Fig. 3.36.

in the contribution from each individual mode [99]. It is also important to note that, under TM polarization the radiation pattern is no longer symmetric when the light incides along one of the sides of the triangle.

3.6.2.1 Short nanowires

Here the light is considered in the near infrared range ($\lambda = 600 - 1200$ nm). The radii of the nanowires are $R = 175, 200, 250$ nm for the hexagonal, square, and triangular profile, respectively and the length is $L = 200$ nm. The reduction of the number of sides leads to a decrease of the volume (keeping the same radius), thus both a blue-shift and a decrease of amplitude of the scattering cross section follows. To compensate for this effect and to be able to compare the results for the three different geometries, the radii are chosen in such a way that the low order modes, i.e., electric (ED) and magnetic (MD) dipoles and magnetic quadrupole (MQ), have

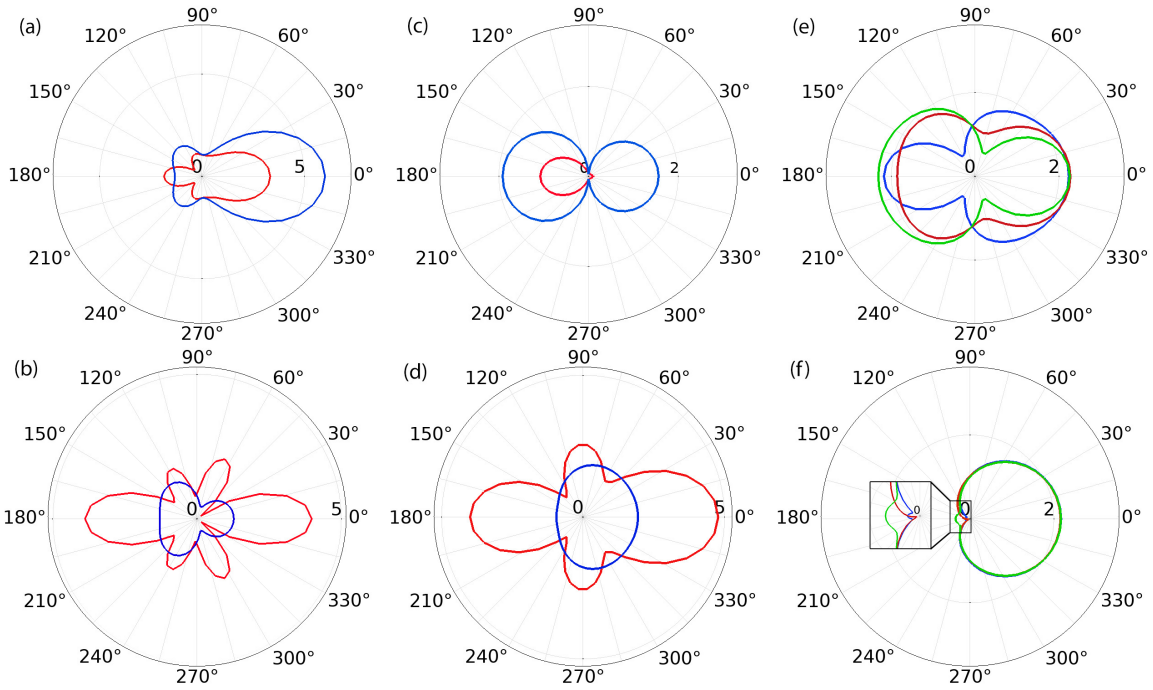

Figure 3.36: 2D radiation patterns for the hexagon (a,b), square (c,d) and triangular (e,f) nanoprisms. 0° corresponds to forward scattering. The colors of the figures again match the colors of the incidence angle shown in Fig. 3.34. For the hexagonal nanoparticle the wavelength is $\lambda = 540$ nm and TE polarization in (a) and $\lambda = 636$ nm and TM polarization in (b). For the square $\lambda = 636$ nm and TE in (c) and $\lambda = 816$ nm and TM in (d). For the triangular case $\lambda = 640$ nm and TE (e) and $\lambda = 1148$ nm and TM where the Kerker condition is satisfied (f). The units for the far-field norm are 10^{-7} V/m.

the main contributions to the total scattering within the same range. In Fig. 3.35 the scattering cross section for the three prismatic geometries is shown with different angles of incidence and in Fig. 3.36 the radiation patterns for the selected wavelengths are shown.

The scattering in the hexagonal prism shows practically no sign of anisotropy on a large interval of wavelengths. Only for the magnetic hexapole (MH) a remarkable difference appears when rotating the angle of incidence, as can be seen in Figs. 3.35(a) and 3.35(b). In Figs. 3.36(a) and 3.36(b) radiation patterns corresponding to the wavelengths marked by the blue lines in Fig. 3.35 are shown. The radiation patterns for the hexagonal nanoparticle under the MH modes reveal a clear difference resulting from this anisotropy, as the MH is either diminished under TE or red-shifted under TM conditions. This suggests that the number of sides/corners strongly affects the modes whose symmetry matches the geometry of the sample.

Indeed, for the square geometry, a significant difference now in the MQ is observed in Figs. 3.35(c) and 3.35(d). For $\lambda = 636$ nm, under TE polarization, we can observe an interesting situation [Fig. 3.36(c)] in which the forward scattering is almost completely cancelled when the light impinges perpendicular to one of the corners, as the scattering cross section is almost zero for that wavelength. For TM polarization a considerable red-shift of the MQ mode is observed, and the directivity pattern shown in Fig. 3.36(d) clearly reflects this remarkable change. Due to their matching modes, both the square

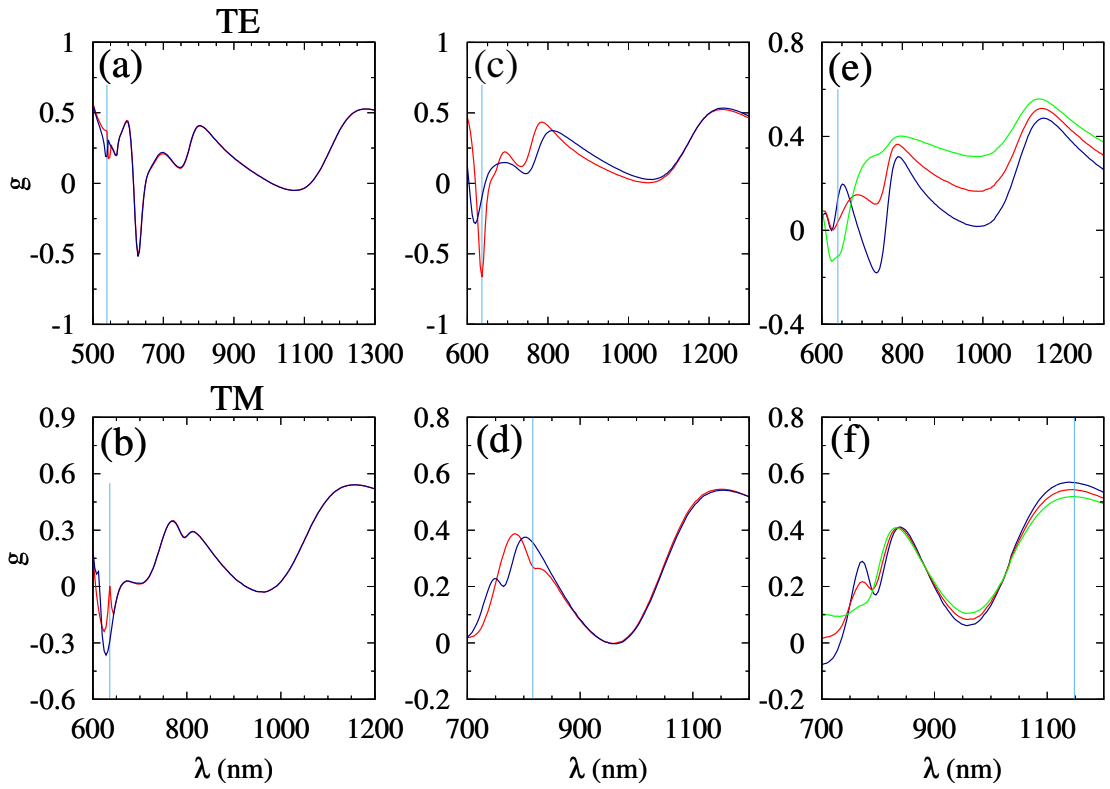

Figure 3.37: Asymmetry parameter as a function of the wavelength for the hexagonal (a,b), square (c,d), and triangular (e,f) nanoprisms as in Fig 3.35. The blue lines also correspond to the same wavelength for which the directivity patterns where obtained in Fig. 3.36.

and the hexagonal geometry allow for a high degree of tunability through the rotation of the incidence angle.

As pointed out previously, for the wavelength intervals for which the scattering spectra are not sensitive to the angle of incidence, one may still expect a difference in the contribution from each individual mode, and thus different radiation patterns. However, in all the cases tested for the square and the hexagon, the directivities are almost completely insensitive to the angle of incidence. In Fig. 3.37 the asymmetry parameter corresponding to the nanoprisms in the studied wavelength range is shown. As can also be observed, only a slight degree of anisotropy occurs aside the aforementioned modes. Only for the triangular case this effect has a significant magnitude, in Figs. 3.35(e) and 3.35(f) the individual contributions of the dipole moments are shown, where the underlying anisotropy, despite the invariance in the total scattering cross section is revealed. This is also distinctly reflected in the differences of its asymmetry parameter, specially under TE polarization [Fig. 3.37(e)] over the whole range of wavelengths. Remarkably, as observed at $\lambda \approx 750$ nm, the scattering direction can be switched from being predominantly forward to backward by a rotation of 60°, as the asymmetry parameter changes its sign. The MQ mode is clearly diminished under TE polarization as the mode no longer matches the geometry of the sample. Instead, for TM, as the mode is longitudinal, the MQ remains unaffected. The radiation patterns for the MQ are shown in Fig. 3.36(e), revealing a highly anisotropic scattering as expected by its asymmetry parameter.

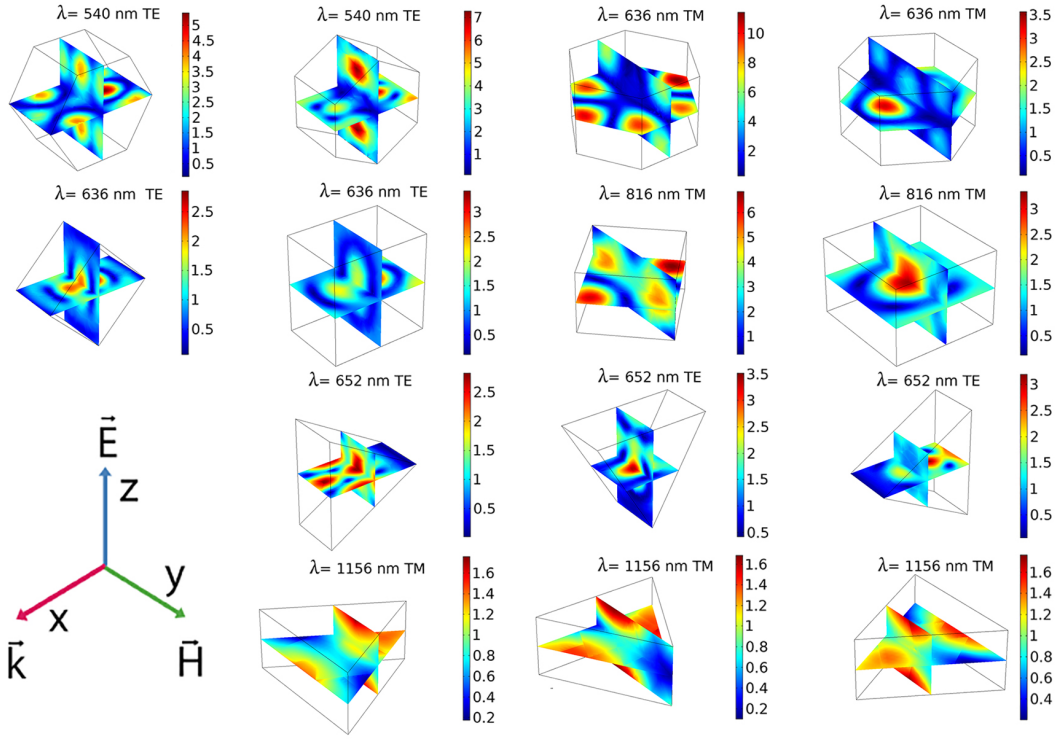

Figure 3.38: Electric field configurations inside the nanoparticles. The direction of incidence of the light is parallel to the x axis with TE or TM polarization depending on the orientation of the nanoparticles. The units of the electric field in the color scale are V/m.

When the magnitude of the ED and the MD are equal (situation known as the first Kerker condition) the backward scattering is cancelled via destructive interference. In Fig. 3.36(f), the directivity pattern when this condition is satisfied, for the triangular nanowire (under TM polarization), shows a slight difference, also observable in Fig. 3.37(f), due to the dependence of the individual dipole modes to the illumination direction.

Finally, the electric field configurations inside the nanoparticles for all the cases considered here are shown in Fig. 3.38. As expected, taking into account the previous results, the electric field inside the particles is rather sensitive to the angle of incidence for the cases where anisotropic scattering is observed. In particular, when the light impinges the nanoparticles with TM polarization, the shift of the MH ($\lambda = 636$ nm) and MQ ($\lambda = 816$ nm) for the hexagon and the square, respectively, is clearly reflected in the electric field configurations. Both completely disappear and the magnitude of the electric field is remarkably diminished, when the incidence is rotated from being perpendicular to one edge to being perpendicular to one side, in accordance to the results shown in Fig. 3.35. The anisotropic scattering of the triangular nanoparticle, despite having the same value of the scattering cross section, is also reflected under TE polarization for the MQ ($\lambda = 652$ nm). The lack of an inversion center results in completely different field configurations inside the nanoparticle when the light impinges perpendicular to one facet or perpendicular to one edge. For TM, in the Kerker condition ($\lambda = 1156$ nm), the field configuration shows little difference, leading to isotropic scattering in accordance to the directivity patterns shown in Fig. 3.36.

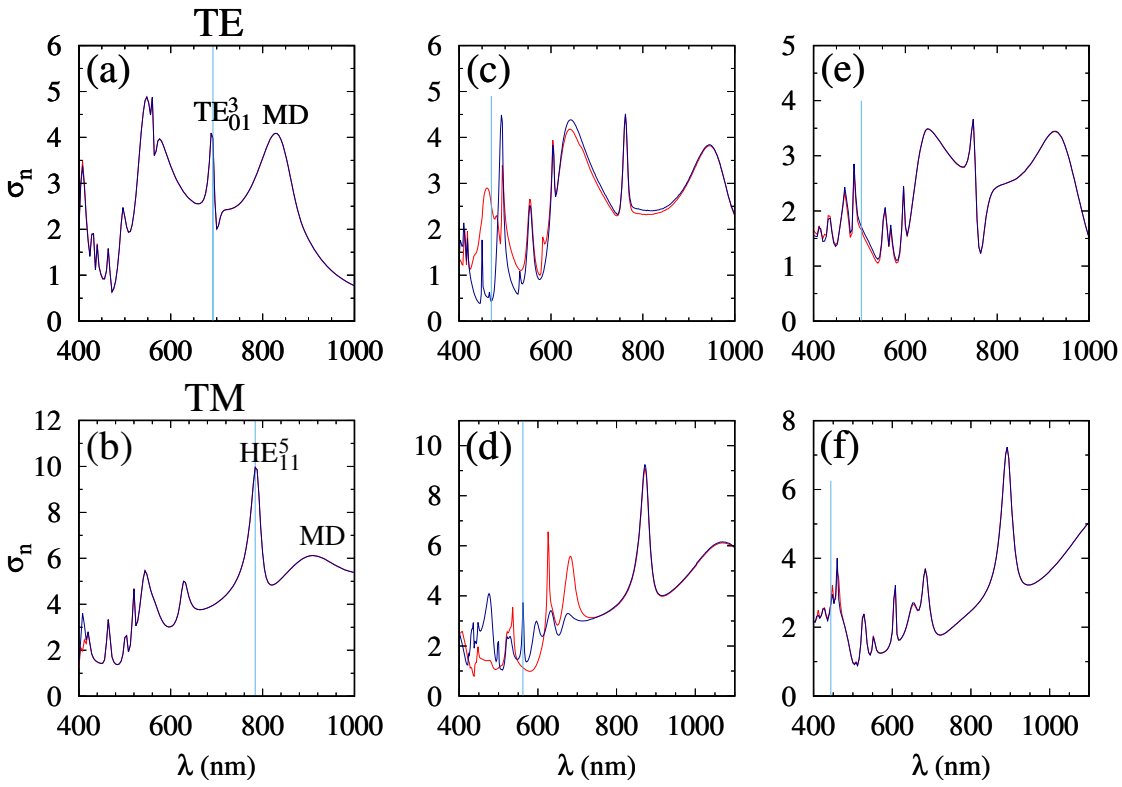

Figure 3.39: As in Fig. 3.35 for nanowires with radii of $R = 100, 135, 175$ nm for hexagonal, square, and triangular geometry, respectively, and $L = 600$ nm.

3.6.2.2 Long nanowires

Longer nanowires have richer and more complex scattering spectra. As it was mentioned in Section 3.6.1.2, Mie resonances now coexist with longitudinal guided modes that develop as the length increases. The guided modes are the result of Fabry-Perot interferences, and the overlapping of transverse and longitudinal modes leads to sharp Fano resonances which can be observed in the scattering cross section spectra.

Light is now considered in the range of $\lambda = 400 - 1100$ nm to also include higher-order modes. For these modes the wavelength is closer to the geometrical cross section difference of the structure under rotation and thus, they are much more sensitive to the incidence angle.

In Fig. 3.39 the scattering cross section dependence on the angle of incidence for the nanowires with radii of $R = 100, 135, 175$ nm for hexagonal, square, and triangular profiles, respectively, is shown and in Figs. 3.40 and 3.41 the corresponding directivity patterns and asymmetry parameters are shown. The length is now $L = 600$ nm in all cases. The guided sharp TE_{01} modes are associated to the reflections of the purely transversal MD and overlap with the broad MD background leading to the sharp Fano resonances. The guided modes for TM polarization are also associated with the MD mode, which has now longitudinal symmetry, and the reflections along the length of the nanowire lead to hybrid Fabry-Perot modes (HE_{11}).

The dimensions (radii and length) of the nanowires are chosen in such a way that the resonances studied in Refs.[118] and [151] are obtained, and are treated as a reference point. The main Fano resonances are seen in Fig. 3.39(a) and 3.39(b), coming from the

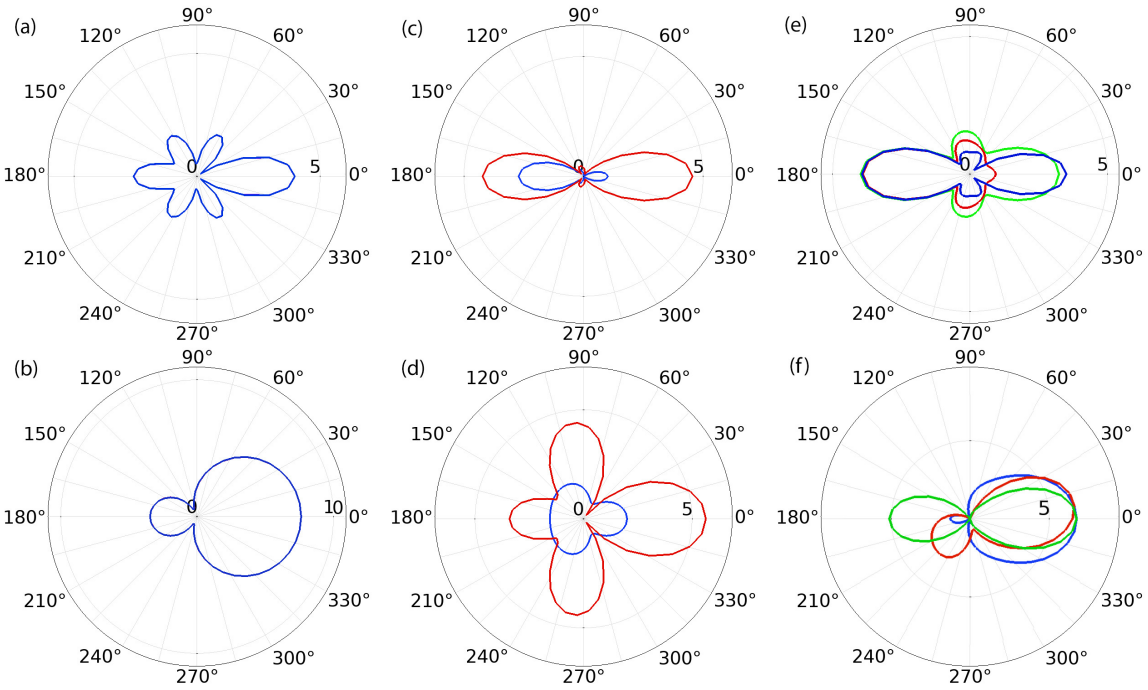

Figure 3.40: 2D radiation patterns for the hexagonal nanowires for TE at $\lambda = 692$ nm (a) and TM at at $\lambda = 784$ nm (b). Square nanowire for TE at $\lambda = 470$ nm (c) and for TM at $\lambda = 562$ nm (d). (e) and (f) for the triangular nanowires at $\lambda = 504$ nm and $\lambda = 444$ nm for TE and TM polarizations, respectively. The color code is the same as in Fig. 3.36.

overlapping of the TE_{01}^{3} and HE_{11}^{5} modes, respectively, with the MD. A more detailed analysis of these modes can be found in [118] for cylindrical nanowires.

In this case, a nearly isotropic scattering cross section for the hexagonal nanowire in Figs. 3.39(a) and 3.39(b) can be observed, both under TE and TM, also reflected in the corresponding asymmetry parameter in Fig. 3.41. The radiation patterns for the TE_{01}^{3} and HE_{11}^{5} modes are shown in Figs. 3.40(a) and 3.40(b), respectively, and reveal a field distribution insensitive to the incidence angle. As the radius is smaller in this case, the geometrical cross section difference under a rotation of the angle of incidence is also smaller. Thus, the anisotropy is still expected to appear but for shorter wavelengths and, again, especially in those modes whose geometry matches the sample, i.e., magnetic hexapole and its associated longitudinal modes.

On the contrary, the square nanowire, Figs. 3.39(c) and 3.39(d), shows remarkable anisotropic scattering cross sections and asymmetry parameters within a wide range of wavelengths. Consequently, a rich set of directivity patterns with flexible tunability is allowed. These high-order modes are rather complex, and their interference and overlapping makes their classification almost unviable. The directivity patterns shown in Fig. 3.40 correspond to wavelengths where interesting features appear. A nearly complete suppression of the forward scattering [Fig. 3.40(c)] is still possible through the interference of high-order modes, but now a much sharper directivity is achieved. In Fig. 3.40(d) a situation similar to the one discussed in the previous section is observed. The radiation pattern reveals a MQ-like behavior, highly anisotropic as it matches the geometry of the square nanowire.

Interestingly, the triangular nanowire also shows a highly anisotropic directional scattering despite the negligible differences in the scattering cross section spectra, both

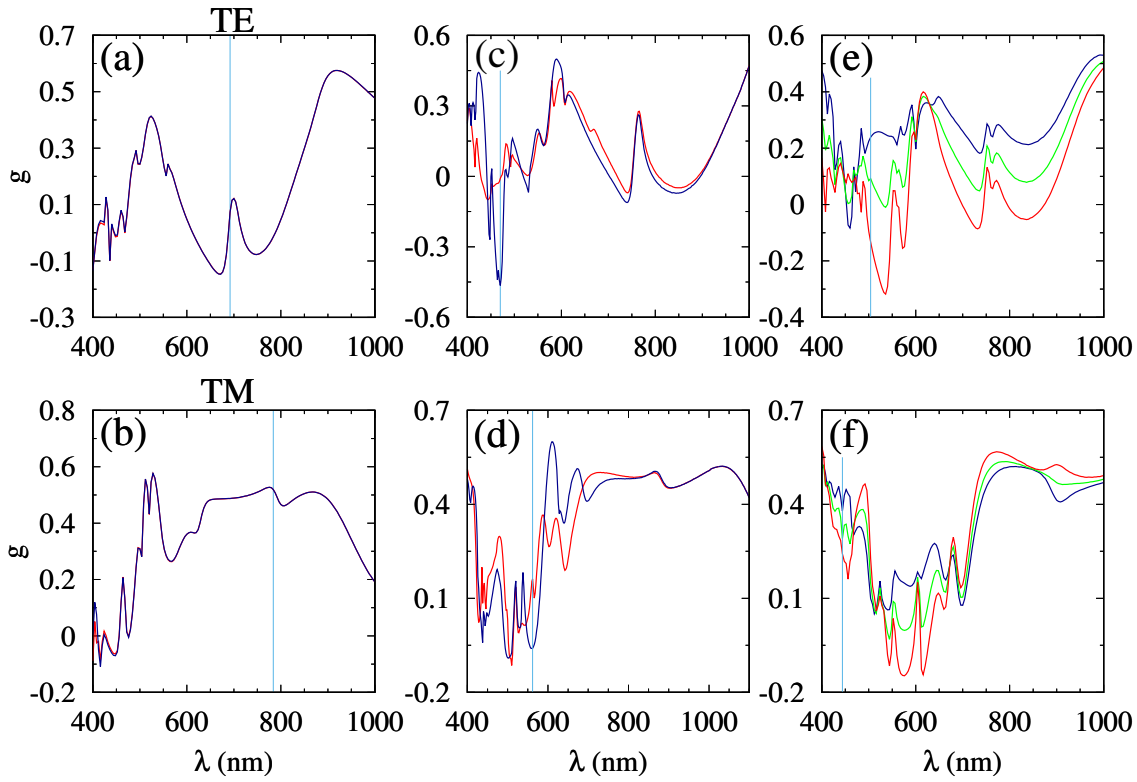

Figure 3.41: Asymmetry parameter as a function of the wavelength as in Fig. 3.37 for long nanowires.

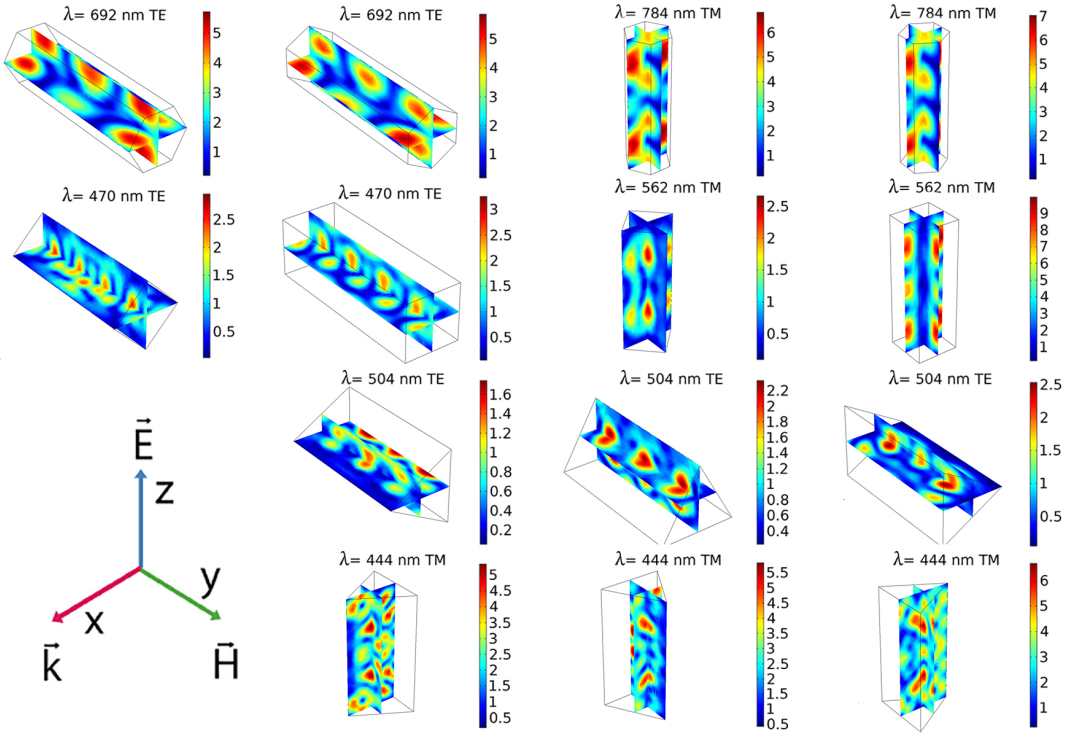

Figure 3.42: Electric field configurations inside the nanowires, as in Fig. 3.38.

under TE and TM polarization, as seen in the asymmetry parameter in Figs. 3.41(e) and 3.41(f). The high anisotropy also occurs within a wide range of wavelengths,

and, to some degree, it also extends to longer ones. In this case, a diminishment of the forward scattering is also achievable [Fig. 3.40(e)] at $\lambda = 504$ nm under TE polarization when the light impinges perpendicular to one corner. Because of its asymmetric scattering under TM polarization, the angle of maximum scattering could be rotated up to 15° [Fig. 3.40(f)].

As for the previously discussed short nanowires, in Fig. 3.42 the electric field configurations for all the cases considered in this subsection are shown. Here, the field configurations are much more complex as more modes, both transverse and longitudinal, contribute and overlap. It is still possible to identify the key features. It is possible to clearly observe that the longitudinal modes are the result of the rebound along the length of the nanowires of the transversal ones. For the hexagonal nanowire, the TE_{01}^{3} ($\lambda = 692$ nm) and HE_{01}^{5} ($\lambda = 784$ nm) modes change only very slightly when rotating the angle of incidence, as expected from the isotropic scattering shown in Fig. 3.40. For the cases of the square and, especially, triangular nanowires, the anisotropy is clearly reflected through the changes in the electric field inside the nanowires. In particular, it is remarkable how anisotropic the electric field is in the triangular case, even when the scattering cross section shows almost negligible variations, contrarily to the hexagonal case, which is in accordance with the directivity patterns of Fig. 3.40.

Chapter 4

Conclusions

The main goal of this thesis has been to demonstrate the specific role of the geometry -often overlooked by experimentalists- in several of the fundamental electrical and optical properties of prismatic CSNs.

In the first part of this work, several features of the quantum states and the conductance of CSNs which are consequences of the internal geometry have been investigated, focusing in nanowires with a conductive shell and an insulating core. Most of the presented results are determined by the energy spectra and by the geometric localization of the electrons. In the ballistic cases, with no impurities, there is no real need for transport calculations, the conductance can be obtained by simply counting the transverse modes. The transport calculations that were performed are intended to support the predictions from the spectra, in a qualitative manner. One of the most interesting aspects is that the states localized on the edges and those localized on the facets can be separated by a large energy gap, such that a single core-shell nanowire may possibly function like a collection of of thinner nanowires. CSNs exposed to a transverse external magnetic field have also been shown to exhibit complex localization mechanisms which are rich in phenomenology. The direction and magnitude of the magnetic field allows for the tunability of the electron localization and creates current loops, i.e., channels of current where electrons travel in opposite directions.

In order to study the consequences of the electron localization induced by this mechanism, we obtained the radiated power density as a function of the angle, in the near field region. We showed that the radiated electromagnetic field can capture the electron and current density localization and we studied how it is affected by a magnetic field transverse to the nanowire, with different angular orientations. Rather than an in-depth study of the magnitude of the emitted power in different situations, our goal was to demonstrate, more qualitatively than quantitatively, that the resulting field is anisotropic and with a tunable directivity, first via the geometry and internal structure of the nanowire, and second with an external magnetic field. Although we restricted our study to individual nanowires, the extension of the ideas to arrays of parallel nanowires, as nanowires are often grown, to achieve a combined effect and increased power, is straightforward.

Properties of excitons confined in triangular, square, and hexagonal shells have also been investigated. It was shown that the states corresponding to the same or similar electron distributions are arranged into quasi-degenerate levels. The exceptions are the states associated with both the conduction electron and the vacancy localized in the same corner. Only a fraction of these states (3p states) in the spin triplet configurations form the lowest, nearly dispersionless, level while the remaining states

in the spin singlet configuration are shifted to much higher energies. The number of such states equals the number of corners, and the set reproduces the degeneracy of single-particle corner states with respect to the spin. For most of the samples these purely corner states mix with states corresponding to conduction electrons localized on the sides. However, if the samples are narrow and the external radii are small, i.e., if the gaps between single-particle corner and side states in the conduction band are sufficiently large, these states fit into the interval that separates excitonic states with the conduction electron occupying a corner area or localized on a side and form distinct excitonic in-gap states. In the case of triangular shell, the largest gap within the energy spectrum originates from the separation of single-particle corner and side states, but for square and hexagonal shells the Coulomb-induced splitting between the two lowest levels becomes the dominant one.

In the second part of the work, several features regarding the light scattering characteristics of the nanowires were investigated. The geometrical optical resonances of semiconductor cylindrical and polygonal nanowires have been obtained in order to explore the role of the geometry in the scattering properties.

The tubular structure has been shown to offer an additional degree of freedom for tuning the spectral position of the resonant modes. Since various modes are affected in different ways by the geometrical parameters it is possible to invert Fano resonances and change the spectral spacing between modes. This possibility is explored both in full nanowires by changing the external radius and in tubular structures by changing the internal radius.

In prismatic nanowires the scattering of light by depends on the illumination direction. When the geometrical cross section difference of the structures under a rotation is comparable to the incident light wavelength a strongly anisotropic scattering occurs, especially for the square geometry. This allows for the possibility of a flexible in-situ tuning of the directivity by a simple change of the incidence angle or by changing the light polarization. Forward scattering may be considerably diminished this way, allowing for interesting applications in switching or sensing. The scattering spectra can be shifted in multiple ways by scaling either the radius, the length, or the aspect ratio of the nanowires. In particular, it is important to note that even if the high-order resonant modes would easily vanish from the visible domain because of absorption, which has been neglected, still, they would be achievable in larger samples. This is due to Maxwell's equations scaling, by red-shifting the modes to the spectral region where the absorption is negligible for common semiconductor materials like Si, Ge, or III-V compounds. Apart from the geometric variables, the refractive index of the material is another parameter that can shift the resonances of the scattering spectra.

Bibliography

1. Cheng, X. 10 - Nanostructures: fabrication and applications (ed Feldman, M.) 348 –375 (2014).
2. Fortuna, S. A. & Li, X. Metal-catalyzed semiconductor nanowires: a review on the control of growth directions. *Semiconductor Science and Technology* **25,** 24–105 (2010).
3. Garnett, E., Mai, L. & Yang, P. Introduction: 1D Nanomaterials/Nanowires. *Chemical Reviews* **119,** 8955–8957 (2019).
4. Samuelson, L. *et al.* Semiconductor nanowires for 0D and 1D physics and applications. *Physica E: Low-dimensional Systems and Nanostructures* **25.** Proceedings of the 13th International Winterschool on New Developments in Solid State Physics - Low-Dimensional Systems, 313 –318 (2004).
5. Thelander, C. *et al.* Nanowire-based one-dimensional electronics. *Materials Today* **9,** 28 –35 (2006).
6. Lu, W. & Lieber, C. M. Semiconductor nanowires. *Journal of Physics D: Applied Physics* **39,** R387–R406 (2006).
7. Noborisaka, J., Motohisa, J., Hara, S. & Fukui, T. Fabrication and characterization of freestanding GaAs-AlGaAs core-shell nanowires and AlGaAs nanotubes by using selective-area metalorganic vapor phase epitaxy. *Applied Physics Letters* **87,** 093109 (2005).
8. Barrigón, E., Heurlin, M., Bi, Z., Monemar, B. & Samuelson, L. Synthesis and Applications of III-V Nanowires. *Chemical Reviews* **119,** 9170–9220 (2019).
9. Tomioka, K., Yoshimura, M. & Fukui, T. F. A III-V nanowire channel on silicon for high-performance vertical transistors. *Nature* **488** (2012).
10. Wirths, S. *et al.* Effect of Si-doping on InAs nanowire transport and morphology. *Journal of Applied Physics* **110,** 053709 (2011).
11. Richter, T. *et al.* Flux Quantization Effects in InN Nanowires. *Nano Letters* **8,** 2834–2838 (2008).
12. Blömers, C. *et al.* Phase-coherent transport in InN nanowires of various sizes. *Phys. Rev. B* **77,** 201301 (2008).
13. Heedt, S. *et al.* Adiabatic Edge Channel Transport in a Nanowire Quantum Point Contact Register. *Nano Letters* **16,** 4569–4575 (2016).
14. Law, M., Goldberger, J. & Yang, P. Semiconductor nanowires and nanotubes. *Annual Review of Materials Research* **34,** 83–122 (2004).
15. Gudiksen, M. S., Lauhon, L. J., Wang, J., Smith, D. C. & Lieber, C. M. Growth of nanowire superlattice structures for nanoscale photonics and electronics. *Nature* **415,** 617–620 (2002).

16. Royo, M., Luca, M. D., Rurali, R. & Zardo, I. A review on III–V core–multishell nanowires: growth, properties, and applications. *Journal of Physics D: Applied Physics* **50,** 143001 (2017).
17. Bhuyan, P. D. *et al.* Si and Ge based metallic core/shell nanowires for nanoelectronic device applications. *Scientific Reports* **8,** 16885 (2018).
18. Steidl, M. *et al.* Impact of Rotational Twin Boundaries and Lattice Mismatch on III-V Nanowire Growth. *ACS Nano* **11,** 8679–8689 (2017).
19. Balaghi, L. *et al.* Widely tunable GaAs bandgap via strain engineering in core/shell nanowires with large lattice mismatch. *Nature Communications* **10,** 2793 (2019).
20. Pistol, M.-E. & Pryor, C. E. Band structure of core-shell semiconductor nanowires. *Phys. Rev. B* **78,** 115319 (2008).
21. Wong, B. M., Léonard, F., Li, Q. & Wang, G. T. Nanoscale Effects on Heterojunction Electron Gases in GaN/AlGaN Core/Shell Nanowires. *Nano Letters* **11,** 3074–3079 (2011).
22. Blömers, C. *et al.* Realization of nanoscaled tubular conductors by means of GaAs/InAs core/shell nanowires. *Nanotechnology* **24,** 035203 (2013).
23. Plochocka, P. *et al.* High Magnetic Field Reveals the Nature of Excitons in a Single GaAs/AlAs Core/Shell Nanowire. *Nano Letters* **13,** 2442–2447 (2013).
24. Pemasiri, K. *et al.* Quantum confinement of excitons in wurtzite InP nanowires. *Journal of Applied Physics* **117,** 194306 (2015).
25. Fan, H. *et al.* Single-crystalline $MgAl_2O_4$ spinel nanotubes using a reactive and removable MgO nanowire template. *Nanotechnology* **17,** 5157 (2006).
26. Shtrikman, H., Popovitz-Biro, R., Kretinin, A. & Heiblum, M. Stacking-Faults-Free Zinc Blende GaAs Nanowires. *Nano Letters* **9,** 215–219 (2009).
27. Dong, Y., Tian, B., Kempa, T. J. & Lieber, C. M. Coaxial Group IIINitride Nanowire Photovoltaics. *Nano Letters* **9,** 2183–2187 (2009).
28. Qian, F. *et al.* Controlled Synthesis of AlN/GaN Multiple Quantum Well Nanowire Structures and Their Optical Properties. *Nano Letters* **12,** 3344–3350 (2012).
29. Baird, L. *et al.* Imaging minority carrier diffusion in GaN nanowires using near field optical microscopy. *Physica B: Condensed Matter* **404,** 4933 –4936 (2009).
30. Li, Y. *et al.* Dopant-Free GaN/AlN/AlGaN Radial Nanowire Heterostructures as High Electron Mobility Transistors. *Nano Letters* **6,** 1468–1473 (2006).
31. Rieger, T., Grutzmacher, D. & Lepsa, M. I. Misfit dislocation free InAs/GaSb core-shell nanowires grown by molecular beam epitaxy. *Nanoscale* **7,** 356–364 (2015).
32. Göransson, D. J. O. *et al.* Coulomb blockade from the shell of an InP-InAs core-shell nanowire with a triangular cross section. *Applied Physics Letters* **114,** 053108 (2019).
33. Yuan, X. *et al.* Antimony Induced 112A Faceted Triangular $GaAs_{1x}Sb_x$/InP Core/Shell Nanowires and Their Enhanced Optical Quality. *Adv. Funct. Mater.* **25,** 5300–5308 (2015).
34. Göransson, D. J. O. *et al.* Coulomb blockade from the shell of an InP-InAs core-shell nanowire with a triangular cross section. *Applied Physics Letters* **114,** 053108 (2019).

35. Dick, K. A., Thelander, C., Samuelson, L. & Caroff, P. Crystal Phase Engineering in Single InAs Nanowires. *Nano Letters* **10,** 3494–3499 (2010).

36. Rieger, T., Luysberg, M., Schäpers, T., Grützmacher, D. & Lepsa, M. I. Molecular Beam Epitaxy Growth of GaAs/InAs Core–Shell Nanowires and Fabrication of InAs Nanotubes. *Nano Letters* **12,** 5559–5564 (2012).

37. Haas, F *et al.* Nanoimprint and selective-area MOVPE for growth of GaAs/InAs core/shell nanowires. *Nanotechnology* **24,** 085603 (2013).

38. Fickenscher, M. *et al.* Optical, Structural, and Numerical Investigations of GaAs/AlGaAs Core–Multishell Nanowire Quantum Well Tubes. *Nano Letters* **13,** 1016–1022 (2013).

39. Wu, H., Sprung, D. W. L. & Martorell, J. Electronic properties of a quantum wire with arbitrary bending angle. *Journal of Applied Physics* **72** (1992).

40. Ferrari, G., Cuoghi, G., Bertoni, A., Goldoni, G. & Molinari, E. Electronic and magnetic states in core-multishell nanowires: Edge localization, Landau levels and Aharonov-Bohm oscillations. *Journal of Physics: Conference Series* **193,** 012027 (2009).

41. Bertoni, A., Royo, M., Mahawish, F. & Goldoni, G. Electron and hole gas in modulation-doped GaAs/$Al_{1-x}Ga_xAs$ radial heterojunctions. *Phys. Rev. B* **84,** 205323 (2011).

42. Royo, M., Bertoni, A. & Goldoni, G. Landau levels, edge states, and magnetoconductance in GaAs/AlGaAs core-shell nanowires. *Phys. Rev. B* **87,** 115316 (2013).

43. Jadczak, J. *et al.* Unintentional High-Density p-Type Modulation Doping of a GaAs/AlAs Core–Multishell Nanowire. *Nano Letters* **14,** 2807–2814 (2014).

44. Shi, T. *et al.* Emergence of Localized States in Narrow GaAs/AlGaAs Nanowire Quantum Well Tubes. *Nano Letters* **15,** 1876–1882 (2015).

45. De Luca, M. *et al.* Determination of Exciton Reduced Mass and Gyromagnetic Factor of Wurtzite (InGa)As Nanowires by Photoluminescence Spectroscopy under High Magnetic Fields. *ACS Nano* **7,** 10717–10725 (2013).

46. Blömers, C. *et al.* Realization of nanoscaled tubular conductors by means of GaAs/InAs core/shell nanowires. *Nanotechnology* **24,** 035203 (2012).

47. Gül, O. *et al.* Flux periodic magnetoconductance oscillations in GaAs/InAs core/shell nanowires. *Phys. Rev. B* **89,** 045417 (2014).

48. Manolescu, A. *et al.* Majorana states in prismatic core-shell nanowires. *Phys. Rev. B* **96,** 125435 (2017).

49. Stanescu, T. D., Sitek, A. & Manolescu, A. Robust topological phase in proximitized core–shell nanowires coupled to multiple superconductors. *Beilstein Journal of Nanotechnology* **9,** 1512–1526 (2018).

50. Erlingsson, S. I., Manolescu, A., Nemnes, G. A., Bardarson, J. H. & Sanchez, D. Reversal of Thermoelectric Current in Tubular Nanowires. *Phys. Rev. Lett.* **119,** 036804 (2017).

51. Thorgilsson, G., Erlingsson, S. I. & Manolescu, A. Thermoelectric current in tubular nanowires in transverse electric and magnetic fields. *Journal of Physics: Conference Series* **906,** 012021 (2017).

52. Erlingsson, S. I., Bardarson, J. H. & Manolescu, A. Thermoelectric current in topological insulator nanowires with impurities. *Beilstein Journal of Nanotechnology* **9,** 1156 (2018).

53. Landauer, R. Spatial Variation of Currents and Fields Due to Localized Scatterers in Metallic Conduction. *IBM Journal of Research and Development* **1,** 223–231 (1957).

54. Van Weperen, I., Plissard, S. R., Bakkers, E. P.A. M., Frolov, S. M. & Kouwenhoven, L. P. Quantized Conductance in an InSb Nanowire. *Nano Letters* **13,** 387–391 (2013).

55. Kammhuber, J. *et al.* Conductance through a helical state in an Indium antimonide nanowire. *Nature Communications* **8,** 478 (2017).

56. Gül, O. *et al.* Flux periodic magnetoconductance oscillations in GaAs/InAs core/shell nanowires. *Phys. Rev. B* **89,** 045417 (2014).

57. Rosdahl, T. O., Manolescu, A. & Gudmundsson, V. Spin and impurity effects on flux-periodic oscillations in core-shell nanowires. *Phys. Rev. B* **90,** 035421 (2014).

58. Ferrari, G., Bertoni, A., Goldoni, G. & Molinari, E. Cylindrical two-dimensional electron gas in a transverse magnetic field. *Phys. Rev. B* **78,** 115326 (2008).

59. Manolescu, A., Rosdahl, T., Erlingsson, S., Serra, L. & Gudmundsson, V. Snaking states on a cylindrical surface in a perpendicular magnetic field. *Eur. Phys. J. B* **86** (2013).

60. Rosdahl, T. O., Manolescu, A. & Gudmundsson, V. Signature of Snaking States in the Conductance of Core–Shell Nanowires. *Nano Letters* **15,** 254–258 (2015).

61. Zellekens, P. *et al. Quantum Transport in GaAs/InSb core-shell nanowires* 2019. arXiv: `1911.05510`.

62. Bharadwaj, P., Deutsch, B. & Novotny, L. Optical Antennas. *Adv. Opt. Photon.* **1,** 438–483 (2009).

63. Novotny, L. & van Hulst, N. Antennas for light. *Nature Photonics* **5.** Review Article, 83 EP – (2011).

64. Kullock, R., Ochs, M., Grimm, P., Emmerling, M. & Hecht, B. Electrically-driven Yagi-Uda antennas for light. *Nature Communications* **11,** 115 (2020).

65. Giannini, V., Berrier, A., Maier, S. A., Sánchez-Gil, J. A. & Rivas, J. G. Scattering efficiency and near field enhancement of active semiconductor plasmonic antennas at terahertz frequencies. *Opt. Express* **18,** 2797–2807 (2010).

66. Vitiello, M. S. *et al.* Room-Temperature Terahertz Detectors Based on Semiconductor Nanowire Field-Effect Transistors. *Nano Letters* **12,** 96–101 (2012).

67. Cao, L., Park, J.-S., Fan, P., Clemens, B. & Brongersma, M. L. Resonant Germanium Nanoantenna Photodetectors. *Nano Letters* **10,** 1229–1233 (2010).

68. Grzela, G. *et al.* Nanowire Antenna Emission. *Nano Letters* **12,** 5481–5486 (2012).

69. Friedler, I. *et al.* Solid-state single photon sources: the nanowire antenna. *Opt. Express* **17,** 2095–2110 (2009).

70. Claudon, J. *et al.* A highly efficient single-photon source based on a quantum dot in a photonic nanowire. *Nature Photonics* **4,** 174 EP – (2010).

71. Krogstrup, P. *et al.* Single-nanowire solar cells beyond the Shockley-Queisser limit. *Nature Photonics* **7,** 306–310 (2013).

72. Kim, S.-K. *et al.* Doubling Absorption in Nanowire Solar Cells with Dielectric Shell Optical Antennas. *Nano Letters* **15,** 753–758 (2015).

73. Peköz, R., B., M. O. & Raty, J.-Y. First-principles design of efficient solar cells using two-dimensional arrays of core-shell and layered SiGe nanowires. *Phys. Rev. B* **83,** 035317 (2011).

74. Cao, L. *et al.* Semiconductor Nanowire Optical Antenna Solar Absorbers. *Nano Letters* **10,** 439–445 (2010).

75. Tang, J., Huo, Z., Brittman, S., Gao, H. & Yang, P. Solution-processed core-shell nanowires for efficient photovoltaic cells. *Nature Nanotechnology* **6,** 568–572 (2011).

76. Yu, Y., Ferry, V. E., Alivisatos, A. P. & Cao, L. Dielectric Core–Shell Optical Antennas for Strong Solar Absorption Enhancement. *Nano Letters* **12,** 3674–3681 (2012).

77. Curto, A. G. *et al.* Multipolar radiation of quantum emitters with nanowire optical antennas. *Nature Communications* **4,** 1750 EP – (2013).

78. Ozel, T., Bourret, G. R., Schmucker, A. L., Brown, K. A. & Mirkin, C. A. Hybrid Semiconductor Core-Shell Nanowires with Tunable Plasmonic Nanoantennas. *Advanced Materials* **25,** 4515–4520 (2013).

79. Taminiau, T. H., Stefani, F. D. & van Hulst, N. F. Optical Nanorod Antennas Modeled as Cavities for Dipolar Emitters: Evolution of Sub- and Super-Radiant Modes. *Nano Letters* **11,** 1020–1024 (2011).

80. Kuznetsov, A. I., Miroshnichenko, A. E., Brongersma, M. L., Kivshar, Y. S. & Lukyanchuk, B. Optically resonant dielectric nanostructures. *Science* **354** (2016).

81. Barreda, A. I., Saiz, J. M., González, F., Moreno, F. & Albella, P. Recent advances in high refractive index dielectric nanoantennas: Basics and applications. *AIP Advances* **9,** 040701 (2019).

82. Albella, P., Alcaraz de la Osa, R., Moreno, F. & Maier, S. A. Electric and Magnetic Field Enhancement with Ultralow Heat Radiation Dielectric Nanoantennas: Considerations for Surface-Enhanced Spectroscopies. *ACS Photonics* **1,** 524–529 (2014).

83. Decker, M. & Staude, I. Resonant dielectric nanostructures: a low-loss platform for functional nanophotonics. *Journal of Optics* **18,** 103001 (2016).

84. Caldarola, M. *et al.* Non-plasmonic nanoantennas for surface enhanced spectroscopies with ultra-low heat conversion. *Nature Communications* **6,** 7915 EP – (2015).

85. Kivshar, Y. & Miroshnichenko, A. Meta-Optics with Mie Resonances. *Opt. Photon. News* **28,** 24–31 (2017).

86. Grzela, G. *et al.* Nanowire Antenna Absorption Probed with Time-Reversed Fourier Microscopy. *Nano Letters* **14,** 3227–3234 (2014).

87. Kuznetsov, A. I., Miroshnichenko, A. E., Fu Yuan Hsing Zhang, J. B. & Luk'yanchuk, B. Magnetic light. *Scientific Reports* **2,** 492 (2012).

88. Van de Groep, J. & Polman, A. Designing dielectric resonators on substrates: Combining magnetic and electric resonances. *Opt. Express* **21,** 26285–26302 (2013).

89. Van de Hulst, H. C. *Light Scattering by Small Particles* (Dover Publications, New York, 1981).

90. Bohren, C. & Huffman, D. R. *Absorption and Scattering of Light by Small Particles* (Wiley-VCH, 2004).

91. García-Etxarri, A. *et al.* Strong magnetic response of submicron Silicon particles in the infrared. *Opt. Express* **19,** 4815–4826 (2011).

92. Valuckas, V., Paniagua-Domínguez, R., Fu, Y. H., Luk'yanchuk, B. & Kuznetsov, A. I. Direct observation of resonance scattering patterns in single silicon nanoparticles. *Applied Physics Letters* **110,** 091108 (2017).

93. Evlyukhin, A. B. *et al.* Demonstration of Magnetic Dipole Resonances of Dielectric Nanospheres in the Visible Region. *Nano Letters* **12,** 3749–3755 (2012).

94. Cao, L., Fan, P., Barnard, E. S., Brown, A. M. & Brongersma, M. L. Tuning the Color of Silicon Nanostructures. *Nano Letters* **10,** 2649–2654 (2010).

95. Kapitanova, P. *et al.* Giant field enhancement in high-index dielectric subwavelength particles. *Scientific Reports* **7,** 731 (2017).

96. Van de Haar, M. A., van de Groep, J., Brenny, B. J. & Polman, A. Controlling magnetic and electric dipole modes in hollow silicon nanocylinders. *Opt. Express* **24,** 2047–2064 (2016).

97. Ee, H.-S., Kang, J.-H., Brongersma, M. L. & Seo, M.-K. Shape-Dependent Light Scattering Properties of Subwavelength Silicon Nanoblocks. *Nano Letters* **15,** 1759–1765 (2015).

98. Evlyukhin, A. B., Reinhardt, C. & Chichkov, B. N. Multipole light scattering by nonspherical nanoparticles in the discrete dipole approximation. *Phys. Rev. B* **84,** 235429 (2011).

99. Terekhov, P. D. *et al.* Multipolar response of nonspherical silicon nanoparticles in the visible and near-infrared spectral ranges. *Phys. Rev. B* **96,** 035443 (2017).

100. Yang, Y. *et al.* Nonlinear Fano-Resonant Dielectric Metasurfaces. *Nano Letters* **15,** 7388–7393 (2015).

101. Yang, Y. *et al.* Dielectric Meta-Reflectarray for Broadband Linear Polarization Conversion and Optical Vortex Generation. *Nano Letters* **14,** 1394–1399 (2014).

102. Moitra, P. *et al.* Large-Scale All-Dielectric Metamaterial Perfect Reflectors. *ACS Photonics* **2,** 692–698 (2015).

103. Paniagua-Domínguez, R. *et al.* Generalized Brewster effect in dielectric metasurfaces. *Nature Communications* **7,** 10362 (2016).

104. Person, S. *et al.* Demonstration of Zero Optical Backscattering from Single Nanoparticles. *Nano Letters* **13,** 1806–1809 (2013).

105. Staude, I. *et al.* Tailoring Directional Scattering through Magnetic and Electric Resonances in Subwavelength Silicon Nanodisks. *ACS Nano* **7,** 7824–7832 (2013).

106. Fu, Y. H., Kuznetsov, A. I., Miroshnichenko, A. E., Yu, Y. F. & Luk'yanchuk, B. Directional visible light scattering by silicon nanoparticles. *Nature Communications* **4,** 1527 (2013).

107. Cambiasso, J. *et al.* Bridging the Gap between Dielectric Nanophotonics and the Visible Regime with Effectively Lossless Gallium Phosphide Antennas. *Nano Letters* **17,** 1219–1225 (2017).

108. Terekhov, P. D. *et al.* Broadband forward scattering from dielectric cubic nanoantenna in lossless media. *Opt. Express* **27,** 10924–10935 (2019).

109. Wiecha, P. R. *et al.* Strongly Directional Scattering from Dielectric Nanowires. *ACS Photonics* **4,** 2036–2046 (2017).

110. Terekhov, P. D., Evlyukhin, A. B., Shalin, A. S. & Karabchevsky, A. Polarization-dependent asymmetric light scattering by silicon nanopyramids and their multipoles resonances. *Journal of Applied Physics* **125,** 173108 (2019).

111. Kobayashi, Y. & Kajikawa, K. Homogeneous dielectric cylinders invisible at optical frequency. *Applied Physics Express* **12,** 042001 (2019).

112. Shcherbakov, M. R. *et al.* Enhanced Third-Harmonic Generation in Silicon Nanoparticles Driven by Magnetic Response. *Nano Letters* **14,** 6488–6492 (2014).

113. Limonov, F. M., Rybin, V. M., Poddubny, N. A. & Kivshar, S. Y. Fano resonances in photonics. *Nature Photonics* **11,** 543–554 (2017).

114. Yan, J. *et al.* Directional Fano Resonance in a Silicon Nanosphere Dimer. *ACS Nano* **9,** 2968–2980 (2015).

115. Hopkins, B. *et al.* Interplay of Magnetic Responses in All-Dielectric Oligomers To Realize Magnetic Fano Resonances. *ACS Photonics* **2,** 724–729 (2015).

116. Yang, Z.-J. Fano Interference of Electromagnetic Modes in Subwavelength Dielectric Nanocrosses. *The Journal of Physical Chemistry C* **120,** 21843–21849 (2016).

117. Fan, P., Yu, Z., Fan, S. & Brongersma, M. L. Optical Fano resonance of an individual semiconductor nanostructure. *Nature Materials* **13,** 471 (2014).

118. Abujetas, D. R., Mandujano, M. A. G., Méndez, E. R. & Sánchez-Gil, J. A. High-Contrast Fano Resonances in Single Semiconductor Nanorods. *ACS Photonics* **4,** 1814–1821 (2017).

119. Royo, M., Bertoni, A. & Goldoni, G. Symmetries in the collective excitations of an electron gas in core-shell nanowires. *Phys. Rev. B* **89,** 155416 (2014).

120. Royo, M., Segarra, C., Bertoni, A., Goldoni, G. & Planelles, J. Aharonov-Bohm oscillations and electron gas transitions in hexagonal core-shell nanowires with an axial magnetic field. *Phys. Rev. B* **91,** 115440 (2015).

121. Sitek, A., Serra, L., Gudmundsson, V. & Manolescu, A. Electron localization and optical absorption of polygonal quantum rings. *Phys. Rev. B* **91,** 235429 (2015).

122. Sitek, A., Thorgilsson, G., Gudmundsson, V. & Manolescu, A. Multi-domain electromagnetic absorption of triangular quantum rings. *Nanotechnology* **27,** 225202 (2016).

123. Sitek, A., Torres, M. U. & Manolescu, A. Corner and side localization of electrons in irregular hexagonal semiconductor shells. *Nanotechnology* **30,** 454001 (2019).

124. Sitek, A., Thorgilsson, G., Gudmundsson, V. & Manolescu, A. Electronic states in core-shell quantum rings. *Proceedings of the 18th International Conference on Transparent Optical Networks (ICTON 2016)* (2016).

125. Funk, S. *et al.* High Mobility One- and Two-Dimensional Electron Systems in Nanowire-Based Quantum Heterostructures. *Nano Letters* **13,** 6189–6196 (2013).

126. Manolescu, A. *et al.* Conductance oscillations of core-shell nanowires in transversal magnetic fields. *Phys. Rev. B* **93,** 205445 (2016).

127. Sitek, A. *et al.* In-gap corner states in core-shell polygonal quantum rings. *Sci. Rep.* **7,** 40197 (2017).

128. *COMSOL Multiphysics® v. 5.4. www.comsol.com. COMSOL AB, Stockholm, Sweden.*

129. Daday, C., Manolescu, A., Marinescu, D. C. & Gudmundsson, V. Electronic charge and spin density distribution in a quantum ring with spin-orbit and Coulomb interactions. *Phys. Rev. B* **84,** 115311 (2011).

130. Groth, C. W., Wimmer, M., Akhmerov, A. R. & Waintal, X. Kwant: a software package for quantum transport. *New Journal of Physics* **16,** 063065 (2014).

131. Datta, S. *Electronic Transport in Mesoscopic Systems* (Cambridge University Press, 1997).

132. Fisher, D. S & Lee, P. A. Relation between conductivity and transmission matrix. *Phys. Rev. B* **23,** 6851 (1981).

133. Ferry, D. K. & Goodnick, S. M. *Transport in Nanostructures* (eds Ahmed, H., Pepper, M. & Broers, A.) (Cambridge University Press, Cambridge, 1997).

134. Doniach, S. & Sondheimer, E. H. *Green's Functions for Solid State Physicists* (Imperial College Press, London, 1998).

135. Timm, R. *et al.* Current-Voltage Characterization of Individual As-Grown Nanowires Using a Scanning Tunneling Microscope. *Nano Letters* **13,** 5182–5189 (2013).

136. Joyce, H. J., Boland, J. L., Davies, C. L., Baig, S. A. & Johnston, M. B. A review of the electrical properties of semiconductor nanowires: insights gained from terahertz conductivity spectroscopy. *Semiconductor Science and Technology* **31,** 103003 (2016).

137. Aspnes, D. E. & Studna, A. A. Dielectric functions and optical parameters of Si, Ge, GaP, GaAs, GaSb, InP, InAs, and InSb from 1.5 to 6.0 eV. *Phys. Rev. B* **27,** 985–1009 (1983).

138. Battiato, S *et al.* Polychromatic emission in a wide energy range from InP-InAs-InP multi-shell nanowires. *Nanotechnology* **30,** 194004 (2019).

139. Sonner, M. M. *et al.* Breakdown of Corner States and Carrier Localization by Monolayer Fluctuations in Radial Nanowire Quantum Wells. *Nano Letters* **19,** 3336–3343 (2019).

140. Ballester, A., Planelles, J. & Bertoni, A. Multi-particle states of semiconductor hexagonal rings: Artificial benzene. *Journal of Applied Physics* **112,** 104317 (2012).

141. Ameruddin, A. S. *et al.* InxGa1-xAs nanowires with uniform composition, pure wurtzite crystal phase and taper-free morphology. *Nanotechnology* **26,** 205604 (2015).

142. Urbaneja Torres, M. *et al.* Conductance features of core-shell nanowires determined by their internal geometry. *Phys. Rev. B* **98,** 085419 (2018).

143. Ferrari, G., Goldoni, G., Bertoni, A., Cuoghi, G. & Molinari, E. Magnetic States in Prismatic Core Multishell Nanowires. *Nano Letters* **9,** 1631–1635 (2009).

144. Ballester, A., Segarra, C., Bertoni, A. & Planelles, J. Suppression of the Aharonov-Bohm effect in hexagonal quantum rings. *EPL (Europhysics Letters)* **104,** 67004 (2013).

145. Tserkovnyak, Y. & Halperin, B. I. Magnetoconductance oscillations in quasiballistic multimode nanowires. *Phys. Rev. B* **74,** 245327 (2006).

146. Bellucci, S. & Onorato, P. Landau levels and edge states in a cylindrical two-dimensional electron gas: A semiclassical approach. *Phys. Rev. B* **82,** 205305 (2010).

147. Chang, C.-H. & Ortix, C. Ballistic anisotropic magnetoresistance in core–shell nanowires and rolled-up nanotubes. *Int. J. Mod. Phys. B* **31,** 1630016 (2017).

148. Manolescu, A. & Gerhardts, R. R. Coulomb effects on the quantum transport of a two-dimensional electron system in periodic electric and magnetic fields. *Phys. Rev. B* **56,** 9707–9718 (1997).

149. Sitek, A. *et al.* Excitons in Core–Shell Nanowires with Polygonal Cross Sections. *Nano Letters* **18,** 2581–2589 (2018).

150. Sitek, A., Urbaneja Torres, M., Torfason, K., Gudmundsson, V. & Manolescu, A. Controlled Coulomb effects in core-shell quantum rings. *Proceedings of the 19th International Conference on Transparent Optical Networks (ICTON 2017)* (2017).

151. Torres, M. U., Sitek, A. & Manolescu, A. *Transverse polarization light scattering in tubular semiconductor nanowires* in *2019 20th International Conference on Transparent Optical Networks (ICTON)* (2019), 1–4.

152. Torres, M. U., Sitek, A. & Manolescu, A. Anisotropic light scattering by prismatic semiconductor nanowires. *Opt. Express* **27,** 25502–25514 (2019).

153. Terekhov, P. D. *et al. Proc. SPIE* **10528** (2018).

Appendix A

Appendix

A.1 Matrix elements of the Exchange interaction term

$$\langle a_1 k_1 s_1 | \Sigma_F | a_2 k_2 s_2 \rangle = -\sum_k \sum_{a'_1, a'_2} \sum_{s'_1, s'_2} F(a'_1, a'_2, k) X(a'_1, a'_2, a_1, a_2, |k - k_1|) \delta\sigma_{s_1}\sigma_{s'_1}\delta\sigma_{s_2}\sigma_{s'_2}$$

where

$$F(a'_1, a'_2, k) = \frac{\Delta k}{2\pi} \sum_{m,s} \psi^*{}_{mks}(a'_1)\psi_{mks}(a'_2)\mathcal{F}\left(\frac{E_{mks} - \mu}{k_B T}\right)$$

and

$$X(a'_1, a'_2, a_1, a_2, |k - k_1|) = 2u_c \sum_{q_1, q_2} \psi_{a'_1}(q_1)\psi^*_{a_1}(q_1)\psi_{a'_2}(q_2)\psi^*_{a_2}(q_2) K_0\left(|(k - k_1)(\boldsymbol{r_{q_1}} - \boldsymbol{r_{q_2}})|\right)$$

with $u_c = e^2/(4\pi\epsilon_0\chi)$ and K_0 is the modified Bessel function of the second kind.

A.2 Matrix elements of the tilted perturbation

$$\langle m | V_{ext} | m' \rangle = V_x \langle m | x | m' \rangle + V_y \langle m | y | m' \rangle + V_z \langle m | z | m' \rangle$$

$$\langle m | x | m' \rangle = \sum_{ans} \sum_{a'n's'} \psi_m(ans)\psi^*{}_{m'}(a'n's')\delta_{ss'}\delta_{nn'} \sum_q \psi^*_a(q)\psi'_a(q)x_q$$

$$\langle m | y | m' \rangle = \sum_{ans} \sum_{a'n's'} \psi_m(ans)\psi^*{}_{m'}(a'n's')\delta_{ss'}\delta_{nn'} \sum_q \psi^*_a(q)\psi'_a(q)y_q$$

$$\langle m | z | m' \rangle = \sum_{ans} \sum_{a'n's'} \psi_m(ans)\psi^*{}_{m'}(a'n's')\delta_{ss'}\delta_{aa'} \sum_{qq'} \psi^*_a(q)\psi'_a(q') \langle n | z | n' \rangle$$

A.3 Current density distribution and its time-derivative over a complete period

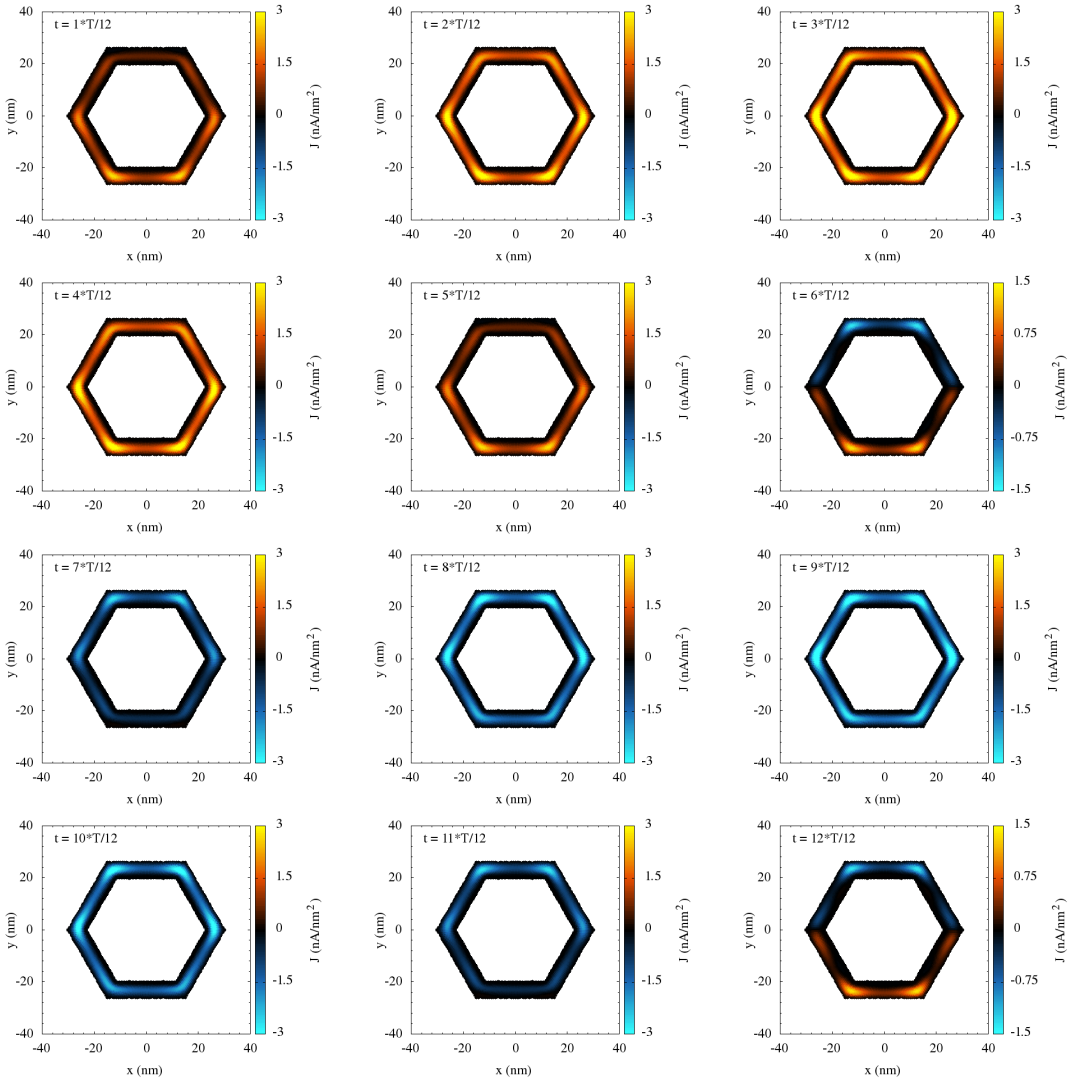

Figure A.1: Current density distribution over a complete period when a magnetic field of $B = 1$ T is applied perpendicular to one of the edges of the nanowire. The carrier concentrarion is $n = 1 \cdot 10^{-5}$ nm^{-3}.

A.4 Time-derivative of the current density over a complete period

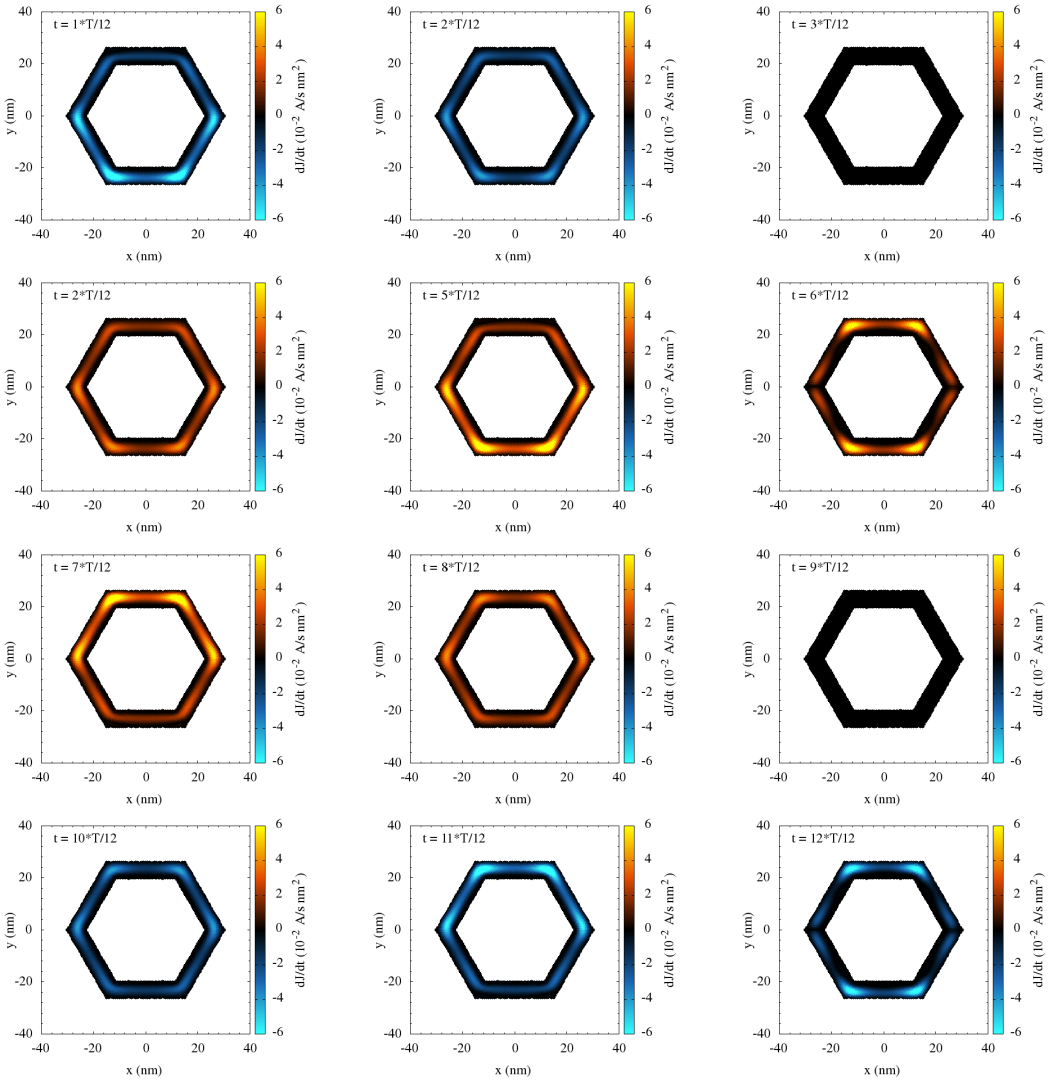

Figure A.2: Time-derivative of the current density distribution over a complete period when a magnetic field of $B = 1$ T is applied perpendicular to one of the edges of the nanowire. The carrier concentrarion is $n = 1 \cdot 10^{-5}$ nm^{-3}.